Analysis and simulation of forming process of 2D and 3D-tubular biaxial braided composite reinforcements

Jinlei Li

Année 2023 N° d'ordre : (attribué par le SCD)

UNIVERSITÉ DE HAUTE-ALSACE
UNIVERSITÉ DE STRASBOURG

THESE

Pour l'obtention du grade de

DOCTEUR DE L'UNIVERSITÉ DE HAUTE-ALSACE

ECOLE DOCTORALE : Mathématiques, Sciences de l'Information et de l'Ingénieur (ED 269)

Discipline : Mécanique

Présentée et soutenue publiquement

par

Jinlei LI

Le 08 Novembre 2023

Analysis and simulation of forming process of 2D and 3D-tubular biaxial braided composite reinforcements

---

Sous la direction des Prof. Peng WANG, Prof. Nahiène HAMILA et Prof. Gildas L'HOSTIS

Jury :	Prof. Sylvain DRAPIER	Mines de Saint-Etienne	(Rapporteur)
	Prof. Olivier POLIT	Université Paris Nanterre	(Rapporteur)
	Prof. Anita CATAPANO	Bordeaux INP	(Examinateur)
	Prof. Christophe BINETRUY	Ecole Centrale de Nantes	(Examinateur)
	Prof. Peng WANG	Université de Haute Alsace	(Directeur de thèse)
	Prof. Nahiène HAMILA	ENI Brest	(co-Directeur de thèse)
	Prof. Gildas L'HOSTIS	Université de Haute Alsace	(co-Directeur de thèse)
	Dr. Eduardo Guzman-Maldonado	Innovamics	(invité)

ACKNOWLEDGEMENTS

Time passes so fast, with the completion of the dissertation, three years of my doctoral career is coming to an end unconsciously. Looking back on the life of doctoral studies, thanks to all the people who have helped me!

I would first like to express my sincere appreciation to my three supervisors: Prof. Peng WANG, Prof. Nahiène Hamila and Prof. Gildas L'Hostis. They gave me the opportunity to do research in France and helped me to broaden my professional knowledge and life experience. They have provided patient guidance and supervision throughout my PhD research and encouraged me to try out new ideas. Their energy, vision, sincerity and motivation have inspired me deeply. Many thanks for their care in my life and help in the scientific research.

I am also very grateful to my cooperator Dr. Eduardo Guzman-Maldonado for the theoretical and technical supports in the simulation analysis, which helped me to quickly understand the theory and apply it to my PhD project.

I am especially grateful to all the staff at the LPMT lab for providing me with experimental and technical help. Thanks to my colleagues and friends: Sascha Krugl, Julie WALTHER, Mahmoud HUSSEIN, Théo PERRIN, Benoit SCHRAB, Abdul Rahmann ASAAD, Yu WANG, Jingshu LU for discussion and knowledge-sharing during my time in research. I would like also thanks to Dr. Shenglei XIAO and Dr. Hao SHEN for their encouragement, advice and help.

I wish to acknowledge the China Scholarship Council (CSC) for the financial support of my doctoral research.

At last, I would like to express my deepest gratitude to my family members for their unconditional support and encouragement during my doctoral studies. I would like to thank my boyfriend for his constant companionship, care and help.

ABSTRACT

The mechanical properties and deformation behavior of textile reinforcements are crucial for the manufacture of composite parts with complex shapes. The quality of reinforcements determines the mechanical properties and load-bearing capacity of the composite parts. This thesis will focus on two-dimensional flat braids and three-dimensional tubular braids to explore the mechanical properties of braided reinforcements from both experimental and simulation aspects. Firstly, based on the bias-extension test, the in-plane shear mechanical model of flat fabric was established by a kinematic method. On this basis, the mechanical properties of tubular fabric were investigated. Uniaxial tensile tests were conducted on the tubular fabric to obtain the shear response. Meanwhile, a theoretical model for characterizing the shear behavior of tubular fabrics was developed and validated based on the experimental results. In addition, considering that the fabric was greatly affected by temperature during the forming process, the thermomechanical behavior of tubular braids was investigated. The effects of different temperatures and tensile speeds on the load-bearing capacity and shear properties of fabrics were discussed. To improve manufacturing efficiency and avoid “trial and error”, a non-orthogonal hyperelastic constitutive model for simulating the forming process of braided reinforcements was improved. The model considered the tensile and shear deformation modes of the braided fabrics during the forming process and used invariants to describe the corresponding strain energy. The relation between the tensile load and the second Piola-Kirchhoff stress tensor was also established to identify the material parameters. The simulation results of the bias-extension test and hemispherical stamping test of the braided fabrics were compared with experimental results to verify the correctness of the hyperelastic model. Finally, based on the tensile test of the tubular braided fabrics, the hyperelastic model was used to investigate the forming of the tubular fabrics. The results show that the theoretical model proposed in the experimental part of this thesis and the improved non-orthogonal hyperelastic constitutive model in the simulation part can effectively characterize the mechanical behavior of the braided fabrics.

Résumé

Les propriétés mécaniques et la déformabilité des renforts textiles sont essentielles pour la fabrication de pièces composites de formes complexes. La qualité des renforts détermine les propriétés mécaniques et la capacité de charge des pièces composites. Cette thèse se concentrera sur les tresses plates bidimensionnelles et les tresses tubulaires tridimensionnelles pour explorer les propriétés mécaniques des renforts tressés sous des aspects expérimentaux et de simulation. Tout d'abord, sur la base du Bias-extension test, le modèle mécanique de cisaillement dans le plan de la tresse plate a été établi par une méthode cinématique. Sur cette base, les propriétés mécaniques de la tresse tubulaire ont été étudiées. Des essais de traction uniaxiale ont été réalisés sur pour obtenir la réponse au cisaillement. En même temps, un modèle théorique caractérisant le comportement de cisaillement des tresses tubulaires a été développé et validé sur la base des résultats expérimentaux. De plus, compte tenu de l'impact important de la température sur le renfort co-mélé thermoplastique lors du thermoformage, le comportement thermomécanique des tresses tubulaires a été étudié. Les effets de différentes températures et vitesses de traction sur la capacité de charge et les propriétés de cisaillement des renforts textiles ont été discutés. Pour améliorer l'efficacité de la fabrication et éviter les essais coûteux, un modèle constitutif hyperélastique non orthogonal pour simuler le procédé de mise en forme des renforts tressés a été amélioré. Le modèle prenait en compte les modes de déformation en traction et en cisaillement des tresses lors de la mise en forme et utilisait des invariants pour décrire l'énergie de déformation correspondante. La relation entre la charge de traction et le tenseur des contraintes de Piola-Kirchhoff de second ordre a été également établie pour identifier les paramètres du matériau. Les résultats de simulation du Bias-extention test et du test d'emboutissage hémisphérique des tresses ont été comparés aux résultats expérimentaux pour vérifier le modèle numérique dévelopé. Enfin, sur la base de l'essai de traction des tresses tubulaires, le modèle hyperélastique a été utilisé pour étudier le préformage des tresses tubulaires. Les résultats montrent que le modèle théorique proposé dans la partie expérimentale de cette thèse et le modèle constitutif hyperélastique non orthogonal amélioré dans la partie de simulation peuvent caractériser efficacement le comportement mécanique des tresses biaxiales avec des structures 2D et 3D-tubulaire.

CONTENTS

LIST OF FIGURES

Chapter I

Chapter II

Chapter III

Chapter IV

Appendix A

LIST OF TABLES

Chapter II

Chapter III

Chapter IV

GENERAL INTRODUCTION

Résumé en français

Les composites textiles, en tant que matériaux avancés, ont été largement utilisés dans divers domaines. Leur application permet de réduire le poids des pièces composites de forme complexe. Par rapport aux matériaux métalliques traditionnels, les composites textiles ont une résistance et une rigidité similaires, mais leur poids est considérablement réduit, ce qui est important pour la réduction de la consommation d'énergie et de la pollution de l'environnement. La fabrication de pièces composites nécessite une phase de mise en forme du renfort dans la géométrie souhaitée, ce que l'on appelle le procédé du préformage. Au cours de ce procédé, la déformation du textile est complexe et les facteurs affectant la déformation sont nombreux, ce qui peut facilement entraîner divers défauts de mise en forme, tels que le plissement, les boucles et le glissement. Étant donné que ces défauts de mise en forme ne peuvent pas être éliminés et qu'ils sont conservés dans les phases de préformage ultérieurs, ils finissent par affecter la forme et les performances des structures composites finales. Cette situation est très défavorable au traitement et à la fabrication des pièces composites, et il est nécessaire d'éliminer des défauts à la source et d'améliorer la qualité du préformage.

Afin d'améliorer la qualité du formage des pièces composites, le procédé de préformage des renforts textiles est devenu le cœur de la recherche. Les propriétés mécaniques et le comportement à la déformation des renforts textiles sont cruciaux pour la fabrication de pièces composites de forme complexe, et leur qualité de préformage influence fortement les propriétés mécaniques et la capacité de charge des pièces. Les renforts textiles sont généralement préparés par deux procédés textiles : le tissage et le tressage. Les renforts tissés à une seule couche sont formés par l'entrecroisement de deux ensembles de fils orthogonaux. Les fils longitudinaux sont les fils de chaîne et les fils transversaux sont les fils de trame. Lorsque la préforme tissée à une seule couche ne peut répondre aux exigences d'épaisseur du matériau composite, la préforme tissée à plusieurs couches peut être empilée et reliée par des fils dans le sens de l'épaisseur

pour obtenir une préforme tridimensionnelle. Bien que les matériaux composites préparés par les préformes tridimensionnelles présentent une résistance élevée au cisaillement entre les couches, ce qui résout efficacement le problème de la fissuration par délamination des composites stratifiés, les préformes bidimensionnelles et tridimensionnelles ne peuvent pas répondre aux exigences d'épaisseur du matériau composite. Enfin les préformes tissées bidimensionnelles et tridimensionnelles ont un champ de mise en forme par l'angle de tissage qui est fixe et égal à 90°. La recherche a révélé que le processus de tressage, un autre procédé textile couramment utilisé, permet de préparer des renforts tressés qui peuvent compenser les défauts des renforts tissés. Les préformes tressées présentent une plus grande variabilité structurelle et davantage de motifs de tressage, ce qui permet de les concevoir en fonction de différentes conditions d'application, élargissant ainsi le champ d'application des composites textiles. En raison de la structure symétrique des préformes tissées, la loi de comportement est facile à caractériser et à prévoir et elle a l'objet de nombreux travaux. Ceci n'est pas le cas pour les préformes tissées, car son comportement mécanique pendant le préformage n'a pas été aujourd'hui entièrement caractérisé. L'objet de ce travail porte sur l'étude et l'analyse des propriétés mécaniques pertinentes des préformes tressées, lors de leur mise en forme par préformage.

Le chapitre I présente d'abord une revue de la littérature sur les textiles composites, résumant les types de préformes textiles, le procédé du préformage et les défauts existants. Afin de minimiser les défauts, ce chapitre étudie les essais pertinents pour caractériser les propriétés mécaniques des préformes en fonction de leurs modes de déformation pendant le préformage, y compris les propriétés de traction, de cisaillement dans le plan et de flexion. Sur la base des recherches expérimentales, les propriétés mécaniques des préformes peuvent être obtenues et utilisées pour simuler le procédé de mise en forme du renfort textile afin d'éviter les "erreurs de mesures expérimentales". C'est pourquoi différentes méthodes de simulation sont ensuite exposées, principalement à l'échelle macroscopique, mésoscopique et microscopique.

Parallèlement, les modèles discrets, semi-discrets et continus sont également résumés pour le problème des grandes déformations des tissus. On montre ainsi que les différentes méthodes de simulation ont leurs propres avantages et inconvénients et doivent être choisies raisonnablement en fonction des problèmes pratiques.

Le chapitre II présent principalement des recherches sur les tresses plates bidimensionnelles et les tresses tubulaires tridimensionnelles, et explore les propriétés mécaniques des renforts tressés à partir de l'expérience. Les propriétés mécaniques des préformes tressées bidimensionnelles ont été déterminées par des essais « Bias extension tests ». Une approche cinématique est utilisée pour établir un modèle mécanique de cisaillement dans le plan pour les tresses afin de décrire leur comportement en cisaillement. Les propriétés mécaniques des tresses tubulaires sont ensuite étudiées. Des essais de traction uni axiale sont effectués pour obtenir leur réponse au cisaillement. Il a été constaté que ces tresses subissent un cisaillement inhomogène en surface extérieure du tube, une combinaison de cisaillement en surface et d'extension du fil, et enfin une extension pure du fil sous une charge de traction. En outre, un modèle analytique permettant de caractériser le comportement en cisaillement des tresses tubulaires est établi et vérifié par rapport aux résultats expérimentaux. De plus, étant donné l'influence significative de la température sur le renfort pendant le thermoformage, le comportement thermomécanique de tresses tubulaires est également étudié. Les effets de températures et vitesses de traction sur les propriétés de cisaillement sont discutés.

Pour améliorer l'efficacité et réduire les coûts de fabrication, le chapitre III développe un modèle constitutif hyperélastique non orthogonal pour simuler le préformage des renforts tressés. Le modèle prend en compte les modes de déformation en traction et en cisaillement des tresses pendant leur mise en forme et utilise les invariants de la transformation géométrique pour décrire l'énergie de déformation correspondante. La relation entre la charge de traction et le second tenseur des contraintes de Piola-Kirchhoff est également établie pour identifier les paramètres du matériau. Les résultats

de simulation des essais de « Bias-extension test » et d'emboutissage hémisphérique ont été comparés aux résultats expérimentaux pour valider le modèle développé.

Enfin, le chapitre IV se concentre sur l'étude de la simulation de la mise en forme de tresses tubulaires par le modèle hyperélastique développé dans chapitre III. En tirant parti du comportement de contraction radiale des tresses tubulaires sous tension, le tresse est étiré et conformé sur des moules de différentes formes pour obtenir la forme souhaitée. L'effet des différentes formes de section transversale sur les propriétés de cisaillement des tissus est analysé. Les résultats indiquent que le modèle analytique du renfort tressé proposé dans la partie expérimentale et le modèle constitutif hyperélastique non orthogonal dans la partie simulation peuvent caractériser efficacement le comportement mécanique du renfort tressé, ce qui pose une base théorique pour la mise en forme rapide de préformes tressées multicouches dans les procédés ultérieurs.

Problems statement

Textile composites, as an advanced material, have been widely used in various fields. Its application provides the possibility of reducing the weight of composite parts with complex shapes. Compared with traditional metal materials, textile composites have similar strength and stiffness, but their weight is greatly reduced, which is significant for reducing energy consumption and environmental pollution. The manufacture of composite parts requires preforming the reinforcement into the desired shape, which is known as the preforming process. During this process, the deformation of the fabric is more complex and there are more factors affecting the deformation, which can easily lead to a variety of forming defects, such as wrinkling, buckling and slippage. Considering that these forming defects cannot be eliminated and are retained in subsequent forming processes, they ultimately affect the shape and performance of the composite components. This is very unfavorable to the processing and manufacturing of composite parts, and it is necessary to eliminate the forming defects at the source and improve the forming quality.

To improve the forming quality of composite parts, the preforming process of textile reinforcement has become the focus of research. The mechanical properties and deformation behavior of textile reinforcements are crucial to the manufacture of composite parts with complex shapes, and their preforming quality determines the mechanical properties and load-bearing capacity of the parts. Textile reinforcements are usually prepared by two textile processes: weaving and braiding. The single-layer woven preforms are formed by interweaving two sets of orthogonal yarns. The longitudinal yarns are called warp yarns, and the transverse yarns are called weft yarns. When the single-layer woven preform cannot meet the thickness requirements of the composite material, the multi-layer woven preform can be stacked together and connected with yarn along the thickness direction to obtain a three-dimensional preform.

Although composite materials prepared by the three-dimensional preforms have high interlayer shear resistance, which effectively solves the problem of delamination

cracking of the laminated composites. However, the two-dimensional and three-dimensional woven preforms limit their application range because the weaving angle is fixed at 90°. The research has found that braiding process, as another commonly used textile process, can prepare braided preforms that can compensate for the shortcomings of woven preforms. Braided preforms have greater structural variability and more braiding patterns, allowing for design based on different application conditions, thus further expanding the application range of textile composites. At the same time, due to the symmetrical structure of woven preforms, the deformation law is easy to characterize and predict. So, it has been widely studied. Compared with the woven preform, the deformation behavior characteristics of braided preform during the preforming process have not been fully characterized. This thesis will analyze and study the relevant properties of braided preforms.

Thesis outline

Chapter I first provides a literature review on textile composites, summarizing the types of textile preforms, preforming process and existing forming defects. In order to minimize defects, this chapter investigates the relevant tests for characterizing the mechanical properties of preforms according to their deformation modes during the forming process, including tensile, in-plane shear and bending properties. Based on experimental researches, the material properties of the preforms can be obtained and used to simulate the fabric forming process to avoid “trial and error”. Therefore, different simulation methods are proposed, mainly including macroscopic, mesoscopic and microscopic scales. Meanwhile, discrete, semi-discrete and continuous methods are also summarized for the large deformation problem of fabrics. Different simulation methods have their own advantages and disadvantages, and should be chosen reasonably according to practical problems.

Chapter II mainly takes two-dimensional flat braids and three-dimensional tubular braids as the research objects, and explores the mechanical properties of braided fabrics from the experiment. The mechanical properties of the two-dimensional braided

preforms were determined by bias-extension tests. A kinematic approach is used to establish an in-plane shear mechanical model for braided fabric to describe their shear behavior. Based on this, the mechanical properties of tubular braids are explored. The uniaxial tensile tests are conducted on tubular fabrics to obtain their shear response. It's found that such fabrics undergo non-homogenous in-plane shearing, a combination of in-plane shearing and yarn extension, and finally pure yarn extension under tensile loading. Additionally, a theoretical model for characterizing the shear behavior of tubular fabrics are established and verified according to the experimental phenomena. Furthermore, considering the significant influence of temperature on fabric during the forming process, the thermomechanical behavior of tubular braided fabric is also studied. The effects of different temperatures and tensile speeds on the load-bearing capacity and shear properties of the tubular fabric are discussed.

To improve manufacturing efficiency and reduce manufacturing costs, Chapter III improves a non-orthogonal hyperelastic constitutive model for simulating the forming process of braided reinforcements. The model considers the tensile and shear deformation modes of the braided fabrics during the forming process and uses invariants to describe the corresponding strain energy. The relation between the tensile load and the second Piola-Kirchhoff stress tensor is also established to identify the material parameters. The simulation results of the bias-extension test and hemispherical stamping test of the braided fabrics were compared with experimental results to verify the correctness of the hyperelastic model.

Finally, based on the tensile tests of tubular fabrics, Chapter IV focuses on the forming of tubular braids based on the improved hyperelastic model. By taking advantage of the radial contraction behavior of tubular fabrics under tension, the fabric is stretched and conformed on the molds of different shapes to achieve the desired shape. The effect of different cross-sectional shapes on the shear properties of fabrics is analyzed. The results indicate that the theoretical model of the braided fabric proposed in the experimental part and the improved non-orthogonal hyperelastic constitutive

model in the simulation part can effectively characterize the mechanical behavior of the braided fabric, which lays a theoretical foundation for the rapid forming of multi-layer braided preforms in subsequent processes.

I. State of the art

Résumé en français

Ces dernières années, sous la demande de l'industrie de la fabrication haut de gamme, les matériaux composites aux formes complexes sont devenus progressivement un sujet de recherche phare dans le domaine des composites, comme le montre la Fig. 1.1 Aujourd'hui, l'application des matériaux composites dans les composants structuraux porteurs de grandes surfaces est relativement mature. Avec les exigences croissantes en matière de matériaux légers dans les industries aérospatiale et automobile, la demande de composites aux formes complexes augmente également progressivement. En effet, les composites aux formes complexes présentent non seulement les mêmes propriétés mécaniques que les composants métalliques, mais ils permettent également de réduire d'avantage le poids des pièces et de réaliser des économies d'énergie. En raison de l'anisotropie des matériaux composites, la maîtrise est difficile dans le processus de fabrication de pièces composites aux formes complexes. Actuellement, la production de composants en matériaux composites de haute qualité et efficace est devenue un point difficile et un défi dans le domaine des matériaux composites.

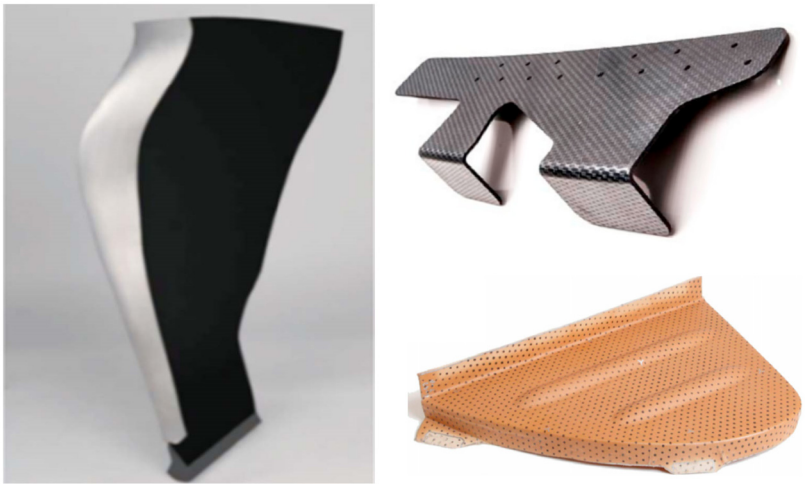

Fig. 1.1 Pièces composites aux formes complexes [1,2].

Les pièces composites aux formes complexes peuvent être réalisées grâce à la technologie textile, ce qui favorise le développement des composites textiles. Les composites textiles sont des matériaux haute performance composés de préformes de fibres et de la polymérisation de la matrice. Lors de la préparation de pièces composites textiles aux formes complexes, il est généralement nécessaire de préparer le textile en préformes, c'est-à-dire un processus de préformage. L'orientation des fibres et la forme

de préformage à cette étape ont un impact significatif sur l'injection de résine ultérieure et la capacité de charge des pièces composites. Par conséquent, la structure et les propriétés mécaniques des préformes de fibres déterminent les propriétés mécaniques des pièces composites structurales.

Actuellement, il existe de nombreuses structures différentes de préformes, notamment le tissage, le tressage, le tricotage et le surpiquage, réalisées selon différents processus de formation textile. En même temps, selon la pénétration des fils dans la direction de l'épaisseur de la préforme, celle-ci peut être divisée en une structure bidimensionnelle plane et une structure tridimensionnelle. Dans la structure tridimensionnelle, on trouve à la fois des tissus tubulaires avec une bonne intégrité et des tissus planaires multicouches reliés par des fils de liage. Étant donné que les différentes structures des préformes textiles présentent différentes propriétés mécaniques, il est nécessaire de les classer. Des études ont montré que les propriétés mécaniques des textiles sont principalement déterminées par la structure des fibres. Cela s'explique par le fait que les textiles sont composés de nombreux fils discrets, et chaque fil est composé de centaines de fibres. Pour les textiles secs, l'absence de cohésion interne entre les fibres en raison de l'absence de remplissage de la matrice les rend susceptibles de glisser, ce qui affecte la qualité du préformage des textiles. De plus, l'anisotropie du textile entraîne également une hétérogénéité de la résistance et de la rigidité des tissus, qui est étroitement liée à l'orientation des fibres. Tous ces facteurs provoquent différents types de défauts de formage dans les préformes lors du processus de formage.

En mettant l'accent sur les préformes textiles, ce chapitre présente d'abord les applications des composites textiles, puis fournit un résumé détaillé de la classification des préformes textiles. Étant donné que les préformes avec différentes structures ont des propriétés mécaniques différentes, le processus de préformage est très important et le tissu est accompagné de défauts pendant le processus de préformage. Afin de minimiser les défauts, des tests mécaniques sur les préformes sont également étudiés, comprenant principalement la tension, le cisaillement plan et la flexion. Sur la base des tests mécaniques, les propriétés de la préforme peuvent être caractérisées et utilisées comme paramètres de simulation importants pour simuler la mise en forme du tissu. Différentes méthodes de simulation ont été proposées pour différentes échelles de recherche, comprenant principalement le niveau microscopique, mésoscopique et macroscopique. En même temps, selon l'objet de recherche, cela peut être divisé en

modèles discrets, semi-discrets et continus. Ce chapitre fournit un résumé systématique de la caractérisation expérimentale et de la modélisation mécanique des propriétés mécaniques des préformes, ce qui constitue la base des chapitres suivants.

Mots-clés : Composites textiles ; Préformage ; Défauts ; Propriétés mécaniques ; Simulation.

1.1 Introduction to the textile composites

1.1.1 Textile composites and their applications

Composite materials are composed of two or more materials with different properties through physical or chemical methods. It is a material with new properties that can bring into play the advantages of various materials, overcome the shortcomings of a single material, expand the scope of material applications and better meet various performance requirements. Composites consist of two main components: matrix and reinforcement. The reinforcement provides strength and stiffness support for the material and controls the mechanical properties of the entire structure. The matrix holds and protects the reinforcement, transmits loads, and provides cohesion. The combination of matrix and reinforcement combines the properties of different materials, showing the characteristics of lightweight, high strength, convenient processing and molding, excellent elasticity, and chemical corrosion resistance. It has gradually replaced wood and metal alloys and is widely used in aviation and automobiles, medical, construction, sports, energy and military manufacturing, and other manufacturing fields.

Composites were first used to manufacture laminates and are widely used due to their high stiffness and strength. In the process of application, the out-of-plane properties are weak and the fabric lay-up process takes a lot of time [3]. Therefore, over the past few decades, textile composites have been developed to compensate for the disadvantages of laminates. Textile composites refer to the materials that use textile technology to prepare various fiber-reinforced materials into textile preforms, and then mix the matrix with the preforms. Compared with conventional laminated composites, the preparation of textile composites has a higher production efficiency, and the structural stability of the material is improved due to the interlacing of yarns [4]. The problem of delamination in the thickness direction of the laminate is also solved by adding a binder yarn [5] that runs through each layer of fabric along the thickness direction of the textile fabric, avoiding defects such as interlayer cracking and delamination damage of composite components. At the same time, textile technology can manufacture various complex shapes more flexibly and play an irreplaceable role in weight reduction for large and complex components. Therefore, it is widely used in various fields, as shown in Fig. 1.2.

In aviation, high strength, high rigidity, and lightweight are the basic requirements for structural materials in the aerospace field. The development of textile technology

has further expanded the scope of the application of composite materials in aviation, from non-load-bearing components such as spoilers and fairings to secondary load-bearing components such as aircraft tails to large-scale main load-bearing components such as cabins and wings. Composites have gradually replaced traditional metals such as steel, aluminum and titanium to become the fourth largest aerospace structural materials. At present, in the field of civil airliners, the amount of composite materials used in Boeing 777 has reached 9.9t, accounting for 25% of the total weight of the structure; Boeing 787 took the lead in applying composite materials to the main bearing structure, and the amount of composite materials used exceeds 50% of the total weight of the entire structure [6]. The Airbus A350-XWB has further increased the amount of advanced composite materials, reaching 52% of the total weight of the structure.

In the automotive field: The high strength and high modulus of composite materials are widely used in the automotive field, which greatly reduces the overall weight and fuel consumption of the body. Textile composites are used instead of metal in the body, interior, bumpers, wheels and other parts of the car to achieve a better weight reduction effect. For example, the BMW i8 uses composite materials for its body, reducing its mass by 39%. At the same time, the higher cushioning capacity and energy absorption rate of the composite material also improves the crash safety of the car.

Other fields: Textile composites are also widely used in various fields such as sports, medicine and military. Sports helmets, skis, medical prostheses, medical braces, tank armor and bulletproof vests all meet their respective performance requirements by using textile composite materials.

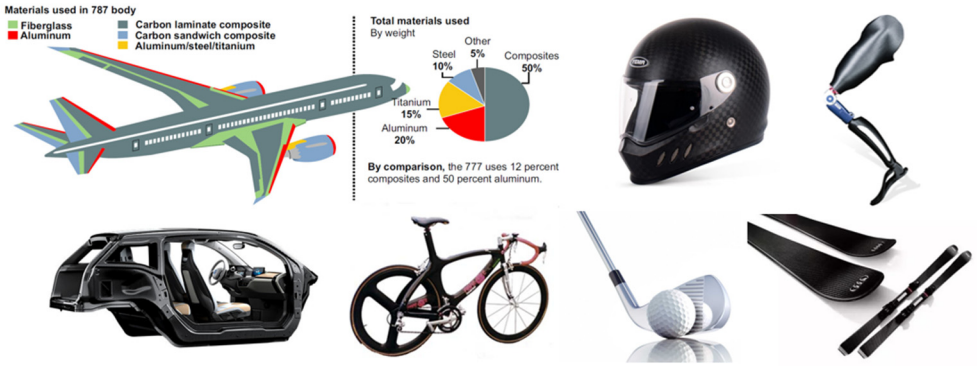

Fig. 1.2 Applications of textile composites.

1.1.2 Textile reinforcement

According to the definition of composite materials, the composition of textile

composites also includes matrix and reinforcement. The matrix consists mainly of polymer, metal and ceramic, while the reinforcement includes natural and artificial fibers, etc. The manufacture of textile composite components first requires the reinforcement fibers to be made into textile preforms. Depending on the textile process, the textile preforms can be classified as woven, knitted, braided and nonwoven fabrics [7], as shown in Fig. 1.3. Based on the dimensionality of the fabric, the preforms are further divided into two-dimensional (2D) fabrics and three-dimensional (3D) fabrics. Two-dimensional fabrics, also known as flat fabrics, are manufactured from two sets of yarns with different orientations by textile technology. Among them, two-dimensional woven fabrics are composed of two sets of orthogonal yarns, the longitudinal yarns are called the warp and the lateral yarns are weft. Due to their good in-plane properties and drapability, two-dimensional woven fabrics can be formed integrally and have become one of the most widely studied types of fabrics. With the expansion of fabric applications, single-layer fabrics cannot meet the thickness requirements of composite materials, and it's necessary to stack multi-layer fabrics and increase yarns in the thickness direction for effective connection, thereby obtaining three-dimensional woven fabrics. Whether it is a two-dimensional woven fabric or a three-dimensional woven fabric, the interlacing angle between yarns is fixed at 90° and cannot be changed, which leads to a relatively single variety and pattern of fabrics, and the angle of yarns cannot be modified when forming complex shapes, thus limiting the further use of woven preforms. Therefore, braiding technology has gradually developed and been applied to the preparation process of textile preforms [8,9]. Unlike woven fabrics, the angle between the two sets of yarns in braided fabrics can be specified as arbitrary angles, and the drapability is further improved, making them more suitable for manufacturing complex curved shapes. This shows that braided fabrics have broad development prospects. Considering that the research on braided fabrics is still incomplete, the mechanical properties of braided fabrics have not been fully characterized. Therefore, this thesis mainly focuses on the preforming process of braided fabrics as the research object.

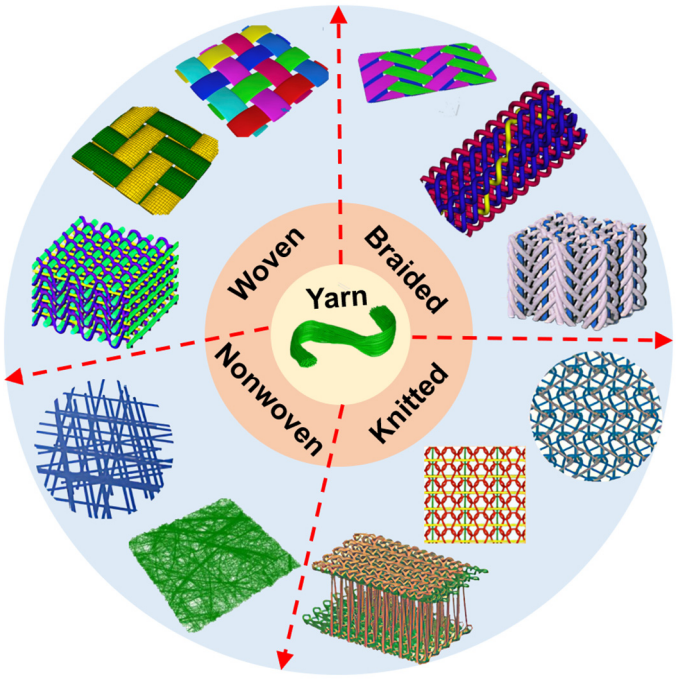

Fig. 1.3 Types of textile fabric reinforcement.

1.2 Introduction of braided fabric reinforcement

1.2.1 Braiding technique

Among various textile composites, artificial fibers (carbon fiber and glass fiber) have been widely used in textile preforms due to their excellent properties such as high strength, high stiffness, and corrosion resistance [10–13]. However, artificial fibers have poor biodegradability and cannot be recycled. In contrast, natural fibers (flax and cotton) mainly come from plants and are easier to obtain with low cost and easy recycling and biodegradability while meeting certain mechanical properties. Therefore, they have gradually attracted attention from manufacturing industries such as aviation and automotive. To further utilize the advantages of natural fiber-reinforced composites, people have integrated ancient braiding technology with modern composite molding technology in recent decades, forming unique braided structure composites. Braided structure composites are the product that combines modern textile industry technology with advanced composite material technology, displaying unique advantages in the field of modern engineering technology.

The development of braiding technology is shown in Fig. 1.4. It's a kind of biased interlacing technique for creating rope-like structures which can be traced back to the early European pentacle dance [14]. In a traditional braiding machine, the yarn carriers

are centered on a bobbin and rotated along a disc track. In this case, the yarn carriers are divided into two groups, one group of yarns rotates in a clockwise direction and the other group rotates in a counterclockwise direction. In this case, multi-strand yarns are interwoven at a certain angle to manufacture flat or tubular fabrics. The development and application of braiding machines can precisely position and control the yarn, which greatly improves the preparation speed of braided fabrics and has broad application prospects [15,16].

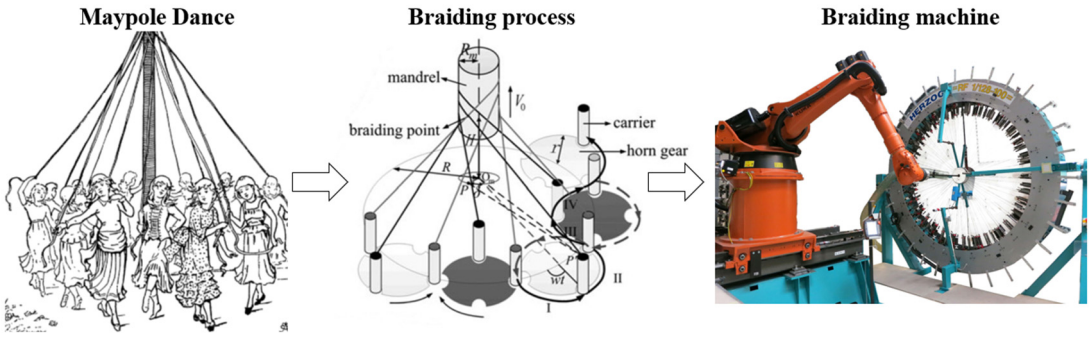

Fig. 1.4 The development of braiding technology.

As for the braiding method, the process characteristic of two-dimensional biaxial braiding technology is to transfer the yarn carrier through traditional intermeshing angular gears, allowing it to move simultaneously according to different rules. This makes three or more bundles of yarn, which are oriented in the direction of the formed fabric, twist, and group together and are arranged in a certain angle direction with the formed fabric, finally forming woven fabric [17–19]. With the diversified demand for composite components for their reinforcement properties, triaxial braiding technology has been developed in recent years. In addition to the traditional two groups of yarns, a third group of yarn is introduced along the forming direction (the axial direction) of the fabric to form an axial yarn system to enhance its axial properties. In addition, single-layer reinforced fabrics are difficult to meet the thickness requirements for making reinforcements in many applications, so multiple overlapping layers have been developed, but their basic structure is similar to that of single-layer braided structures.

1.2.2 Structures of braided fabric reinforcement

Unlike the weaving process, the braiding process is more suitable for the manufacture of flat or tubular fabrics. The types and patterns of fabrics prepared by the braiding

process are more diverse [20], as shown in Fig. 1.5. In this case, flat braided fabrics are made by a braiding machine with a closed loop track that has the same path throughout the bobbin carrier. Tubular braided fabrics are produced by the braiding machine with two closed tracks[21]. Depending on the coverage of the braiding traction, braids are further divided into open braids (coverage of about 80%) and closed braids (coverage of 100%) [22]. In addition to traditional two-dimensional braids, the braiding process can also increase the number of yarn systems so that the fibers inside the preforms interlace with each other in the plane and the thickness direction to form a complete three-dimensional braided preforms. Among them, the multilayer fabric angle interlocking method can maintain stable in-plane shear characteristics due to the designability of the structure and the flexibility of the braiding angle, thus promoting the stability, drapability and structural integrity of the composite.

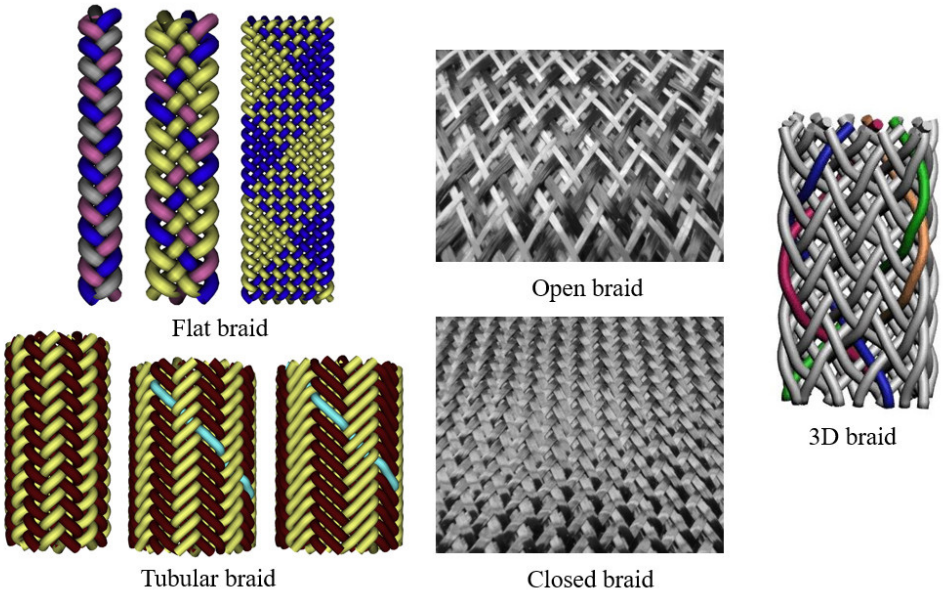

Fig. 1.5 Types of braided fabric reinforcement [21].

1.2.3 Types of braided fabric reinforcement

Although the basic principles and equipment of two-dimensional braiding technology are very similar, there are many specific types of braiding fabrics, as shown in Fig. 1.6. The two-dimensional braided fabrics are fibers or yarns that are evenly distributed on the plane of the fabric through two-dimensional braiding technology. According to the presence or absence of axial yarns, two-dimensional braided fabrics can be classified into two basic types biaxial and triaxial braiding [23]. During the

braiding process, the pattern of the fabric can be determined by the number of fuses set on the horn gear. Currently, the most commonly used braided structures include Diamond Regular and Hercules structures [24]. Diamond braids mean that one yarn continuously alternates from above and below another yarn; Regular braids mean that one yarn crosses above and below two other yarns in a repetitive manner; Hercules braids mean that one yarn repeatedly passes through the top and bottom of three other yarns. Due to the complexity of material selection, fabric shape and structure, it is difficult to simply and comprehensively represent the structure of two-dimensional braided fabrics in detail. The above structural representations only distinguish some commonalities of the fabric, the specific structures still need to be explained.

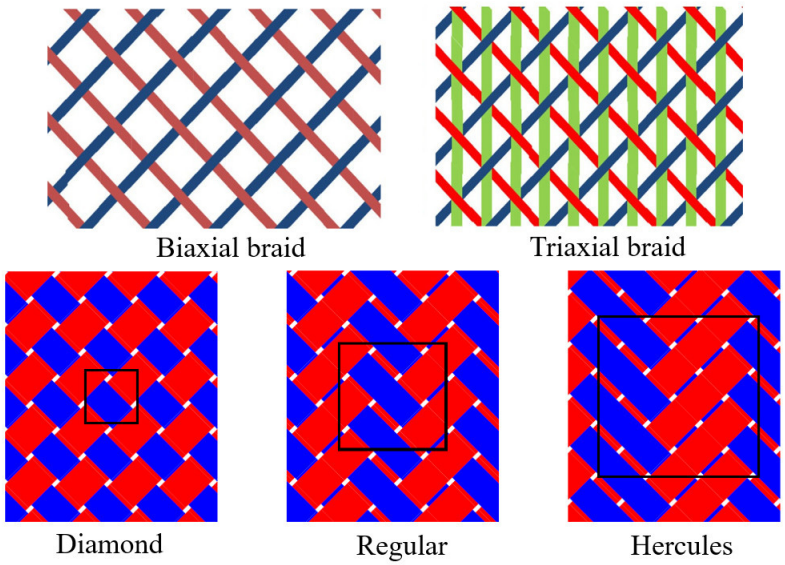

Fig. 1.6 Types of braided fabric reinforcement [22].

1.3 Textile preforming

1.3.1 Preforming technology

There are a variety of forming processes for textile composites. Depending on factors such as forming quality, forming efficiency and the ability to form complex shapes, two widely used processing methods are: Liquid Composite Molding (LCM) and Thermoforming.

(1) The Liquid Composite Molding (LCM) process includes more than ten different types of manufacturing processes [25,26], which can be summarized as injecting liquid matrix into a closed mold cavity with preforms, or heating and melting a resin film that

has been pre-inserted into the mold cavity so that the liquid matrix infiltrates the preforms and cures into composite parts. Resin Transfer Molding (RTM) (Fig. 1.7) as a type of forming in the LCM process, is often used to manufacture complex-shaped composite materials. It can be roughly divided into several steps such as preforming, resin injection, curing and demolding. It is worth noting that in the preparation of complex composite parts, the fabric needs to be preformed first to obtain the desired shape, and this process is called preforming process. Preforming process can be achieved by direct textile forming (Fig. 1.8 (a)), which produces relatively good density and quality of preforms, but has a long preparation cycle and high cost. Therefore, the stamping preforming process (Fig. 1.8 (b)) is gradually being studied and applied as an alternative process for the rapid forming of complex shapes with a short preparation cycle and low cost.

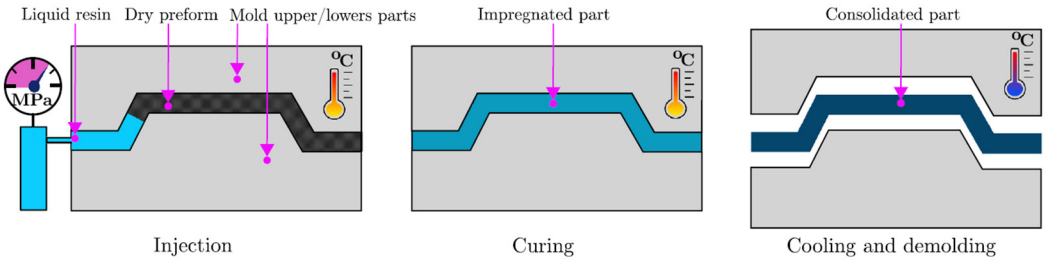

Fig. 1.7 Resin transfer molding injection process [27].

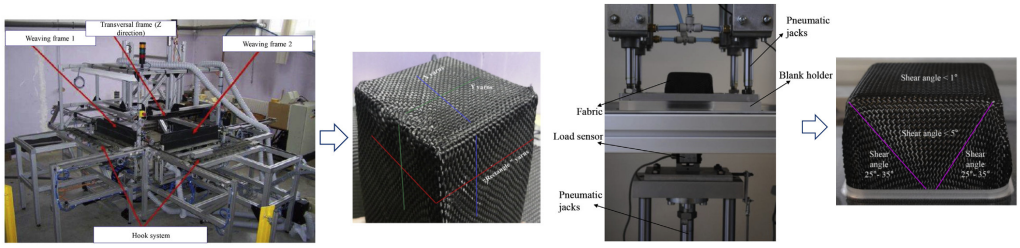

(a) (b)

Fig. 1.8 Classification of preforming process, (a) braiding preforming and (b) stamping preforming [28].

(2) Thermoforming process utilizes thermoplastic prepreg to manufacture composite parts [29]. The thermoplastic prepreg contains resin in the fibers, which eliminates the need for a resin injection stage during the forming process of composite parts. It avoids problems such as uneven distribution of resin and voids in the materials. At the same time, the manufacturing process of thermoforming is relatively fast and usually takes

only a few minutes to complete [30]. This provides the possibility of manufacturing composite parts in large-scale production. As shown in Fig. 1.9, the thermoforming process can be divided into the following steps: 1) heating the thermoplastic prepreg in an oven to the resin melting temperature; 2) transferring the prepreg to the corresponding mold; 3) closing the mold and applying pressure to the thermoplastic prepreg to make it into the desired shape; 4) waiting for the mold to cool and then demolding the composite part. The overall forming stage is similar to the RTM process, but the mechanical properties of the prepregs change during the heating stage, which cannot be ignored for the subsequent structural parts.

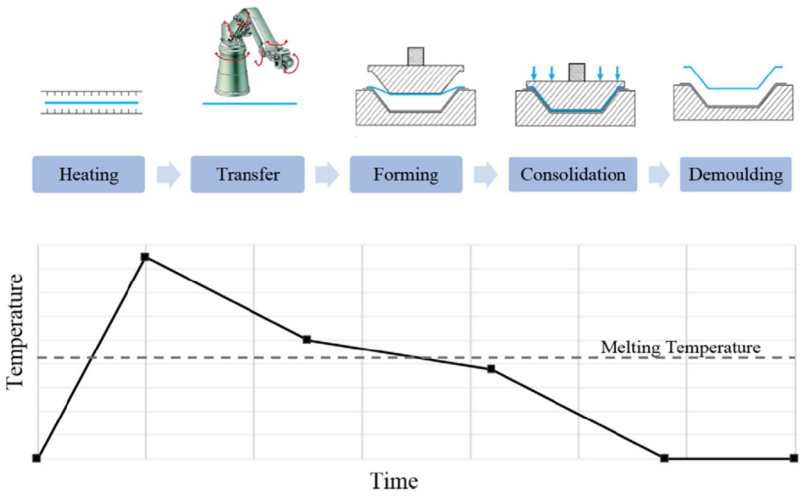

Fig. 1.9 Stages of the thermoforming [30].

1.3.2 Preforming defects

As mentioned above, during the preparation of composite materials with complex shapes, the dry textile preform needs to be preformed into the desired shape before resin injection, and this process is defined as the preforming process [31]. As the first step in the liquid molding process of composite materials, the quality of preforming in this process is crucial. The quality of the preforming largely determines the quality and mechanical properties of the final composite structure [32]. At present, preforming process has been used to manufacture hemisphere [33–36], double-dome [37–40] , square box [41,42], tetrahedron [28,43–45] and various more complex preformed shapes [46,47], as shown in Fig. 1.10. Studies have shown that the preforming process of the fabric is a challenging task. The parameters of the preform and the preforming process parameters affect the deformation behavior of the fabric [48]. Improper process parameters will cause behaviors such as yarn slippage, in-plane shear, interlayer slip,

and draw-in. These deformation behaviors can induce various defects in the fabric, as shown in Fig. 1.11. Wrinkling is one of the most common defects on a macro scale. Boisse et al. proposed that the weak bending stiffness of textiles causes slippage between fibers, resulting in frequent wrinkling [49]. In order to study the formation of wrinkles, many researchers have attempted to reduce wrinkling by changing the pressure of the blank holder. S. Allaou et al. [44] pointed out that in order to obtain no wrinkle fabrics, blank holder is necessary. In addition, Labanie et al. [48] found through experiments that the process parameters have a certain influence on the yarn tension and contact stress. If the pressure of blank holder is too high, the yarn jamming occurs in the stretched deformation area of the fabric. This resulting in uneven distribution of fiber bundles and causing defects.

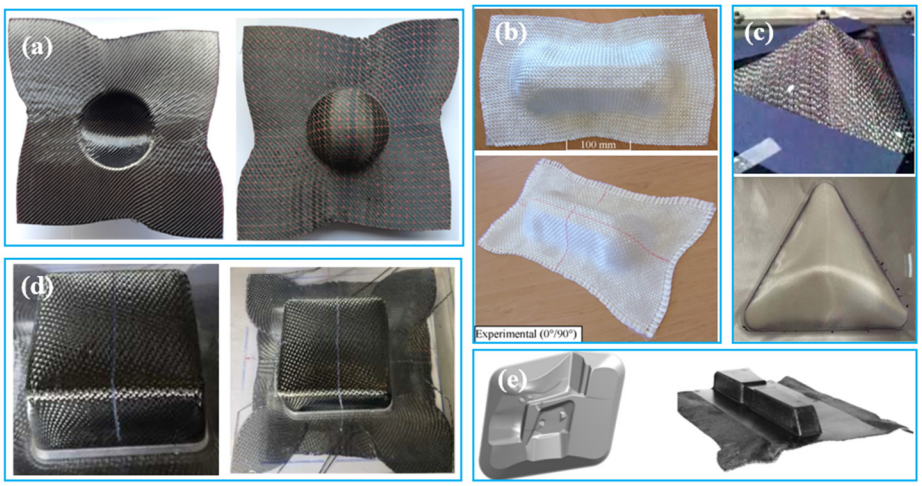

Fig. 1.10 Preformed shapes, (a) hemisphere [36], (b) double-dome [40], (c) tetrahedron [44,50], (d) square box [41] and (e) complex shapes [46,47].

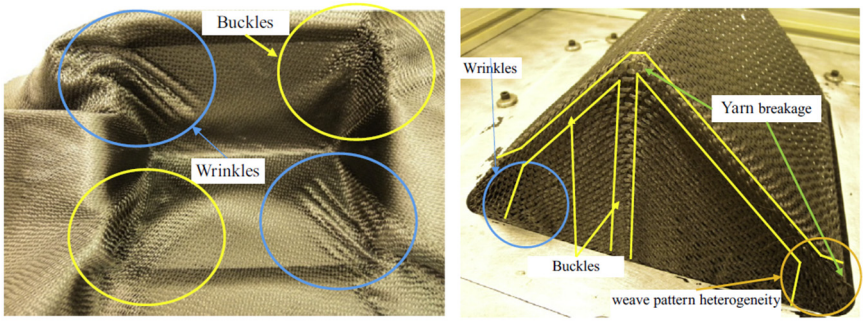

Fig. 1.11 The preforming defects[51].

Buckling, breaking, and misalignment are also common defects that occur during the

preforming process of the fabric [52–54]. These defects can cause uneven resin flow in the matrix, negatively affecting the shape and mechanical properties of the completed composite component. Gatouillat et al. [55] found through simulation studies that yarn slippage during the preforming process can cause the internal structure of the preform to loosen, reducing its mechanical properties. It can also cause uneven matrix resin distribution in the composite material after forming, which can easily lead to stress concentration, thereby reducing the mechanical properties of the composite structure. The deformation properties of triaxial braided composite reinforcements during the manufacturing process were studied [56]. Manufacturing defects such as fiber vacancies, buckling and gaps existed in the preforming process of triaxial braided fabrics. The longitudinal and radial sliding of yarns became the main preforming behavior. The literature also pointed out that the braiding angle directly affects the variation of the fabric deformation performance and is a key parameter for the deformation performance of braided fabrics. A large number of studies have analyzed the deformation behavior of textile preforms in the preforming stage and established the relationship between defects and preforming process parameters to optimize the preforming process. However, most of them focus on woven preforms, and there are relatively few studies on the deformation behavior of braided preforms during the preforming process. Therefore, it is necessary to master the deformation behavior and mechanical properties of braided preforms to improve the forming quality of preforms plays a decisive role in improving the performance of composite materials with special-shaped complex structures.

1.4 Mechanical properties and characterization of the textile preform

From the previous discussion, it is clear that the exploration of the mechanical properties of composite components and characterization of complex structures has become a top priority in the preparation of composites. This is mainly influenced by several factors, including the mechanical properties of the reinforcement (fibers) and matrix (resin), the interfacial properties between fibers and resin, and the resin infusion process. As mentioned in section 1.3, the preparation of complex structures composite components requires textile preforms to undergo a preforming process to obtain the desired shape. Therefore, the mechanical properties of the preforms in the forming process directly affect the mechanical properties of the formed composite parts. This is mainly because, during the preforming process, the mechanical properties of the fabric

determine its deformation behaviour, which results in different forming defects. Therefore, a comprehensive exploration of the basic mechanical properties of the preform is of great significance for improving the overall mechanical properties of the component, and also to improve the final forming quality of the component.

The mechanical behavior of textile-reinforced materials during the forming process has been extensively studied. A large number of studies have focused on understanding the mechanical behavior of the reinforcements through experiments and determining parameters for material constitutive models, which in turn facilitates the application of simulation methods. The basic mechanical properties of textile preforms during forming process include tensile, shear, bending, and compression properties. Gerekeereke et al. summarized the experimental characterization methods for the mechanical properties of textile structures [57]. Bussetaa [58] et al. also proposed testing methods for determining the tensile stiffness, shear stiffness, bending stiffness, and contact surface friction of fabrics. To characterize the deformation properties of fabrics, reveal the deformation mechanism and accurately predict the complex shapes of fabric forming. This thesis focuses on the tensile, shear and bending behaviors during the textile fabric forming process to provide data support for simulation analysis.

1.4.1 Tensile properties

Since the axial tensile stiffness of the yarn is much greater than the other stiffnesses in the transversal direction, the axial direction of the yarn becomes the direction of the maximum tensile stiffness of the textile preforms. Therefore, the orientation of the yarn has a significant impact on the mechanical properties of the preforms. The tensile stiffness is mainly determined by uniaxial tensile tests. The uniaxial tensile test not only determines the tensile stiffness of a single yarn (Fig. 1.12 (a)) but also determines the tensile deformation capacity of the 2D textile structures (Fig. 1.12 (b)). In the uniaxial tensile test, the yarn exhibits a linear behavior in the initial stage of loading, which is different from the tensile behavior of the 2D fabrics. The tensile behavior of the fabric shows a non-linear evolution in the initial stages of loading [57,59–61], which is related to the fluctuations of yarns, especially the number of curls and the curl amplitude of the yarns in the fabric [59]. In addition, considering the interlocking contact between yarns in two-dimensional fabrics, the coupling between the two yarns also affects the tensile state of the fabric. In this case, the uniaxial tensile test cannot accurately describe the tensile behavior of the fabric. In order to characterize the tensile coupling between yarns,

Bossie [62] used a biaxial tensile test to study the biaxial tensile coupling properties of woven fabric by applying tensile loads to the warp and weft directions, as shown in Fig. 1.12 (c). The device can adjust the strains corresponding to the warp and weft directions to obtain different strain ratios and measure them by mechanical extensometer or optical methods. At the same time, the load in each direction is output by a load sensor. Fig. 1.12 (d) shows the biaxial tensile test results of 2-2 twill carbon fabrics with different strain ratios.

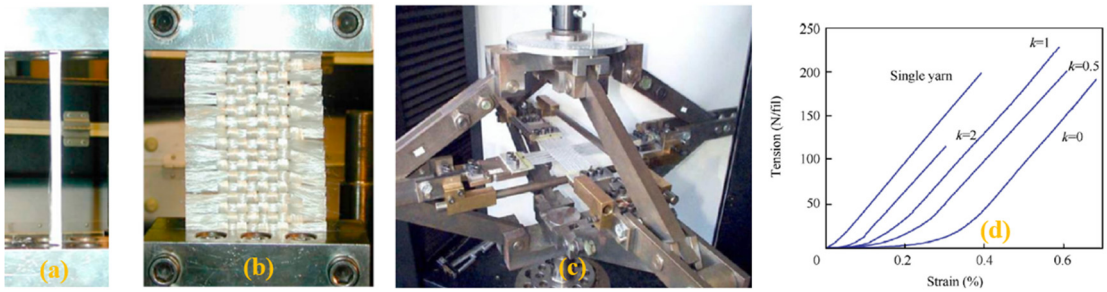

Fig. 1.12 Tensile test of textile materials, (a) single yarn [63], (b) uniaxial tensile of fabric [63], (c) biaxial tensile of fabric [64] and (d) tension-strain curves of different ratios $k = \varepsilon_{11}/\varepsilon_{22}$ [64].

1.4.2 In-plane shear properties

In-plane shear deformation is one of the most important deformation modes in the forming of textile preforms, which is mainly manifested as the reduction of the angle between interlaced yarns. The reason why textile composites can be manufactured into complex shapes more easily is mainly due to the shear deformation mode of the preform. As in-plane shear is the key deformation mode of the hyperboloid structure in preforms, it is closely related to the final shape of the component. Moreover, shear deformation can also cause wrinkles to form in the forming process of fabric, affecting the forming quality and mechanical properties of components. At present, the shear deformation of fabric is mainly studied through the picture frame test (PFT) and bias-extension test (BET) [57,65–68], shown in Fig. 1.13. Both of these methods were tested with single-layer preforms, which were first started in the early 1960s. After many years of development, they have been widely used in the characterization of in-plane shear properties of woven preforms [66,69–71].

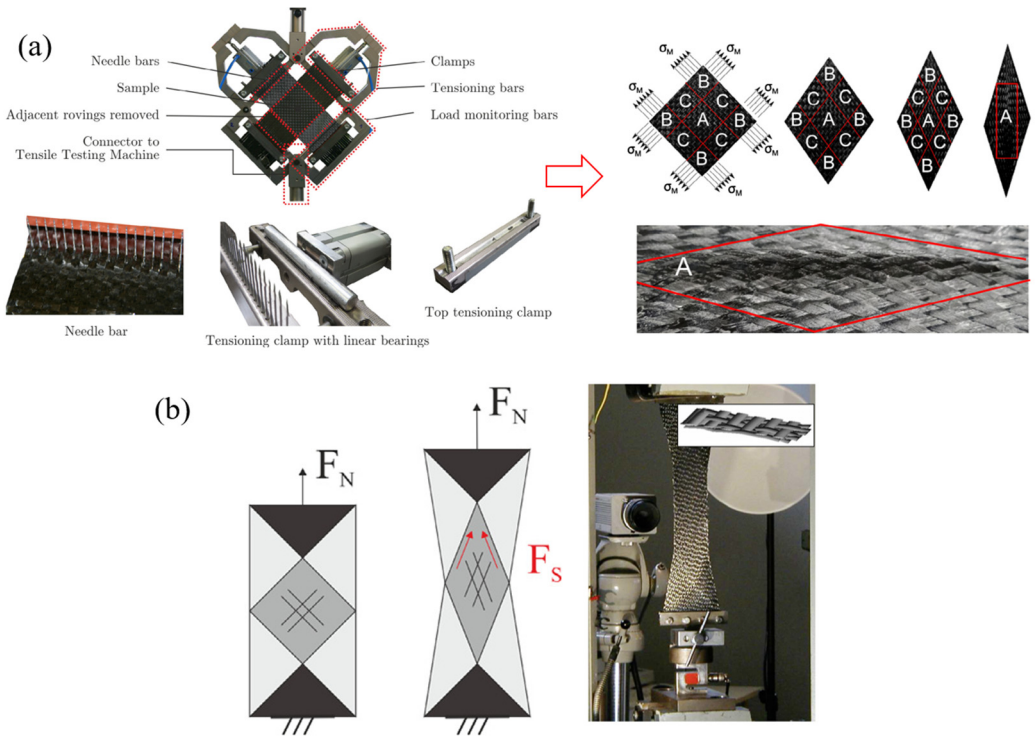

Fig. 1.13 Two principle methods to identify in-plane shearing properties of textile fabrics, (a) picture frame test [72] and (b) bias-extension test [73].

The frame used in the picture frame test is made up of four equal-length rigid rod hinges. When the frame is fixed on the stretching machine, the machine will apply a force along the diagonal direction of the frame, and the intersecting connecting rods rotate close to each other, causing the frame to gradually evolve from an initial square into a diamond frame. The cross-shaped single-layer woven fabric is fixed in the frame, and the fabric undergoes in-plane shear behaviour under the action of force. Fig. 1.13 (a) represents the deformation of the experimental sample. In the ideal conditions, the fabric is subjected to pure shear deformation under a constant in-plane shear force in the tensile test [74,75], and the yarn is not subjected to tension along its axis during the experiment. This requires that the fiber should be aligned with the edges of the frame when the fabric is clamped to avoid stretching the fibers. Otherwise, the high tensile stiffness of the fiber will cause a large error in the measurement of the shear curve. Launay et al. [76] measured the tension of yarn during the PFT and found that yarn was subjected to a certain tension. At the same time, they proved that the in-plane shear behavior of the fabric will be affected by the tension of the yarn when the two ends of the yarn are installed in the picture frame under the state of tension. Therefore, to ensure the accuracy of the experimental results, it is necessary to avoid the yarns in the

tensioned state when the picture frame tensile test is used to analyze the in-plane shear behaviour of the textile preforms.

Bias-extension test is another commonly used method to characterize in-plane shear properties of woven fabrics. Compared with PFT, BET has certain advantages in accuracy and portability, especially for studying in-plane shear and tensile properties of preforms at high temperatures. Due to the free boundary conditions, the yarn has no tension in its direction except for the small tension of the interaction between warp and weft, so the influence of yarn tension on shear performance can be reduced. The sensitivity of the bias-extension test to deviation is lower than that of the picture frame test, and there is no need to design a special clamping structure. Based on the advantages of the bias-extension test, exploring the characteristics of shear and tensile mechanical properties within the woven preforms has become the focus of research at this stage. In the bias-extension tensile test, the woven fabric was cut into a rectangular shape with a length-to-width ratio ≥ 2 [77], and the warp and weft yarns were oriented at 45° to the loading direction of the tensile force. When the two ends of the preforms are subjected to tension, the intersecting yarns first undergo rigid rotation around the interweaving point and the fabric exhibits in-plane shear behavior. In this case, the main resistance to in-plane shear comes from the friction between the yarns. Therefore, the shear force of the fabric is small at the initial stage, and when the intersecting yarns come into contact with each other, transversal compression is generated. Then, the in-plane shear of the fabric ends, the angle between two yarns reached the critical locking angle [78–80], the tensile force increases rapidly and the fabric fails to bear the load. For the bias-extension test, it's assumed that the fibers are not stretchable and the yarn does not slip, the fabric will present three distinct partitions, such as no shear zone A, half shear zone B and pure shear zone C shown in Fig. 1.13 (b) [73,81–83]. However, there are some limitations to the pure shear deformation in zone C, as it assumes that the fiber bundles are inextensible and there is no relative slippage between them. Nevertheless, due to the free ends of the fiber bundles in zone C, large shear deformation can easily induce interlayer slip of the fiber bundles, affecting the actual shear deformation behavior [65,84,85].

The shear behavior of fabrics is usually characterized by the shear angle. Assuming that there is no slippage during the test, the shear angle can be determined by the global displacement. The analytical model of displacement and shear angle can be quickly obtained during the stretching process. In addition, the direct optical measurement

method of shear angle is widely used to eliminate the influence of slippage. Harrison et al. [86] used the digital image correlation (DIC) to measure the shear angle and check the deformation uniformity of the fabric. It is worth noting that when defects are present in the specimen, the DIC measurement results may be inaccurate. An improved transversal tensile test was proposed to study the shear-tension coupling and wrinkling behaviour in detail [77]. When analyzing the in-plane shear mechanical properties of the fabric, it is not enough to explain and describe the change in the shear angle. By determining the shear force that causes the change of the shear angle, the shear moment can be calculated to provide a more comprehensive description of the in-plane shear behavior of the preform.

As mentioned above, current research on the in-plane shear and tensile properties of textile preforms is mainly focused on woven fabrics, as the variability of the braiding angle in braided preforms brings some difficulty in the mechanical analysis. Therefore, further research is needed to improve the understanding of the in-plane shear and tensile properties of braided preforms. Potluri and Manan et al. [87] proposed a micro-mechanical model based on tensile experiments under special conditions that can describe the in-plane shear behaviour of braided preforms. Rosso et al. [88] investigated the tensile properties of biaxial braided preforms (less than 16 yarns) prepared from Kevlar and found that the braiding angle exerted an important influence on their mechanical properties. In addition, the tensile experiment of biaxial braided preforms showed that the strain along the axial direction of the preform increased with the increase of the braiding angle [89]. Guzman-Maldonado [90] studied the in-plane shear behavior of non-orthogonal fabrics by conducting PFT. Xiao et al. [91] proposed an analytical model for characterizing in-plane shear behavior for two-dimensional braided preforms and considered the effect of yarn compaction in a subsequent study to analyze the transition from compacting to slippage of yarn during BET.

1.4.3 Bending properties

During the forming process of preforms, the bending behavior of fabrics is often neglected [92]. The bending stiffness of preforms is lower than that of composites due to the absence of matrix bonding between the fibers in the preform. However, many studies have shown that the bending properties have an important influence on the simulation of forming, especially for the characterization of wrinkles. The size, shape and number of wrinkles are all affected by the bending behavior [57,93]. Studies have

shown that a larger bending stiffness increases the number and size of wrinkles. When the fabric is bent, slippage occurs between the fibers, resulting in a low bending stiffness of the fabric[94]. But, the wrinkles of the fabric change after the bending stiffness is considered in the forming simulation, as shown in Fig. 1.14. Bossie et al. [43,95] considered the effect of bending stiffness in the fabric forming simulation, the number of wrinkles in the simulation results decreased and the size increased, which in turn more accurately predicted the deformation of the fabric (Fig. 1.15). The bending deformation mechanism of preforms is complex, which is manifested in transverse shear and local transverse compression on the fabric, and relative slippage and buckling on the yarn. Currently, the standard tests used to measure the bending properties of fabrics mainly include the Peirce cantilever test, the Kawa-bata bending test and the three-point bending test. Since the three-point bending test is mainly used to measure fabrics with thickness, this chapter focuses on the methods used to measure the bending stiffness of single-layer two-dimensional fabrics.

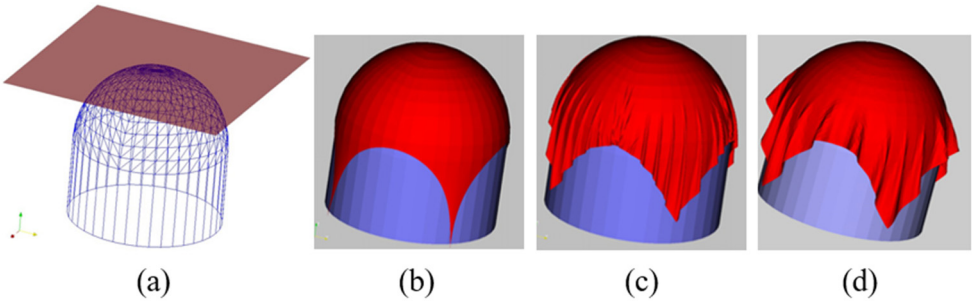

Fig. 1.14 Draping on an hemisphere, (a) initial geometry, (b) tensile stiffness only, (c) tensile stiffness + in plane shear stiffness and (d) tensile stiffness + in plane shear stiffness + bending stiffness [43].

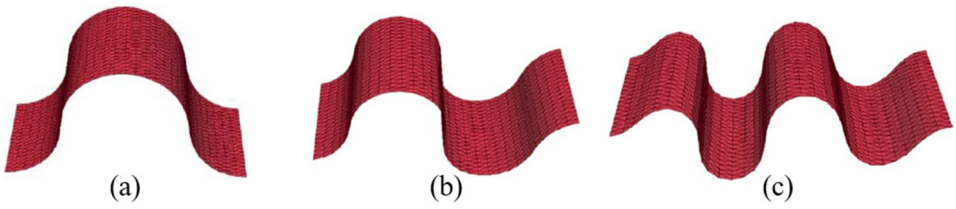

Fig. 1.15 Compression in the yarn direction of a woven reinforcement with different bending stiffness, (a) 1Nmm^{-1} , (b) 5Nmm^{-1} and (c) 10Nmm^{-1} [96].

(1) The Peirce cantilever beam method: This method was developed in the 1930s [97,98]. It is based on the principle that the textile cantilever bends under its gravity.

Due to its simple operation and wide applicability, it has been used in bending tests of dry fabrics and prepregs. It can be combined with optical measurement techniques to measure the deformation of the specimen conveniently and quickly. The cantilever beam method assumes that the bending stiffness of the fabric is constant, as shown in Fig. 1.16 (a). A rectangular fabric specimen was placed on a horizontal platform and extended slowly along the horizontal direction. The fabric was bent under its gravity until the tip of the cantilever touched the three-dimensional inclined plane, and the bending stiffness was calculated according to the corresponding formula. The initial inclination angle of the three-dimensional inclined plane was 7.1°. Later, for the convenience of calculation, some scholars positioned the inclined plate angle at 41.5° [55,99,100].

The accuracy of the bending stiffness calculated using the cantilever beam bending method needs to be improved. Lammens et al. [101] found that the bending stiffness calculated using the conventional cantilever beam test method has a certain error, which ignores the effect of higher-order effects. Since the bending stiffness of fabric has some nonlinearity, Bilbao et al. [102] proposed an optically assisted test method for measuring high curvature bending properties. The device used for this test is shown in Fig. 1.16 (b), which includes a mechanical part and an optical part. The free end of the specimen is suspended under gravity or a certain mass is suspended at its free end to achieve high curvature bending. The bending shape of the specimen is captured by a camera to record the deformation process of the entire fabric, and the bending moment-curvature curve is plotted to characterize the bending stiffness for measuring woven fabrics with different structures, thicknesses and bending stiffnesses. Based on this, Liang et al.[103] used the device (Fig. 1.16 (c)) to conduct bending tests on 2D fabrics, 3D laminated fabrics and 3D woven fabrics, and obtained the curvature by fitting the bending states of specimens with uniform quartic B-spline curves. In addition, Liang et al. also characterized the bending behavior of thermoplastic prepreg and proposed a cantilever beam test device that could control the ambient temperature for testing. Due to the possible distortion caused by nonlinear load effects during the preform draping, SHERWOOD et al. [104] proposed a vertical cantilever beam method. The preform was suspended vertically and the load was applied to its free end. The displacement of the specimen was recorded by a camera and the bending curvature was calculated. Based on this method, Alshahrani et al. [105] tested the bending behavior of thermoplastic prepregs at high temperatures using a test device with radiant heating shown in Fig.

1.16 (d). The bending stiffness of the prepregs decreased with increasing temperature until the thermoplastic resin melted and the bending stiffness remained constant. The bending stiffness was also affected by the loading rate, with a higher loading rate resulting in a larger bending stiffness.

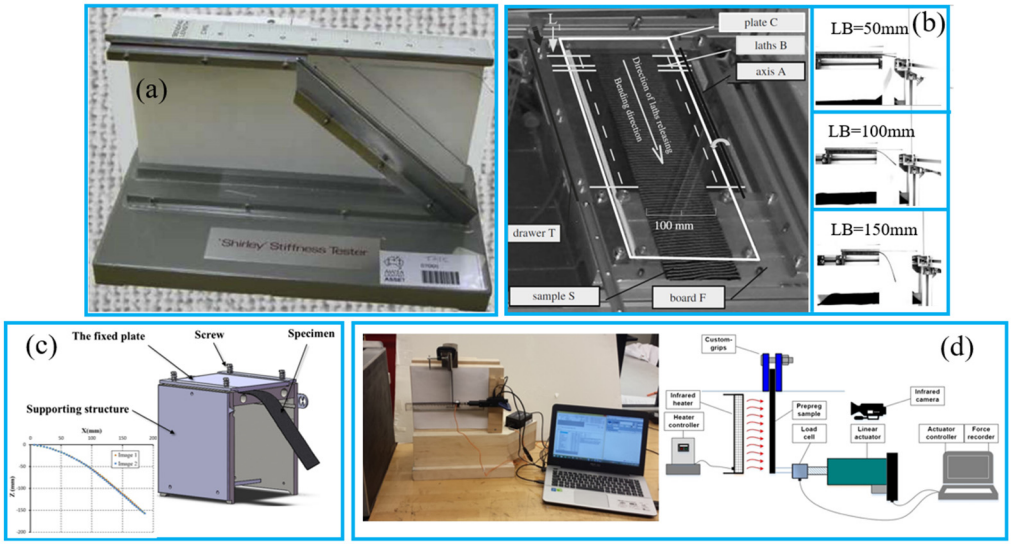

Fig. 1.16 The Peirce cantilever beam method, (a) standard cantilever bending test [94], (b) new flexometer-cantilever bending test fixture [102], (c) support for the high thickness specimen clamping [93] and (d) vertical cantilever bending test system [105].

(2) Kawa-bata bending test: This method is another method to measure the bending properties of fabrics, which was developed in 1980 [102,106]. It mainly investigates the effect of the loading rate and the cyclic loading on the bending stiffness of the fabric. As shown in Fig. 1.17, this test ensures that the specimen undergoes pure bending deformation during the test, to measure the mechanical properties of the preforms in pure bending. In addition, the device allows obtaining the variation of the bending moment per unit width of the specimen with curvature. By using this device for bending cyclic loading tests, the nonlinear relationship between bending moment and curvature of the preform can be obtained. Furthermore, a rheometer bending test device has also been developed to control the temperature and bending rate during the experiment and to study the dependence of fabric bending stiffness on temperature and loading frequency.

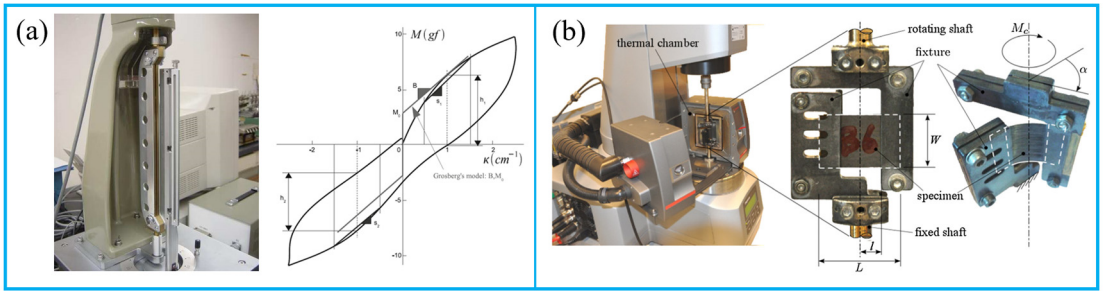

Fig. 1.17 Kawabata bending test, (a) KES-FB2 device [102] and (b) rheometer bending test device [107].

1.5 Modelling approaches for the simulation of the textile forming

For the forming research of textile composites, the characterization of the mechanical properties of preform based on the experiments requires high time and cost. It is difficult to conduct characterization tests on certain parts of the fabric, so the numerical simulation of the textile composites is of great significance for the forming process. It can predict the feasibility of the fabric forming process and the generation of defects under given conditions, which is beneficial to reduce the "trial and error" process in the forming stage. Since the textile preforms are composed of thousands of continuous fibers and have multi-scale characteristics, they are usually divided into three scales, i.e. macroscale (part-mm), mesoscale (yarn-10^{-1} mm) and microscale (fibre -um) [58,64,108], as shown in Fig. 1.18.

(a) At the macroscopic scale, the fabric is considered a continuous material. The overall deformation and the formability of the preforms are mainly studied to predict defects such as wrinkles, yarn slippage and buckling, etc [49].

(b) At the mesoscopic scale, the studies mainly focus on a large number of intersecting yarns and representative unit cell (RUC) that can represent the periodic structural fabric, considering the interaction between yarns to determine the local characteristics of the reinforcing material [109]. This scale allows the calculation of the final mechanical properties of the component as well as the permeability of the deformed reinforcement to predict damage and virtual mechanical tests, which can be used to simulate the resin injection step. However, the simulations at this scale are limited to small areas, and it is difficult to simulate the entire sections when considering the number of yarns and their complex interactions.

(c) The microscopic scale is the smallest scale for simulating textile composites. On

this scale, fiber monofilament is the most basic constituent, such as carbon fiber, glass fiber, aramid fiber, etc. The contact and interaction between fibers are considered, the defects are characterized by establishing beam element models, such as fiber fracture.

The different features and defects mentioned above need to be detected and characterized at different scales, so multi-scale modeling is very important. Considering that the object of this paper is a preform and its mechanical characterization mainly reflects in the macroscopic aspect. So, this thesis focuses on modeling and simulation analysis at the macroscopic level.

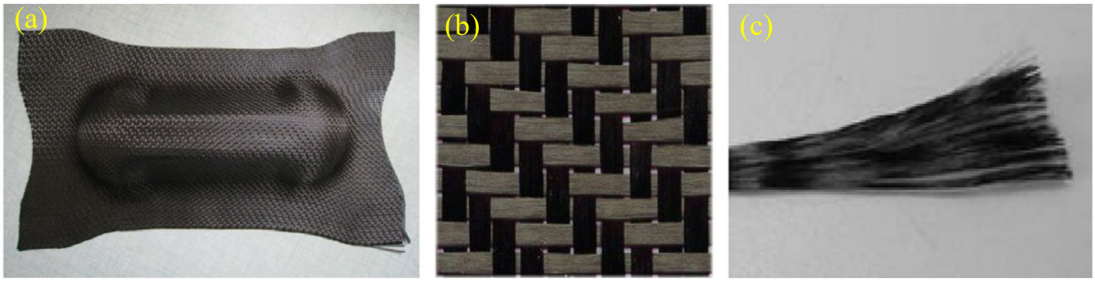

Fig. 1.18 Three different scales of textile reinforcements [108], (a) Macroscopic scale, (b) Mesoscopic scale and (c) Microscopic scale.

Macroscopic numerical simulations mainly include geometric methods based on kinematic descriptions and mechanical methods based on finite element techniques [58]. The kinematic approach, also known as the mapping approach or the fishnet approach, is a purely geometric approach that allows the calculation of the fiber orientation after the deformation of the textile composites [110]. This method does not take into account mechanical behavior and cannot predict major defects and problems such as wrinkling. The mechanical method, also known as the finite method, is based on the material constitutive model to predict the mechanical deformation of textile materials. In the mechanical model, fibers and yarns do not appear in the model. The components of the fabric and their interactions are not studied. The complexity of this model lies in the material behaviour laws. Since textile preforms are non-homogeneous materials, numerical simulation methods for preform forming can be classified into discrete, semi-discrete and continuous methods [111].

1.5.1 Discrete approach

The discrete approach studies the mechanical behavior of fabrics at the microscopic scale [112,113]. This approach takes a single yarn as the object, and each yarn is

modelled. At the same time, it considered the contact between adjacent yarns. It can provide changes in the yarn of the fabric due to deformation and facilitates the calculation of the fabric permeability and the volume fraction of the fibers. As described in reference [114], the microscopic discrete models of preforms require the calculation of a large number of fibres and their contacts, which translates to a computational effort and computational time. In the existing discrete methods, the digital element approach has been proposed and used to simulate textile processes [115], as shown in Fig. 1.19 (a). Each yarn is discretized into rod elements, and the elements are connected by smooth hinges, which the contact behavior between yarns is simulated using contact elements. Based on the single-chain digital element, Zhou et al. [116] further simulated the fibre monofilament in the yarn and constructed a "multi-chain digital element", shown in Fig. 1.19 (b). Said et al. [117] used the "multi-chain digital element" method to simulate the compaction process of large-scale 3D fabrics and accurately predicted the internal structure of the fabric after deformation.

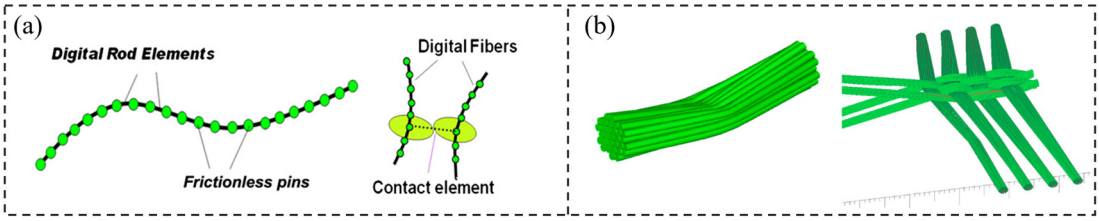

Fig. 1.19 Digital element approaches, (a) single-chain digital element and (b) multi-chain digital element [118].

Starting from the concept of the digital element method, a nodal modeling approach using rods and springs interconnected is proposed [119]. It used the different connections to achieve different deformation models and simulated the response of materials in terms of extension, shear, torsion and bending, as shown in Fig. 1.20. In addition, an approach of virtual fibers at the microscopic scale is also proposed and the geometric model is generated by connecting 3D truss or beam elements. Various textile preform models are established based on the virtual fiber approach as shown in Fig. 1.21, including non-wrinkles fabrics [120], two-dimensional fabric layers[121,122], weft-knitted fabrics [123,124], and three-dimensional woven preforms [125,126]. The discrete method is rarely used for forming analysis of textile-reinforced materials due to its high accuracy and difficulty in obtaining the internal stress state of the material.

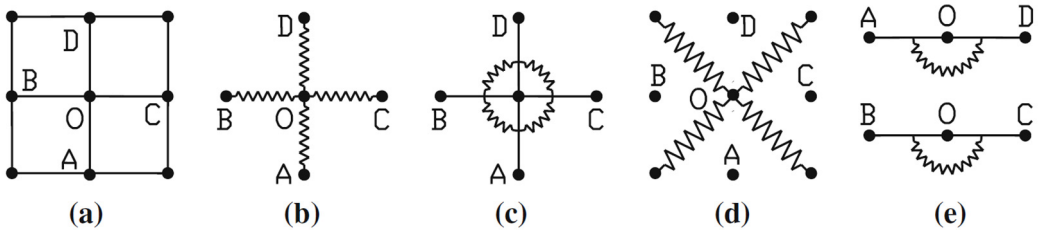

Fig. 1.20 The discrete modelling approach, (a) the typical 'O' discrete model, (b) linear springs for stretch, (c) torsion, (d) diagonal linear springs for shear and (e) bending [119].

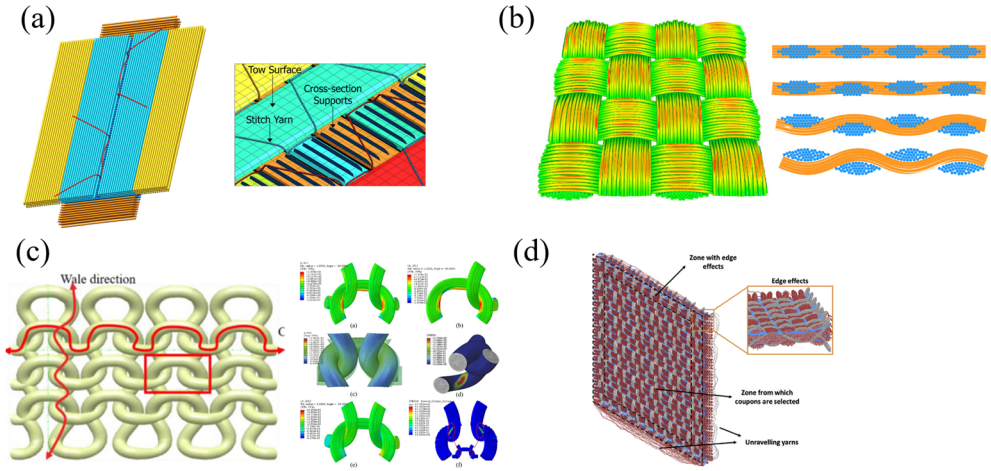

Fig. 1.21 The virtual fiber approaches, (a) non-crimp fabric [120] and (b) 2D woven fabric [121], (c) weft knitted fabric [123] and (d) 3D woven fabric [125].

1.5.2 Semi-discrete approach

The semi-discrete approach [127] is intermediate between the discrete and continuous approaches and is used to define the structure of yarns. The microstructure of fabrics is obtained by considering the effect of different deformations on the internal nodal loads of yarns. In the semi-discrete method, the fabric is considered to be composed of a certain number of discrete elements. Hamila and Boisse et al. [128] developed a three-node finite membrane element based on the semi-discrete method, shown in Fig. 1.22 (a). On this basis, a three-node shell element was also proposed and used to mesh the reinforcements. This method takes into account the tension-locking phenomenon and assumes that the warp and weft directions are arbitrary on both sides of the element to avoid locking [129]. The semi-discrete approach considers the contribution of the material's tensile stiffness, in-plane shear stiffness and out-of-plane bending stiffness to the internal loads of the element. In particular, the tensile and in-

plane shear behaviors are described using three nodal shell elements, while the bending behavior is described by two adjacent shell elements. In addition, an 8-node hexahedral elements (Fig. 1.22 (b)) are also proposed to simulate 3D interlock composite preforming [130].

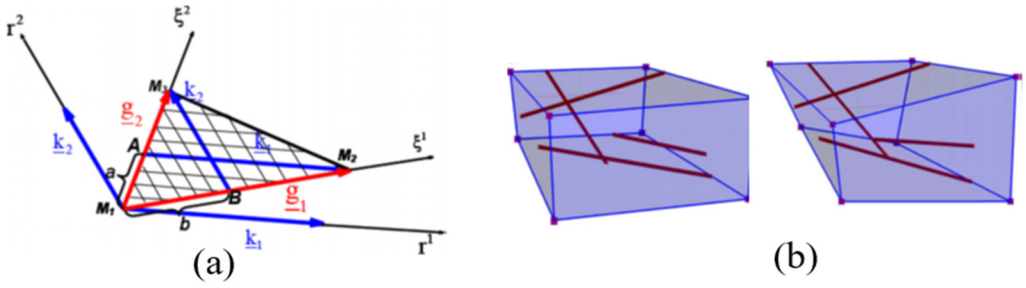

Fig. 1.22 The semi-discrete approaches, (a) three-node finite membrane element [129] and (b) 8-node hexahedral elements [130].

In the existing literature, semi-discrete approaches have been widely used for the textile draping process, as shown in Fig. 1.23. It defines the relationship between load and strain fields and uses the principle of virtual work to establish the relationship between external virtual work, internal virtual work and acceleration virtual work. Among them, the internal virtual work is mainly composed of three parts: tension, in-plane shear and bending. Meanwhile, the parameters in the principle of virtual work are measured by experimental methods. At present, the semi-discrete method has been successfully applied in the simulation analysis of hemispherical draping [43,130], tetrahedral forming [44], square box preforming [28] and its effectiveness has also been confirmed. In hemispherical draping, a simplified form of virtual internal work was used to analyze the role of three kinds of stiffness (tension, in-plane shear and bending) in the wrinkling simulation [43]. It pointed out that in the double-curved forming process, the in-plane shear stiffness is the main reason for wrinkling, the shear angle is not directly related to wrinkling, and the bending stiffness mainly determines the shape of the wrinkling. The forming process of tetrahedron shows that the shear angles calculated using the semi-discrete simulation method agree well with the experiment [44]. The correct shape of the fold was obtained by this method. The simulation analysis also found that the pressure on the blank holders has an important effect on the wrinkles, it can avoid repeating experiments to obtain these conclusions. The distribution of shear angle obtained by the box preforming simulation using the semi-discrete method is

consistent with the experiment. Wrinkles can be observed at the corners of the box, and applying higher pressure at the corners increases the risk of wrinkling and slippage. Furthermore, predicted wrinkling under different forming conditions for the square box using the semi-discrete approach. In the subsequent research work, the semi-discrete method was also applied to the simulation of thermoforming of multilayer composite preforms [131].

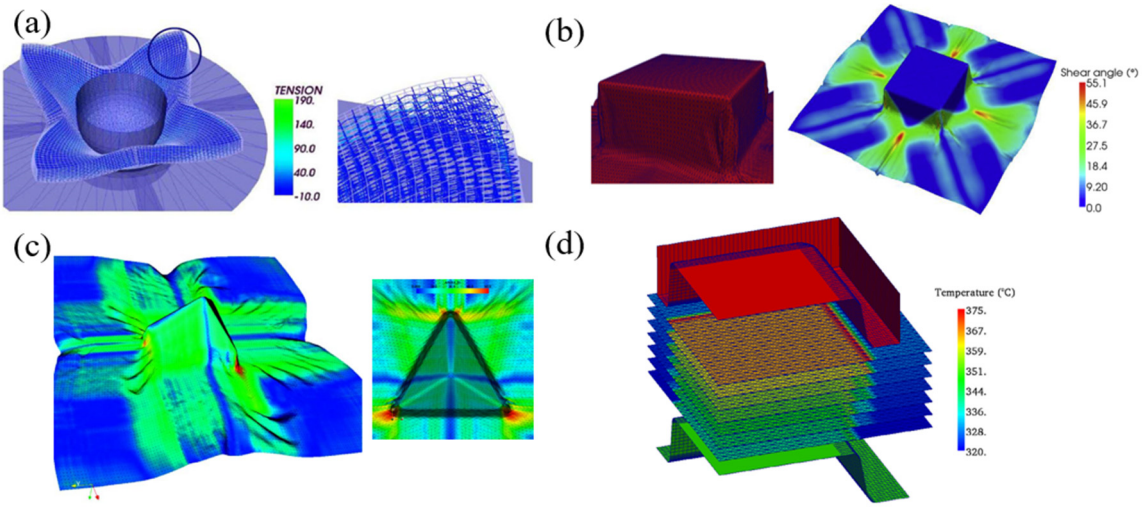

Fig. 1.23 Applications of semi-discrete approach, (a) hemispherical draping [130], (b) square box preforming [28], (c) tetrahedral forming [44] and (d) thermoforming of multilayer composite preforms [131].

1.5.3 Continuous approach

In the actual simulation process, in addition to selecting the suitable simulation method, the efficiency of the simulation also needs to be considered. Based on the discrete and semi-discrete approaches, continuous approaches have been proposed and used to characterize the deformation of fabrics [38,132,133]. This method can effectively improve the simulation efficiency. The continuous approach treats the preforms as a continuum and does not consider the structure inside the preforms, the mutual friction and extrusion between the yarns, etc. It is based on the theory of continuum mechanics to study the macroscopic mechanical response of the fabrics to the external load, and then obtain the load-deformation curve. This method is not only easy to implement in finite element software but also has high computational efficiency, which can predict the shape and mechanical properties of the final component. The key to this method is to select a suitable constitutive model that responds to the specific

mechanical properties of the fabric and to determine the material parameters through corresponding mechanical tests. Since textile structures exhibit anisotropy and large shear and bending deformations, different continuum models have been developed and used to describe the mechanical behavior of textiles. Currently, numerical simulation methods have been developed including non-orthogonal rate-independent models, hypoelastic models and hyperelastic models, etc., as shown in Fig. 1.24.

Peng and Cao [134] developed a non-orthogonal constitutive model for woven fabrics under large deformations to characterize the anisotropic material behavior of fabrics. A convective coordinate system was introduced to decouple the tension and shear of the fabric. It simplifies the material characterization of the woven fabric. Additionally, a fiber orientation model was established to track the yarns' orientation during the deformation of the fabric. The prediction results of the non-orthogonal model were in good agreement with the experimental results, while the prediction results of the orthogonal model are quite different. Furthermore, Yu et al. [135] developed another new non-orthogonal constitutive model, which well explained the influence of differences in fiber strength and orientation on the anisotropic behavior of reinforcements. It also pointed out that the new constitutive model successful simulated the shearing behavior without significant length change.

In the condition of large deformation of fabrics, the hypoelastic and hyperelastic models have also been proposed. The hypoelastic constitutive model mainly reflects the relationship between the constitutive tensor and the strain rate. It's shown that using hypoelastic law with an objective derivative based on the warp and weft fibre rotation tensors can correctly trace the specific behaviour of the woven materials [40]. A hypoelastic constitutive model for fibrous materials was proposed and extended to the forming simulation of textile materials with two fiber orientations. The objective derivative of the model is defined by fiber rotation, which can be implemented in Abaqus software [136]. A stress resultant shell method considering independent bending and tensile stiffness is proposed, which simulated the draping process of textile composite reinforcements with continuous fibers by relating the stress moment to membrane strains and curvatures according to hypoelastic laws [137]. Within the framework of non-orthogonal hypoelastic material laws, a finite element model for solving highly non-linear fabric forming problems was proposed and embedded in shell or membrane elements. The model can characterize the mechanical behavior of fabrics and improve the formability of multilayer preforms [138].

When the hyperelastic model is used to simulate the macroscopic mechanical behavior of fabrics, it is necessary to select appropriate invariants. The constitutive model mainly describes the relationship between strain energy and various invariants. The total strain energy of the fabric is decoupled into the sum of various independent deformation strain energies such as tension, shearing and bending. These independent strain energies do not affect each other. The tensile strain energy in the fiber direction and the shear strain energy caused by the angle variation in the fabric plane are added to the hyperelastic constitutive model [132]. This is based on the mechanical behavior of fabrics during forming and is used to simulate the draping of textile composites. Charmetant et al. [139]established a hyperelastic model for analyzing the large deformation behavior of 2D fabrics and studied four deformation modes of fabrics. Subsequently, six deformation modes were proposed and added to the hyperelastic model for large-thickness 3D interlocking preforms [133]. Florian et al. [140] proposed a hyperelastic material model considering tension-compression-shear biaxial coupling, which was successfully applied to the simulation of woven fabric forming. Juan et al. [141] used a hyperelastic constitutive model to study the formability of a single-layer E-glass non-crimp 3D orthogonal woven reinforcement with complex shapes, and simulated the forming process of tetrahedral and double dome shapes. The effectiveness of the constitutive model was verified.

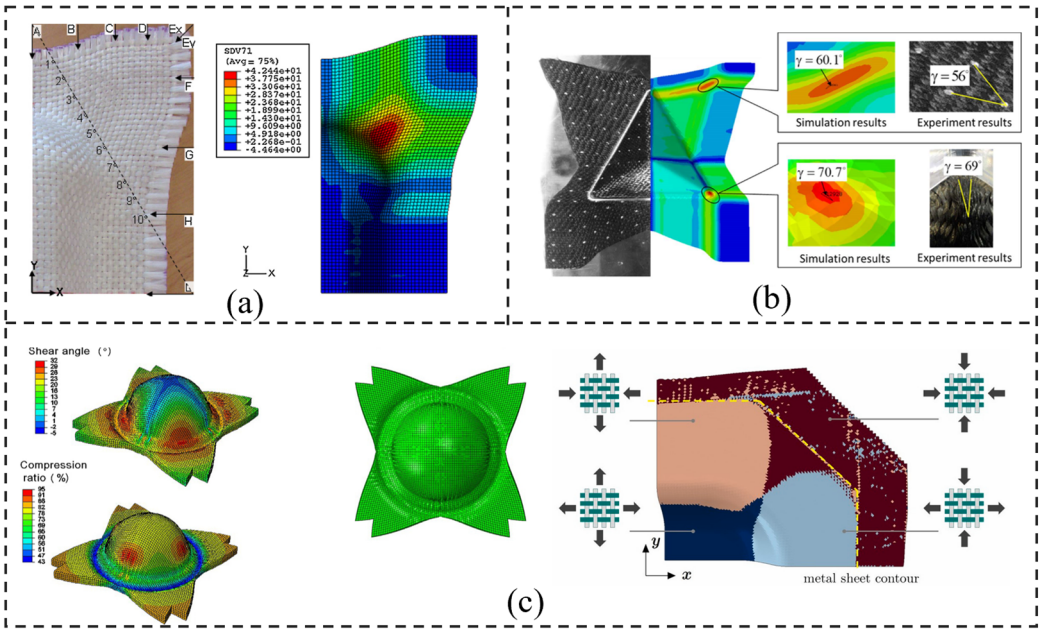

Fig. 1.24 Continuous approach, (a) the non-orthogonal constitutive model [40], (b) the hypoelastic model [137] and (c) the hyperelastic model [133,142].

1.6 Conclusion of Chapter I

The application of composite materials in components is changing from simple structures to complex structures, and the research is gradually changing from laminated composites to textile composites. This chapter responds to this trend with a great deal of research on the fabrication of composites with complex shapes. Firstly, the basic concept and application of textile composites are introduced, and then the reinforcements of textile composites are classified. On this basis, the preforming process of composites before resin injection is introduced, which is one of the key steps in manufacturing composites with complex shapes. During the preforming process, the mechanical behavior of the fabric can lead to different types of defects, such as wrinkles, buckling, etc. In order to reduce defects generation, the mechanical properties of the fabric are essential. Therefore, the fourth part of this chapter reviews the characterization test for the mechanical properties of fabrics, mainly including tensile, in-plane shear and bending properties for the deformation of single-layer fabrics during the preforming process. Considering the many factors that affect the quality of fabric forming, it is difficult to conduct research completely relying on experiments. Based on the mechanical properties testing of fabrics, the fifth part mainly introduced the simulation method of fabric forming. The simulation of textile reinforcements can be divided into microscopic, mesoscopic and macroscopic. Among them, the macroscopic scale method is acceptable to simulate the fabric forming process although some information is neglected in the simulation, and the method requires the lowest computational cost. Therefore, this chapter mainly analyzes the simulation methods of fabrics at the macroscopic level, which are mainly classified as discrete, semi-discrete and continuous. After the comparative analysis, the subsequent chapters in this thesis will use the continuous approach to study and simulate the mechanical properties of fabrics.

II. Mechanical behavior characteristics under tensile load during forming of braided fabrics

Résumé en français

Les composites tressés présentent de nombreux avantages intéressants, tels que la variabilité structurelle, des cycles de préparation courts et la possibilité d'être conçus selon diverses conditions d'application. Ces avantages jouent un rôle important dans la réduction du poids des composants aux formes complexes. Aujourd'hui, l'application des composites tressés devient de plus en plus large et est progressivement utilisé dans des industries telles que l'aérospatiale, l'automobile, la médecine et le sport.

Par rapport aux renforts tissées, les propriétés mécaniques des renforts tressés sont plus complexes et varient en fonction de l'angle de tressage. Les renforts tressés sont principalement divisés en renforts plats bidimensionnels et en renforts tubulaires tridimensionnels, comme illustré dans la Fig. 2.1. pour lesquels les propriétés mécaniques doivent être étudiées de manière séparée. Les caractéristiques de cisaillement dans le plan du préformage des tresses sont l'un des facteurs importants pour garantir la qualité des préformes avant l'imprégnation de la résine. L'étude des tresses plates a suscité de l'attention car due à leur structure asymétrique, elles présentent des comportements mécaniques différents dans les directions axiale et transversale. Ce chapitre étudie les propriétés mécaniques des préformes tressées en se basant sur des essais de traction. Tout d'abord, un modèle théorique est développé pour décrire le comportement de cisaillement dans le plan des tresses plates avec des angles de tressage arbitraires lors du biax-extension test, et la réponse en charge de la tresse est obtenue. L'angle de cisaillement lors des expériences est enregistré à l'aide de méthodes d'imagerie numérique et les résultats théoriques sont obtenus à partir de l'implémentation du modèle. Les résultats montrent que les renforts tressés présentent des caractéristiques de cisaillement différentes dans les directions transversale et axiale. De plus, l'étude du comportement mécanique des tresses plates fournira une loi théorique et des données pour l'approche de simulation par éléments finis abordée dans les chapitres III et IV.

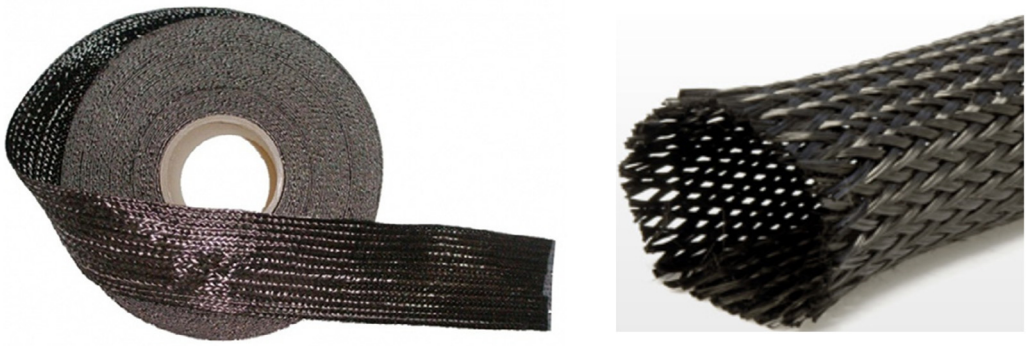

(a) (b)

Fig. 2.1 Renfort tressé, (a) avec une structure plate et (b) avec une structure tubulaire.

Mots-clés: Tresse plate; Tresses tubulaire; Cisaillement dans le plan; Propriétés mécaniques; Propriétés thermomécaniques

2.1 Introduction

The mechanical properties of braided fabrics largely affect the properties of composite parts with complex shapes. This chapter mainly focuses on the mechanical properties of two types of braided fabrics made of natural fibers, i.e., flat braided fabrics and tubular braided fabrics. Since flat braided fabrics have been extensively studied, this chapter just only introduces the theoretical models of flat braided fabrics and the results under bias-extension tests. The deformation analysis of tubular fabrics becomes the focus of this chapter. First, a mechanical model is established to describe the shear deformation characteristics of tubular braided fabrics, and then the mechanical response of tubular fabrics is studied under the uniaxial tensile tests. Considering that the mechanical properties of the fabric are affected by temperature during the forming process, this chapter also studies the thermomechanical properties of the tubular fabric. Through the analysis of theory and experiment, the mechanical properties of the preform are comprehensively grasped and provide a theoretical basis for the simulation analysis.

2.2 Bias-extension test for 2D non-orthogonal fabrics

2.2.1 Analytical model for shearing angle

To study the bias-extension test, two hypotheses are proposed: one to assume that the preform has no yarn slippage during the initial stage of loading, and that the yarns in the fabric are inextensible. Under this condition, there will be three shear areas in the fabric, as shown in Fig. 2.2. Area A represents the non-deformed zone ($\gamma = 0$), and no shearing took place in this zone. Area B represents the half-shear zone ($\gamma/2$), in two interlaced yarns, where one of the yarns was free at both ends. Free yarns undergo in-plane shearing during the tensile test. Area C represents the pure shear zone (γ), which appears in the middle part of the preform. The interlaced yarns were free at both ends. Therefore, in the process of the preform bearing the load, the interlaced yarns in this region underwent complete shearing.

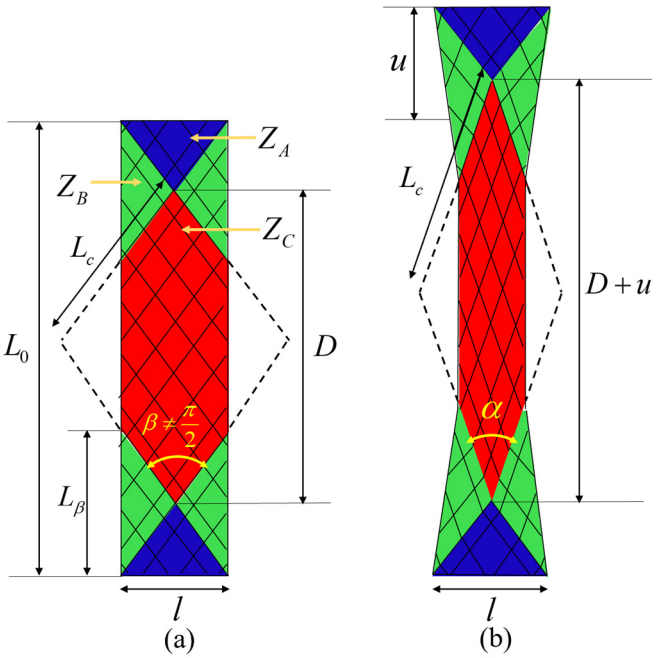

Fig. 2.2 The geometry of the fabric during a bias extension test, (a) initial state and (b) deformed state.

Fig. 2.2 (a) shows the undeformed stage of the fabric, the braiding angle $(\beta/2)$ was unchanged since the fabric had not yet been stretched. With the increase of the load, the two interlaced yarns in zone C started to rotate, and β gradually decreased to α, causing the shear angle γ to be generated. This shear angle can be expressed as:

$$\gamma=\beta-\alpha \tag{2.1}$$

In the pure shear zone, the value α can be determined according to the fabric geometry.

$$\cos\left(\frac{\alpha}{2}\right)=\frac{(D+u)}{2L_c} \tag{2.2}$$

Here, D and L_c are the diagonal length and theoretical side length of the rhombus of the pure shear zone (zone C) before deformation. The height of the triangle (L_β) in area A remained unchanged after the deformation and can be expressed as $L_\beta=l/\tan(\beta/2)$. The diagonal length of the pure shear zone D can thus be computed as:

$$D=L_0-L_\beta=L_0-\frac{l}{\tan(\frac{\beta}{2})} \tag{2.3}$$

The relationship between the braiding angle (β) and L_2 is:

$$L_c = \frac{D}{2\cos\left(\frac{\beta}{2}\right)} \tag{2.4}$$

According to Eq. 2.2 and Eq. 2.3:

$$L_c = \frac{1}{2\cos\left(\frac{\beta}{2}\right)}\left(L_0 - \frac{l}{\tan\left(\frac{\beta}{2}\right)}\right) \tag{2.5}$$

Therefore, the theoretical value of the shear angle is defined as:

$$\gamma = \beta - 2\arccos\left[\frac{u\sin\left(\frac{\beta}{2}\right)}{L_0 \cdot \tan\left(\frac{\beta}{2}\right) - l} + \cos\left(\frac{\beta}{2}\right)\right] \tag{2.6}$$

In the initial configuration, the fabric was not stretched and had no shearing behavior. The areas of zones A, B and C are expressed as:

$$Z_A = \frac{l \cdot L_\beta}{2} = \frac{l^2}{2 \cdot \tan\left(\frac{\beta}{2}\right)};\ Z_B = l \cdot L_\beta = \frac{l^2}{\tan\left(\frac{\beta}{2}\right)};\ Z_C = l \cdot \left(L_0 - \frac{3}{2}\frac{l}{\tan\left(\frac{\beta}{2}\right)}\right) \tag{2.7}$$

It is worth noting that the geometric relationship mentioned above is only correct when the aspect ratio of the fabric satisfies the following condition:

$$r = \frac{L_0}{l} \tag{2.8}$$

$$r \geq \frac{2}{\tan\left(\frac{\beta}{2}\right)} \tag{2.9}$$

2.2.2 Sample preparation

The proposed models were examined by using braided fabrics of flax/PA12 commingled yarns listed in Table 2.1. The biaxial braided fabrics were all produced by overbraiding on the braiding looms provided by the Gemtex laboratory [143,144]. It should be stated that it was necessary to carefully cut the fabric into a single layer of samples for the bias-extension test. A fair amount of attention was also required to master the braiding angle and avoid fiber slippage or local pull-out, as shown in Fig. 2.3.

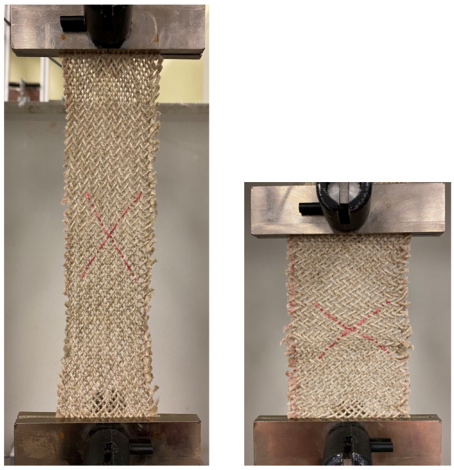

(a) (b)

Fig. 2.3 The fabrics for bias-extension tests, (a) axial test and (b) transversal test.

Table 2.1 The main physical properties of the tested braided fabrics.

Parameters	Flax/PA12
Type of braid	Biaxial twill 2-2
Yarn density (tex)	500
Braiding angle (β/2)	35°
Yarn thickness (mm)	1.03
Yarn width (mm)	1.15
Number of yarns per cm	4.2
Area density of the fabric (g/m^2)	376 ± 5

2.2.3 Experimental setup and the results

A series of bias-extension tests were performed on a rectangular sample to obtain the material parameters for the in-plane shear behavior. As mentioned in Section 2.2, to obtain a more complete mechanical behavior and validate the proposed theoretical model, two "Bias-extension" type tests were carried out in the axial and transversal directions to apply stress on the specimen in negative and positive shear, respectively [145].

The bias-extension test of non-orthogonal fabrics was conducted on a standard MTS system at a loading rate of 50 mm/min. The relevant parameters of the textile materials are listed in Table 2.1. It is worth noting that the braiding angle ($\beta/2$) of the fabric was 35°, and that the fabric structure was asymmetrical in the axial and transversal

directions. So, the angle of the interlaced yarn is 70° and 110° in the axial and transversal directions respectively. According to the requirements of Eq. 2.9, the parameters whose aspect ratio met the test requirements were obtained. The aspect ratios had to be greater than 2.9 in the axial direction and 1.4 in the transversal direction, and the specific parameters are shown in Table 2.2. Meanwhile, a camera was used to observe the deformation of the fabric in real time during the experiment. To reduce the error, each test is repeated five times to obtain average data.

Table 2.2 The main geometrical properties of the tested specimens.

Stretch direction	Sample yarns	L_0 (length) (mm)	l (width) (mm)	D (mm)	r (ratio) (L_0/l)
Axial Direction	Flax/PA12	200	50	128.59	4
		300	50	228.59	6
Transversal Direction		100	60	57.98	1.67

In order to ensure a sufficient pure shear space of the fabric, the geometric ratios of 4 in the axial direction and 1.67 in the transversal direction were selected for the test. According to the definition of in-plane shear angle, the axial direction along the sample is the positive direction. So, for the bias-extension test in the axial direction of the sample, the load and displacement are taken as positive values; for the test in the transversal direction of the sample, the load and displacement are taken as negative values. Fig. 2.4 shows the evolution of the experimental force obtained for these two tests as a function of the displacement, and the calculation of the shear angle determined from Eq. 2.6. However, only experimental data for a shear angle between -80° and 40° were used to characterize the material shearing. At this stage, there is enough shear space between the yarns. The yarns rotate with each other without being stretched, and the fabric undergoes pure shear deformation.

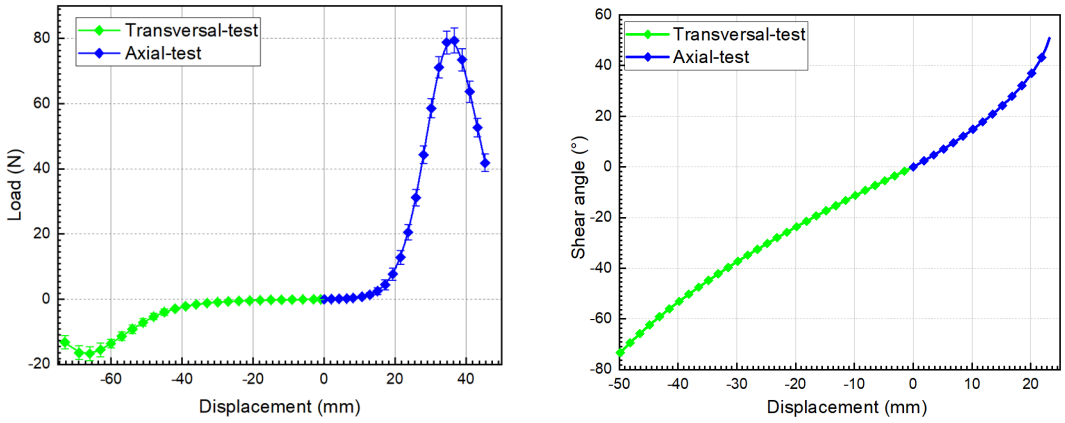

(a) (b)

Fig. 2.4 Results of flax/PA12 in different directions, (a) experimental load and (b) theoretical shear angle.

From Fig. 2.4, it can be seen that the relationship between load and displacement exhibits a nonlinear evolution, and the stretching process of the fabric goes through three stages. Firstly, as the displacement increases, the load increases slowly. The yarns have enough shear space, and the load is mainly used to overcome the friction between the yarns. With further displacement, the in-plane shear space of the intersecting yarns continuously decreases. When the interlaced yarns contact each other through the in-plane shearing process, the shear space no longer exists. At this point, the continuous in-plane shear behavior of the interlaced yarns will generate a transverse compressive force in the radial direction of the yarns, causing the load to increase rapidly and enter the second stage. Subsequently, as the stretching process continues, the intersecting yarns experience relative slippage, resulting in a decrease in load. The load-bearing capacity of the fabric is lost, and the in-plane shear behavior comes to an end.

2.3 Shear deformation characteristics of tubular fabrics under tensile loads

2.3.1 Materials and methods

The Flax/Polyamide 12 commingled yarns with a linear density of 500 tex and 1.78 mass ratio (64% flax yarns / 36% PA12 yarns) used in this study were provided by Schappe Technique. The tested tubular braided fabric is shown in Fig. 2.5 (b) and their main properties are listed in Table 2.3. The total number of yarns in the tubular fabric is 96. The braiding angle ($\beta/2$) shown in Fig. 2.5 (a) is defined as the angle between the

axial direction and the yarn.

Table 2.3 The main properties of the tested tubular braided fabric.

Parameters	
Type of fabric	Biaxial twill 2-2
Area density (g/m^2)	376 ± 5
Thickness (mm)	2.1
Diameter (mm)	50
Braiding angle ($\beta/2$)	55°
Number of yarns per cm	4.2

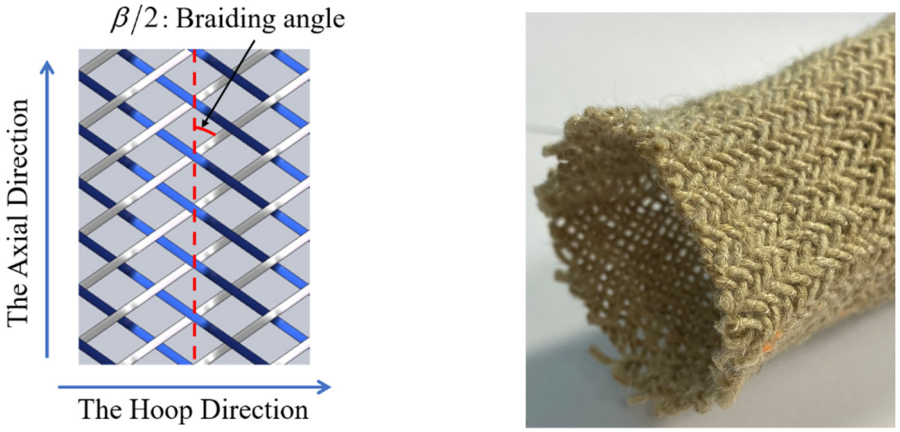

(a) (b)

Fig. 2.5 Tested tubular braided fabric.

The experimental setup for the tensile testing is shown in Fig. 2.6. Both ends of the specimen were fixed in the tensile machine by clamps, and a stretching force was applied at a uniform speed (10 mm/min) along the axial direction of the fabric. The length of the specimen was 40 mm excluding the gripped zones. It was essential to leave an appropriate length of fabric for clamping to ensure that no slippage occurred between the tows of the specimen and the clamps during the test [146]. To accurately analyze the mechanical response during the tensile testing of the tubular braided fabric, 3D scanning equipment with two cameras, shown in Fig. 2.6, was employed to monitor the test progression in real-time and record the changing state of the sample with the stretching. Consequently, the extension of the yarns and the change of the angle between them could be determined thanks to some markers related to the non-homogenous deformation shown in Fig. 2.7.

In order to reduce the experimental error when identifying the yarns' elongation, two intersecting yarns and pastes corresponding to markers at the intersection were chosen. The only criterion for selecting the markers was to ensure that they were positioned on the same single yarn. Considering the possible influence of yarn shearing, 5 marks were made on the fabric to obtain the length variation of two intersecting yarns and take the average value. For this, asymmetric markers were deemed to be more representative. The yarns' extension could be recorded during the test but not at the beginning, and in the course of the experiment the extension eventually led to damage to the sample's structure (Fig. 2.7 (d)).

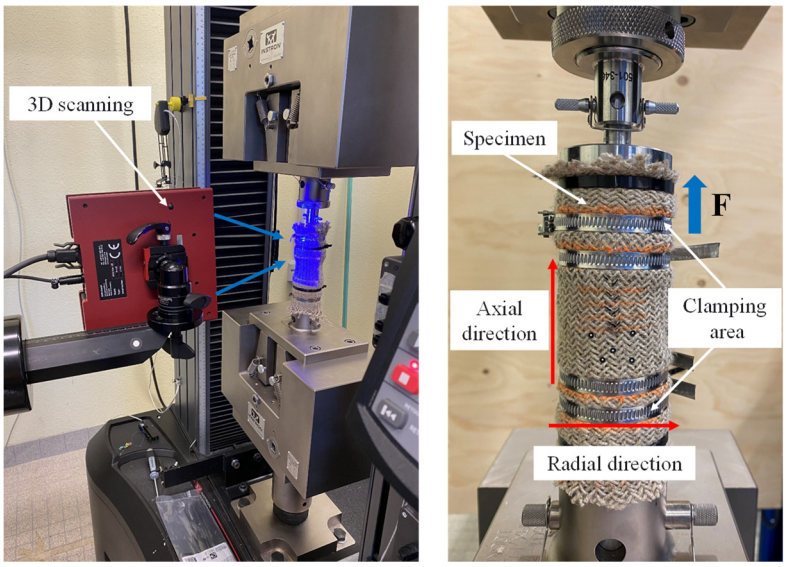

Fig. 2.6 Experimental device.

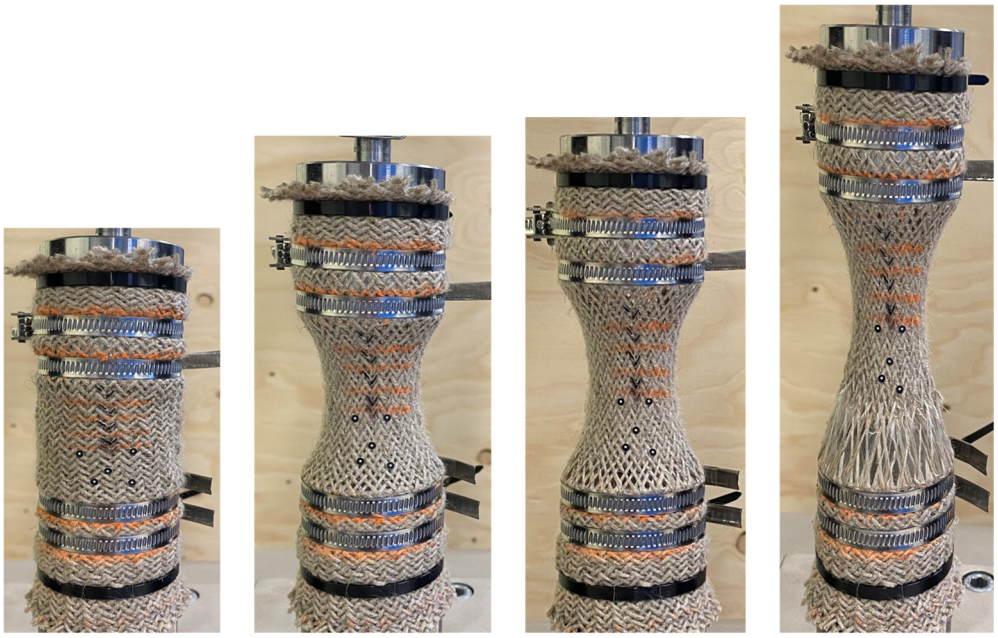

(a) (b) (c) (d)

Fig. 2.7 Tubular fabric specimen and markers, (a) initial state, (b) deformed state with 50% deformation, (c) deformed state with 75% deformation and (d) failure state.

After the tensile testing, the tubular fabrics eventually took on a radially contracted shape. At the beginning of the test, the intersecting yarns had enough rotational space to be accompanied by a pure shear behavior under the tensile load, and the radial contraction thus strongly depended on the variation of the shear angle. The study of radial shrinkage of tubular fabrics relies on their 3D structure and several methods can be used to remodel this: mathematical models and related algorithms to establish fabric simulation models [147], X-ray tomography to remodel the representative volume element [148–150], and 3D scanning to quickly reconstruct the model to experimental analysis. 3D scanning is an emerging technology that can convert objects into digital forms in spatial dimensions for rapid imaging [151]. Taking 3D images with a camera to capture the coordinates (x, y, z) of an object and regenerate the point clouds on the surface of the object has become a popular technique for characterizing textile deformation, and includes measurements of various strains during the textile reinforcements forming [73], reconstruction of wrinkling [143,144]; measurement of tow buckling [152], etc. In the present study, to vividly describe the profile shape of the deformed fabric during the test, Structure From Motion (SFM) was used complemented with the software CloudCompare to increase the quality of modelling [153].

SFM is an algorithm that reconstructs a real three-dimensional scene using two-

dimensional images from various angles in the collected space. SFM automatically extracts camera parameters from images, finds overlapping scenes in the input images, and performs feature extraction. When the feature points of the image are obtained, they are matched by calculating the Euclidean distance between the feature points of two images [154]. After finding the image pairs that match the required number of feature points, for each image, the matching pair is optimized and improved by the RANSAC algorithm [155]. The feature points are passed on in a chain in such matching pairs, and they are always detected to form a trajectory. At the same time, by estimating the internal and external parameter matrices, the coordinates of 3D points are obtained by triangulation.

Based on the reference points, i.e., the points in the non-moving parts, CloudCompare allows scaling of the model to obtain the real coordinates of the reconstructed point cloud in the 3D scene according to the actual geometric size. It also supports the output of coordinates for subsequent processing [156]. The original point-clouds exported by the SFM method include quite a significant amount of noise points. To increase the quality of the 3D reconstruction, post-processing was carried out in CloudCompare. The noise filtration was able to remove the isolated points from the raw point-clouds. The sizes of the processed point clouds generated via the SFM algorithm were relative and had to be calibrated to the real dimensions of the sample [153]. Errors were allowed in the calibration process. By modeling the known physical objects, the dimensions of the model obtained by the mentioned SFM and CloudCompare software were compared with the actual dimension and the modeling accuracy was found to be close to 99.32%.

Fig. 2.8 shows the evolution of this post-processing for a deformed tubular braided fabric in the axial tensile test. The new point-clouds in Fig. 2.8 (c) reproduced the essential features of the sample in Fig. 2.8 (a) after eliminating the isolated points (the noise) in the raw point clouds (Fig. 2.8 (b)).

(a) (b) (c)

Fig. 2.8 Example of three-dimensional reconstruction, (a) photo of the sample, (b) raw point cloud, (c) processed point cloud.

2.3.2 Mechanical responses in the tensile test

As presented in Fig. 2.7, tensile stretching of a tubular braided fabric leads principally to shearing deformation and extension of the yarns. The rotation of the yarns related to the shearing deformation on the plane of the unit cell is shown schematically in Fig. 2.9. This shearing deformation can be quantified by a shear angle. It is evident that the shear angle is not uniform in all of the unit cells, which is similar to what is seen for a flat braid [157] and to the bias-extension of a woven fabric [65,66,74] presenting different shear angle distributions, i.e., for which the shear angle is not unique. From the bias-extension test, it was found that the in-plane shearing was divided into three zones, i.e., the no-shear zone, the pure-shear zone and the semi-shear zone. The unit cells in the same zone had identical shear angles. Compared to the bias-extension test of flat fabrics, tensile testing of tubular fabrics led to the shear angles being identical only if the unit cells were on the circumference of the same height (i.e., had the same Z position), as shown in Fig. 2.9 (b). Therefore, the shearing deformation described by the shear angles is related to the tensile displacement in the axial direction. During a tensile test, the fabric is subjected to axial tension, and the intersecting yarns rotate and approach each other along the stretching direction [158–161], thereby causing a decrease in the angle between the yarns in the axial direction, resulting in a shearing behaviour.

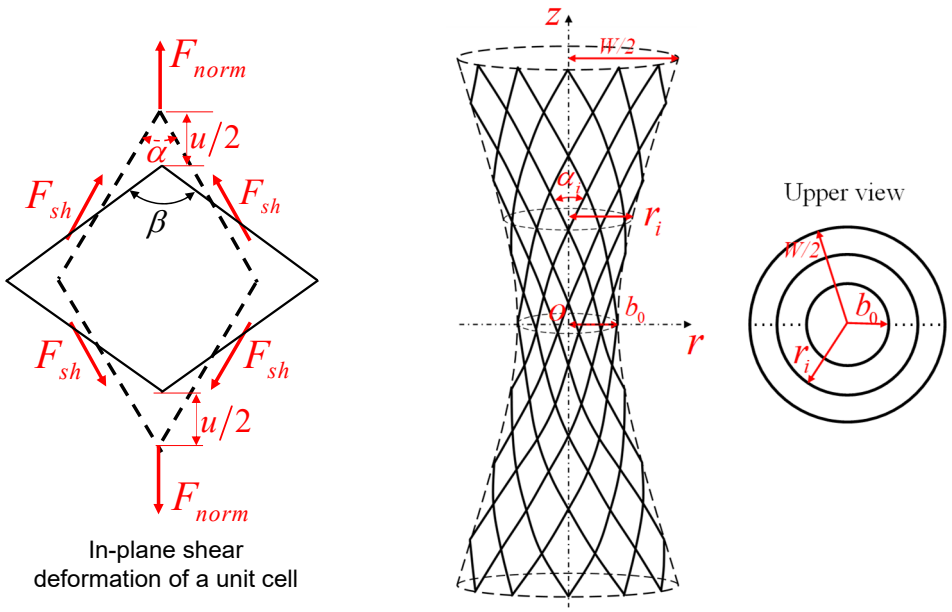

(a) (b)

Fig. 2.9 Schematic representation of the shearing deformation, (a) on the plane of a unit cell and (b) on the whole structure of the braided fabric.

The shearing deformation on the plane of the unit cell is shown schematically in Fig. 2.9 (a). The shearing angle is one of the essential parameters during the forming of textile fabrics. To describe how the shearing mechanism is coupled with the extension of the tubular fabrics and then optimize the pre-forming process of such a 3D structure, the analytical models need to be based on experiments to ascertain the relationship between tensile displacement and radial shrinkage, and subsequently determine the changes in shear angles and shear moments. Consequently, it is necessary to establish a kinematic and mechanical model to portray how the shear angle is connected to the tensile displacement [65,66,76,162] and also to describe the shear moment as a function of the shear angle [65,66,76,163].

(1) Prediction of the shear angle

Fig. 2.10 gives a schematic display of the whole tubular specimen and unit cell deformations under tensile stress. The tubular fabric undergoes radial contraction under tensile displacement [164,165] and the yarns become reoriented. In this case, the shear angles are generated distinctly on different zones corresponding to the Z position of the unit cell. The shear angles increase with the tensile displacement. To determine the shear angles, the axisymmetric fabric can first be projected on a plane as shown in Fig. 2.10, after which the radial contraction leads to the fabric taking on the shape of a

parabola as described in Eq. 2.10.

$$r=\sum_{i=0}^{N} b_i \cdot z^{2i} \tag{2.10}$$

Here, z and r are axial and radial coordinates, respectively, and N, b_i, i are constants. To simplify the calculation, N can be suggested as 1 which will be confirmed by experiments. Consequently, Eq. 2.10 can be expressed as:

$$r=\frac{2(W-2b_0)}{(u+L)^2}\cdot z^2+b_0 \tag{2.11}$$

Where u is the tensile displacement, b_0 presents the minimum radius of the deformed tubular fabric (the radius on the mean plane), and L and W symbolize the original length and diameter of the fabric, respectively.

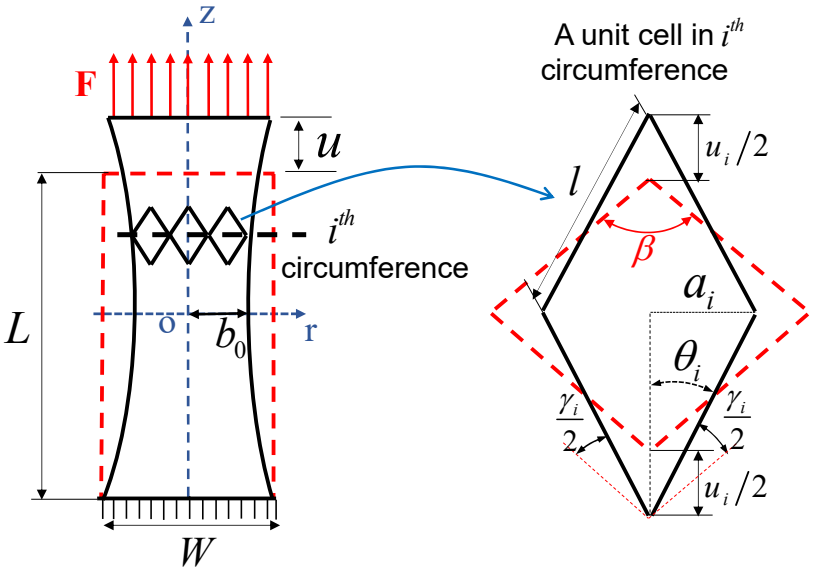

Fig. 2.10 The tubular braided fabric under a tensile load and a deformed unit cell in the i^{th} circumference.

Based on Eq. 2.11, the radial contraction at any position in the axial direction and the corresponding circumferential radius can be obtained since there is an assumption of no network slippage at the cross-over points of the yarns [65,146]. Therefore, the i^{th} unit cell can be represented as the research object (Fig. 2.10) to calculate the shear angle as shown in the following equations.

$$\gamma_i=\beta-2\theta_i \tag{2.12}$$

$$\sin\theta_i = \frac{a_i}{l} \tag{2.13}$$

In the i[th] unit cell, γ_i is the shear angle, a_i and l represent half of the diagonal length and the side length of the cell, respectively.

The radius of the circle in which the i[th] cell is located can be defined as r_i, and a_i can thus be expressed as:

$$a_i = \frac{\pi r_i}{n} \tag{2.14}$$

$$n = \frac{\pi \cdot W}{2 \cdot l \cdot \sin(\frac{\beta}{2})} \tag{2.15}$$

where n presents the number of the unit cells in a circumference. This number is a constant in the initial state and does not change in the deformed state.

The shear angle γ_i of the i[th] unit cell during the extension of the tubular braided fabric can be obtained by Eqs. 2.16-2.17.

$$\theta_i = Arc\sin\left[\left(\frac{4\cdot(W-2b_0)}{W(u+L)^2}\cdot z_i^{\,2} + \frac{2b_0}{W}\right)\cdot\sin\left(\frac{\beta}{2}\right)\right] \tag{2.16}$$

$$\gamma_i = \beta - 2\arcsin\left[\left(\frac{4\cdot(W-2b_0)}{W(u+L)^2}\cdot z_i^{\,2} + \frac{2b_0}{W}\right)\cdot\sin\left(\frac{\beta}{2}\right)\right] \tag{2.17}$$

Here, z_i is the Z coordinate of the center of the i[th] cell.

It is clear that the shear angle is identical in all unit cells on the same circumference (with the same Z positions). Therefore, the shear angle as a function of the tensile displacement can be given as:

$$\gamma = \beta - 2\arcsin\left[\left(\frac{4\cdot(W-2b_0)}{W(u+L)^2}\cdot z^{2} + \frac{2b_0}{W}\right)\cdot\sin\left(\frac{\beta}{2}\right)\right] \tag{2.18}$$

(2) Shear moment and shear load

As presented previously, the shear deformation is the domestic deformation mode during the tensile testing of a tubular braided fabric, and one can neglect the compaction on the lateral sides of the yarns and the extension of the fibres which normally occurs after the “locking shear angle”. Consequently, the power from the clamping load can be considered to dissipate mainly in the shearing zones. Regarding the non-homogenous shear deformation in the tubular structure, the prediction of the shear moment is focused on the unit cells that have the same Z. Considering a continuum

structure, the dissipation of energy during the tensile stress can be described by Eq. 2.19.

$$F(\gamma)\cdot\dot{u}=\int_{-(u+L)/2}^{(u+L)/2}2\pi\cdot r\cdot M_s(\gamma)\cdot\dot{\gamma}dz \tag{2.19}$$

where $M_s(\gamma)$ is the shear moment per unit area. $F(\gamma)$ is the clamping force. $\dot{u}$ is the rate of the quantity *u*. As a result, the shear moment $M_s(\gamma)$ is a function of the shear angle and depends on *z* in the axial direction as detailed in Eq. 2.20.

$$M_s(\gamma)=\frac{F(\gamma)}{2\pi\int_{-(u+L)/2}^{(u+L)/2}\left[\frac{2(W-2b_0)}{(u+L)^2}\cdot z^2+b_0\right]\cdot\frac{16(W-2b_0)\cdot\sin\left(\frac{\beta}{2}\right)\cdot z^2}{W(u+L)^3\sqrt{1-\left[\left(\frac{4\cdot(W-2b_0)}{W(u+L)^2}\cdot z^2+\frac{2b_0}{W}\right)\cdot\sin\left(\frac{\beta}{2}\right)\right]^2}}dz} \tag{2.20}$$

As the tangential load along the side of a fabric rhomboid element with unit cell dimensions (Fig. 2.9), the shear load has been described in [65], and depends on the shear moment of the fabric element (cf. Eq. 2.21). As a result, this load on a unit cell of the tubular braided fabric can be expressed by Eq. 2.22. On this basis, the numerical integration algorithm is employed to calculate the shear load during the tensile test. This is mainly achieved by employing MATLAB to call the integral function to implement.

$$M_s(\gamma)=F_{sh}\cdot\sin(\beta-\gamma) \tag{2.21}$$

$$F_{sh}(\gamma)=\frac{F(\gamma)}{2\pi\cdot\sin(\beta-\gamma)\cdot\int_{-(u+L)/2}^{(u+L)/2}\left[\frac{2(W-2b_0)}{(u+L)^2}\cdot z^2+b_0\right]\cdot\frac{16(W-2b_0)\cdot\sin\left(\frac{\beta}{2}\right)\cdot z^2}{W(u+L)^3\sqrt{1-\left[\left(\frac{4\cdot(W-2b_0)}{W(u+L)^2}\cdot z^2+\frac{2b_0}{W}\right)\cdot\sin\left(\frac{\beta}{2}\right)\right]^2}}dz} \tag{2.22}$$

2.3.3 Verification of the hypothesis

Several circles were marked on the tubular samples in their initial state to verify that no sliding took place between the yarns at the cross-over points. As shown in Fig. 2.7, the circles remained plane and perpendicular to the tubular axis throughout the test, which means that the circles were deformed only in the radial direction.

As described in section 2.3.2, the establishment of the theoretical shear model first considered the profile change during the stretching process of the fabric. Thanks to the Digital Image Correlation (DIC) method, the deformed profiles were reconstructed by using SFM and are shown in Fig. 2.11. During the acquisition of the images, the surface

of the samples was sufficiently and evenly illuminated without the appearance of reflections. To ensure accuracy, a full-range image stream including 72 images from all angles of the specimen was used to reconstruct the 3D point clouds.

It was found that the radial shrinkage of the fabric increased with the tensile displacement. The deformed tubular fabric maintained a symmetrical shape. Fig. 2.12 (a-c) present the comparisons between the measured lateral profiles and the ones obtained theoretically from Eq. 2.10 at a deformation of 25, 50 and 75 %, respectively. The good agreement found validated the hypothesis of the lateral profile and the expression of the theoretical profile curve provided by Eq. 2.10.

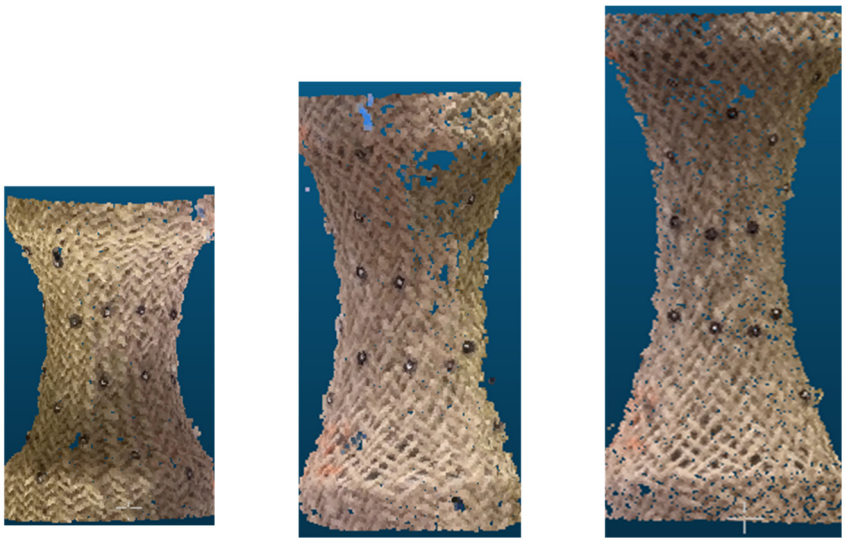

Fig. 2.11 The tubular fabric at 25, 50 and 75% deformation.

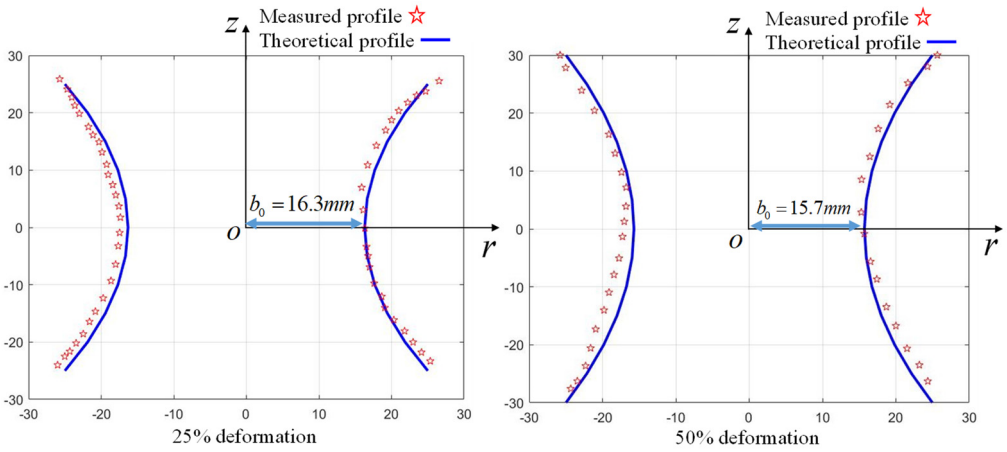

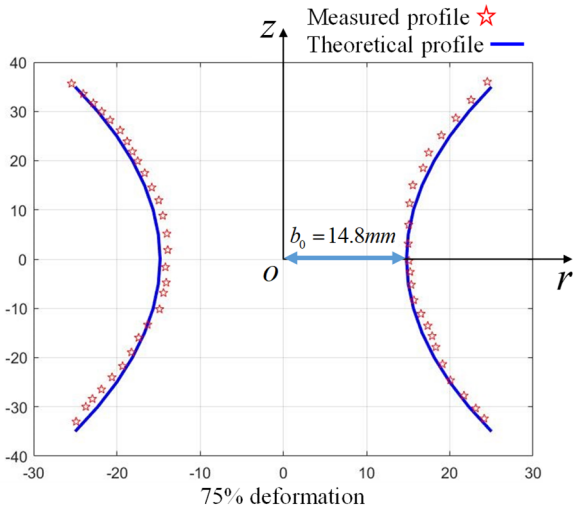

Fig. 2.12 Comparisons between measured and theoretical approaches about the lateral profile of the deformed tubular sample.

2.3.4 Tensile curves of the tubular braided fabrics

Fig. 2.13 presents the tensile load *vs.* the global deformation of tubular braided samples in axial extension tests. The curves can be divided into three parts before reaching the maximum load. In the 1st part, the load increased relatively slowly as a function of the tensile deformation. It was believed that this phenomenon concerned the pure in-plane shearing of each unit cell. At 60% deformation, the load started to rise rapidly due to the effects of extension and lateral compaction of the yarns. Between the 60 and 75% deformation, in-plane shearing was the dominating deformation mode: when strong contact appeared on the lateral sides of the yarns, the lateral compaction blocked the yarns' rotation. Consequently, the coupling of extension and lateral compaction of the yarns generated a rapid rise in the load. This significant increase started to fade at 125% deformation when the first damage to the yarns was observed near the clamps.

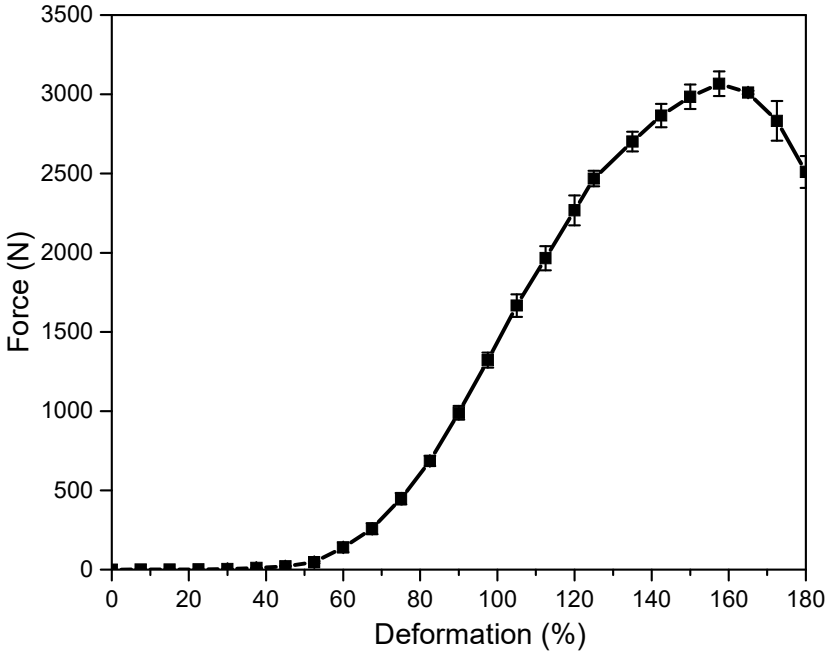

Fig. 2.13 Tensile load *vs.* global deformation for tubular braided samples.

Fig. 2.14 shows the shear angle and elongation of the yarn as a function of the fabric's global deformation. As can be seen, there was hardly any extension of the yarns before 75% deformation and the shear angle augmented rapidly in this pure shearing zone (Zone 1). Between 75 and 125% deformation, denoted "Zone 2" in Fig. 2.14, the shear angle increased slowly due to the impediment of the yarns' lateral compaction. In contrast, a significant extension of the yarns was noted. After 125% deformation (in Zone 3), the shear angle barely changed. From this moment, the deformed structure was completely locked and was denoted the "locking structure". Compared with plane textile fabrics, it was not appropriate to define it as a "locking angle", as a "locking angle" is not uniform in deformed tubular fabrics. In Fig. 2.14, the "locking angle" was close to 60° in the zone of 5 mm from the central line of the fabric (zone B in Fig. 2.15). The results displayed in Fig. 2.14 also explain the phenomena extracted from the tensile load / global deformation curve in Fig. 2.13.

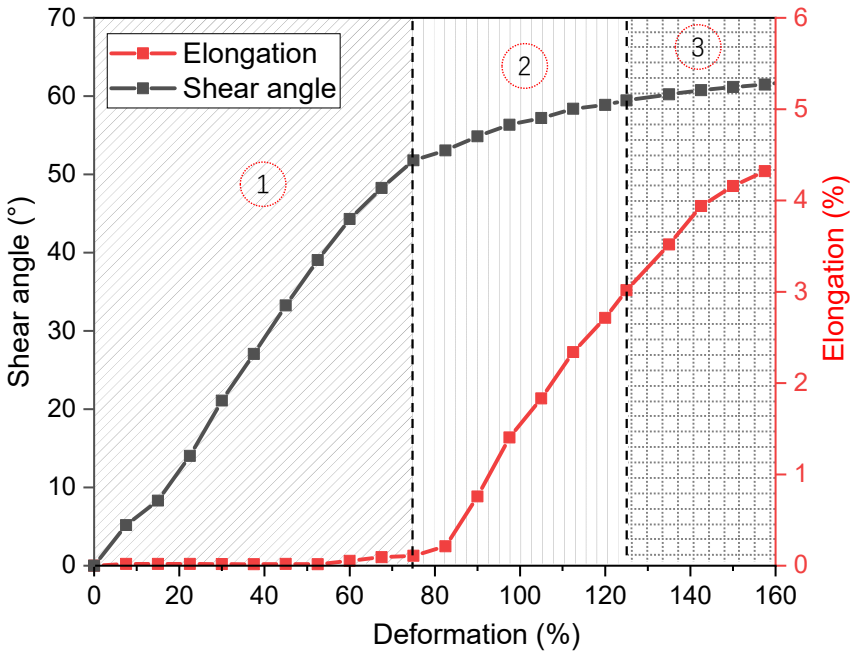

Fig. 2.14 Shear angle and elongation of the yarn *vs.* the fabric's global deformation during a tensile test (observed at 5 mm from the central line of the fabric).

2.3.5 In-plane shear response

As discussed previously, the axial tensile test of the tubular braided fabric generates a variation in the angle between the yarns. This angle can be defined as the in-plane shear angle on a unit cell and is not homogenous along the tubular sample. Fig. 2.15 shows four selected zones on the tested fabric in the axial direction according to the relevant dimensions. Due to the symmetry, it was possible to monitor the angles between the yarns only on the upper half of the sample.

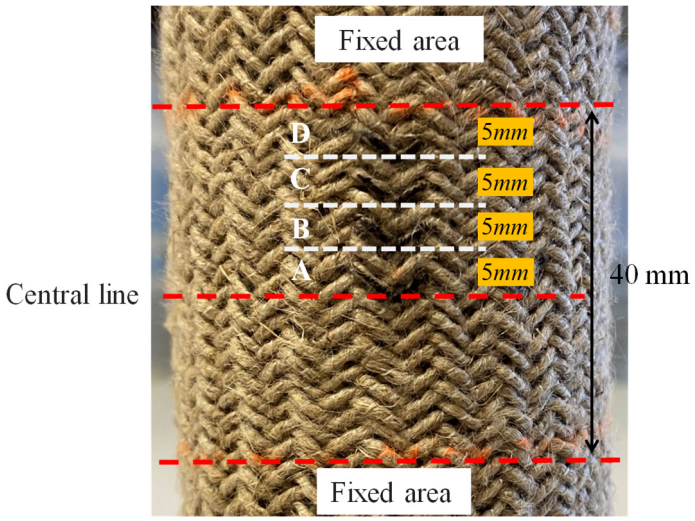

Fig. 2.15 Schematic representation of the shear region division.

Fig. 2.16 shows a comparison between the theoretical and experimental shear angles as functions of the global tensile deformation. The theoretical angles were calculated by using Eq. 2.17 and the experimental ones were obtained by DIC. The shear angles were found to be different in various distinct zones on the tubular sample. The central zone (zone A) consistently underwent the biggest shearing effect compared with the other zones. The zone closest to the clamps (zone D) had little rotation space, which led to it having the smallest shear angles. A good agreement (<10%) between theoretical and experimental approaches confirmed the developed analytical model, but this agreement lasted only up to 75% deformation or in the pure-shearing stage. From 75% global deformation, analytical and experimental results are increasingly divergent (30% difference at 120% deformation and 50% difference at 150% deformation). Moreover, at 75% global deformation, a notable shearing effect with a shear angle of almost 60° and radial shrinkage of 41% was observed in zone A. With the given braided fabric in the present study, 60° in-plane shearing deformation can be considered deep forming. In other words, it was possible to carry out deep forming while remaining in the pure-shearing stage of the tubular braided fabric in question.

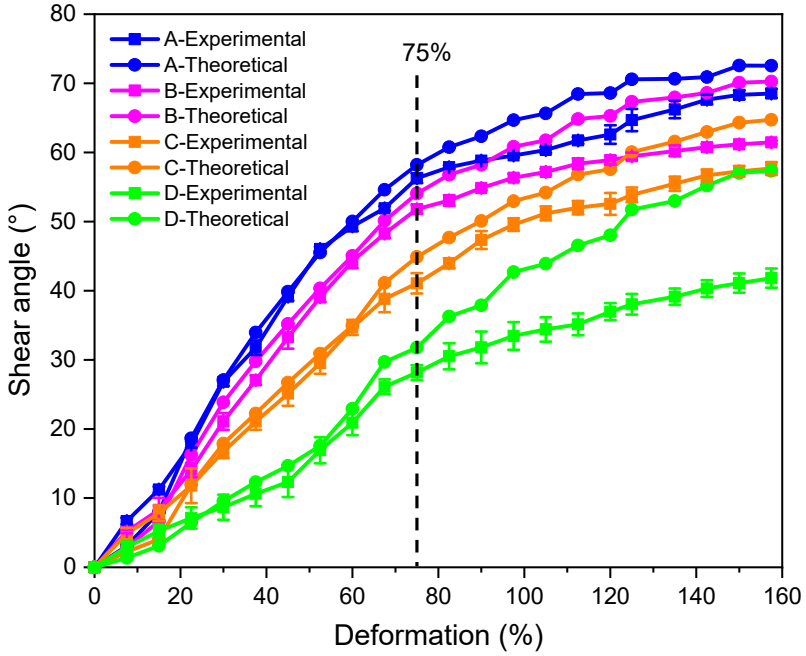

Fig. 2.16 Shear angle *vs.* global tensile deformation: comparison between theoretical and experimental results.

As presented in Fig. 2.16, the theoretical model provided a good prediction of the shear angle in the pure-shearing stage during the tensile testing of the tubular braided fabrics. Fig. 2.17 displays the shear loads as a function of the shear angles of the tubular braided samples under the axial tensile stress, with values obtained by Eq. 2.22. The four curves of shear load *vs.* shear angle corresponded to the four zones defined in Fig. 2.17. To obtain the same shearing deformation (i.e., the same shear angle), the different zones required different shear loads. There thus existed a local shearing behaviour or shearing deformation field on the tubular fabric. Compared with the zones close to the clamps, the central zones were deformed more easily under the shearing effects. It can be also observed that the "locking angle" was not uniform in the zones and depended on the position in the axial direction (the Z position). Furthermore, when going from zone A to zone D, the maximum shear angle that could be reached gradually decreased, indicating that zone A had a larger shearing space than the other areas in the pure-shearing stage.

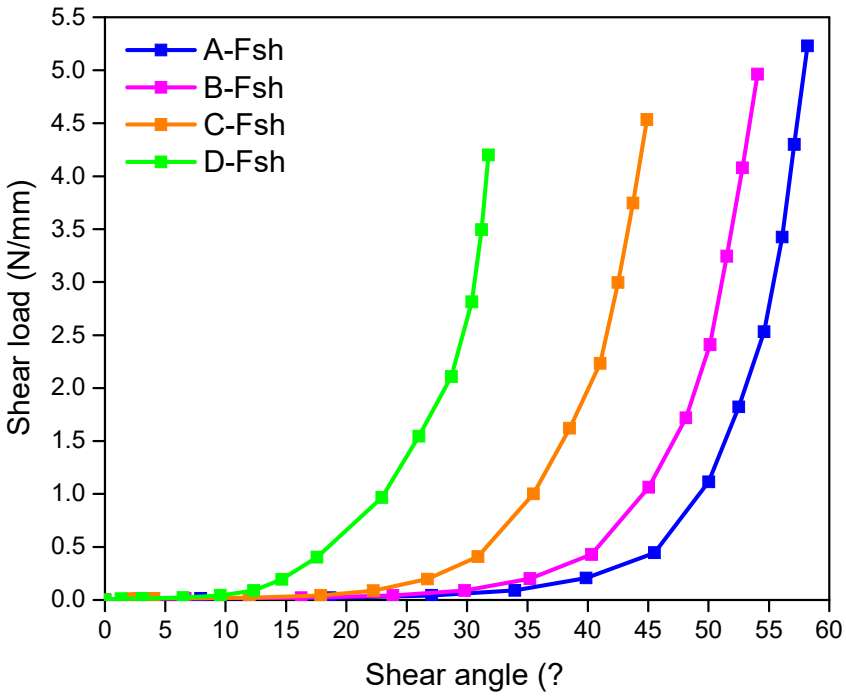

Fig. 2.17 Shear load *vs.* shear angle in the different zones of the tubular braided fabric.

2.4 Thermomechanical behavior of tubular fabrics under the tensile loads

2.4.1 Materials

The tubular braided reinforcements analyzed in the present study were manufactured from natural fibers commingled with Flax and Polyamide 12 (PA12) yarns (as shown in Fig. 2.18 (b)). The fabrics were produced by Gemtex laboratory. The total number of yarns in the tubular fabric is 96 and it was provided by Schappe Technique. The length of the specimen used for the test is 40 mm excluding the gripper zones and the diameter of the specimen is 50 mm. The main physical properties are noted in Table 2.4. As the important parameters of the samples, the braiding angle was determined by the braiding process. It can be noted that half of the angle between the tows is defined as the braiding angle (β/2) which is 55°, the structure is shown in Fig. 2.18 (a).

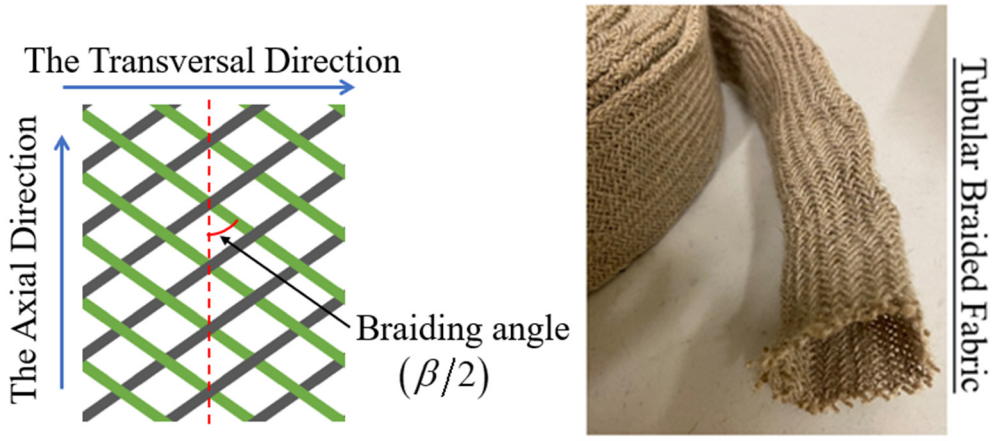

(a) (b)

Fig. 2.18 Tubular braided fabrics, (a) Structure diagram of 2-2 twill with braids and (b) Tested braids with Flax/PA12 commingled yarn.

Table 2.4 The main properties of the tubular braid fabrics.

Parameters	Flax/PA12 Specimen
Type of braid	Biaxial twill 2-2
Initial braid angle (β/2)	55°
Yarns density (tex)	500
Area density (g/m^2)	376 ± 5
Number of yarns per cm	4.2
Thickness (mm)	2.06
The mass fraction of flax	64%
The mass fraction of polyamide	36%

2.4.2 Tensile tests under hot temperatures

The uniaxial tensile tests are conducted by an Instron tensile machine with a load cell is 250 kN. According to the standard NF ISO 13934, the tensile speed was set to 10mm/min. To avoid the sliding of the sample during the stretching process, the ends of the fabric are connected to the stretching machine by the corresponding clamps. The mechanical behavior and the braiding angle of the samples during tensile tests were recorded thanks to a camera that was positioned in front of the machine. The software ImageJ is also used to analyze the pictures. Fig. 2.19 displays the experimental setup. The thermomechanical test of the fabric is mainly divided into two parts to analyze the effects of temperature and tensile speed on mechanical properties. Since the melting value of PA12 is 178 °C, the temperature range was chosen to include below and above

the melt temperature to analyze the thermomechanical properties of fabrics more comprehensively. The specific experimental conditions are shown in Table 2.5. All tests are performed in an isothermal oven and each test was started after the temperature has stabilized. To ensure the accuracy of the results, the tests are conducted more than three times.

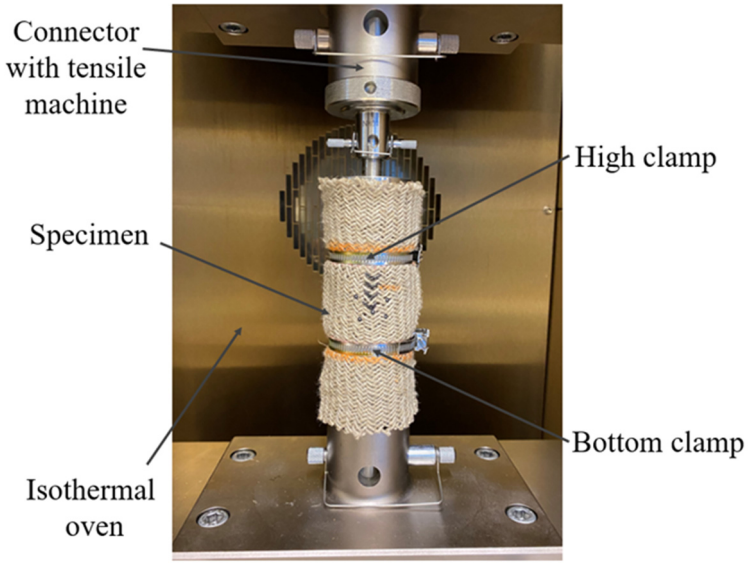

Fig. 2.19 Setup of the tensile machine with the specimen.

Table 2.5 The different main conditions of the tensile test.

Condition	Temperature(℃)	Velocity(mm/min)
Room temperature and displacement speed	20	10
Variants of temperature with same velocity	150 170 180 190	10
Variants of velocity with same temperature	190	5 10 20

Fig. 2.20 shows the tubular specimen before and after the tensile test. Fig. 2.20 (a) shows the initial state of the specimen. The deformed shape at 150 °C is shown in Fig. 2.20 (b). Fig. 2.20 (c) shows the deformation at 190 °C. The radial shrinkage structure

of the specimens is clearly shown in the deformed configuration. The melting state of PA12 can be observed at 190 °C and the specimen was impregnated.

The experimental results in Fig. 2.20 show that the shear behavior of tubular fabric under tensile load not only leads to radial shrinkage but also yarns' reorientation [159,161], which creates the shear angle. It's similar to the in-plane shear of the woven fabric [65,66,84]. During the bias-extension test, as the tensile displacement increases, the intersecting yarns rotate with each other and leading to a decrease in the angle between them. So, the fabric undergoes in-plane shear behavior and produces the shear angle. The in-plane shear behavior leads to three different zones, which are the 'no-shear zone', 'semi-shear zone' and 'pure shear zone' [76,162,166]. It is worth noting that the shear angles are equal within the same zone. But for tubular fabrics, the shear angle is the same only at the fabric's circumference of the same height. To analyze the mechanical behavior of tubular fabrics, it's crucial to grasp the variation law of shear angle. As the shear angle not only depends on the tensile displacement but also is affected by the temperature. Therefore, to analyze the shear behavior of fabrics during thermoforming, the effects of deformation and temperature need to be considered. In the existing studies, the analysis of shear angle is mostly based on analytical models which have proven to be effective for characterizing the mechanical behavior of fabrics at room temperature and have been used for simulation analysis. This section attempts to develop an analytical model to determine the shear angle on the smallest circumference of the tubular fabrics at room temperature.

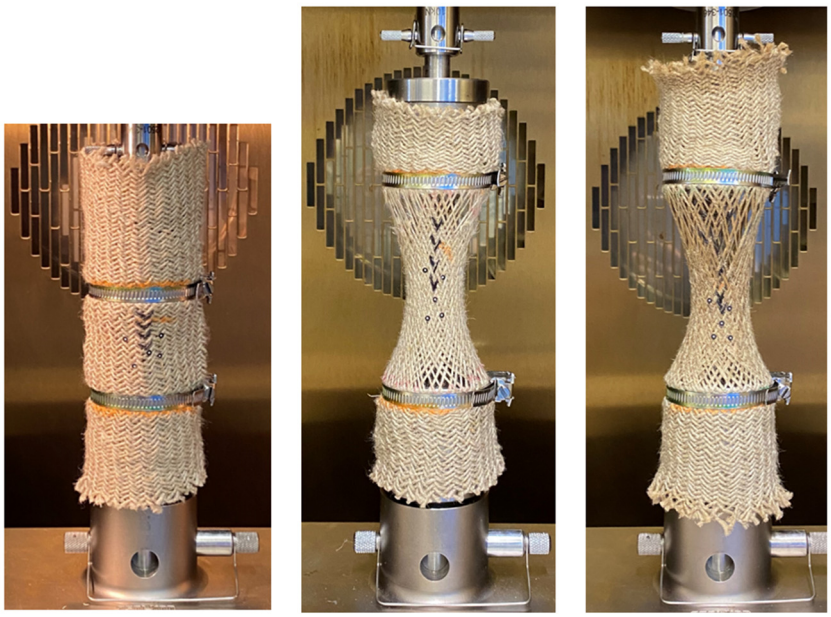

(a) (b) (c)

Fig. 2.20 Tensile tests performed on tubular braids in an isothermal oven, (a) initial state, (b) specimen with broken yarn at 150 °C and (c) specimen with broken yarn at 190 °C.

Compared to the state of the fabric after removing it from the tensile machine at 150 °C and 190 °C, the results are different (Fig. 2.21). It can be directly observed that after being stretched at the temperature of 190 °C, the fabric still maintained the radial shrinkage shape even if it has been removed from the tensile machine after being stretched at the temperature of 190 °C. It's probably due to the fact that 190 °C exceeds the melting point of PA12, the fabric is in a molten state and cannot return to its initial state after curing. On the contrary, the melting point of PA12 is not reached at 150 °C, the fabric has the behavior of returning to its original state when it is removed from the machine. This also confirms that temperature has an important influence on the forming of the fabric and should be set reasonably. In particular, the melting point of the yarn cannot be ignored during the thermoforming process.

(a) (b)

Fig. 2.21 Specimens removed from the testing machine, (a) specimen at 150 °C and (b) specimen at 190 °C.

In the forming process of the fabric, the influence of the shear angle cannot be ignored. On the one hand, the shear angle facilitates the draping of the fabric. On the other hand, the shear angle is closely related to wrinkling. The shear angle facilitates the draping of the fabric but is also closely related to wrinkling. When the shear angle exceeds the maximum critical value ("locking angle"), wrinkling is more likely to be produced. So, it is necessary to master the evolution of the shear angle. It is obvious from the experimental results that the distribution of the shear angle of the tubular fabric is not uniform. The shear angle is the largest in the middle part of the fabric and the smallest at both ends. Therefore, the shear angle in the minimum circumference of the fabric ("the maximum shear zone") is the first to reach the locking angle, which induces forming defects. In this section, an attempt is made to develop an analytical model to predict the shear angle in the maximum shear zone of tubular fabrics.

According to the experimental results, a deformation schematic diagram of tubular fabric is shown in Fig. 2.22, L and W in the figures symbolize the original length of the fabric and the diameter of the fabric, respectively. z represents the axial direction of the fabric. F is the tensile load. It is assumed that there is no slippage between two yarns and the yarns are not elongated during the test. As the tensile displacement increases, the relationship between the displacement and the minimum radius of the fabric can be

fitted:

$$b = 0.005587 \cdot u^2 - 0.5367 \cdot u + 25.06 \tag{2.23}$$

where u presents the tensile displacement and b presents the minimum radius of the fabric.

To study the shear angle of the fabric, a unit cell in the minimum circumference of the fabric is taken as the research object, as shown in Fig. 2.22. According to the definition of the shear angle and the corresponding geometric relationship, the shear angle on the minimum circumference of the fabric can be expressed as:

$$\gamma = \beta - \alpha \tag{2.24}$$

$$\gamma = \beta - 2\arcsin\left(\frac{2b\sin\left(\frac{\beta}{2}\right)}{W}\right) \tag{2.25}$$

where L symbolizes the original length of the fabric, z indicates the height of the fabric along any circumference in the axial direction. W represents the diameter of the fabric. β is the initial interlaced angle and γ is the shearing angle.

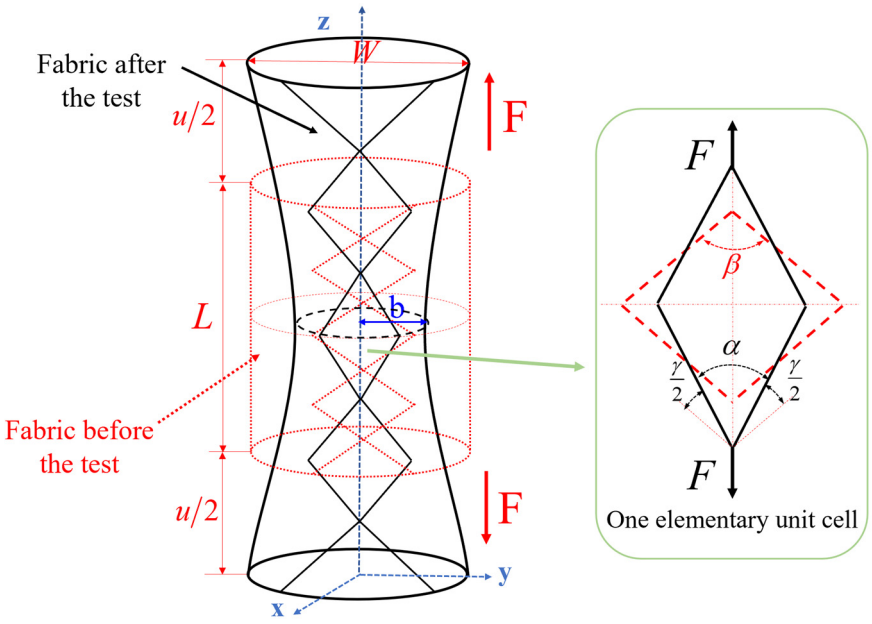

Fig. 2.22 Deformation of the tubular fabric before and after the test.

2.4.3 Results and discussion

(1) Comparison between the experimental and theoretical shear angle

The shear angle in the minimum circumference of the fabric during the test was measured optically to verify the theoretical model proposed in Section 2.4.2. The

theoretical value of the shear angle can be obtained by bringing the displacement into Eq. 2.25, the theoretical value of the shear angle at 150 °C can be obtained and compared with the experimental results, as shown in Fig. 2.23. The measurement results of the shear angle in the minimum circumference of the fabric follow the theoretical curve until the deformation reaches 60% to 70% (corresponding to a 50° shear angle). When the fabric deformation reaches about 35% to 40% (i.e. a 35° angle), the experimental value and the theoretical value begin to separate, but the theoretical value can still describe the experimental value well. The maximum error at this stage is 9.5%. This means that there is no (or limited) elongation of the yarn and no (or limited) slippage between the two yarns before the 40% deformation, which is consistent with the previous assumptions. In this stage of the test, it is reasonable to use theoretical values to reflect the shear angle. The crossed yarns are rotated relative to each other, and the shear angle increases. When the deformation exceeds 70%, there is a large separation between the experimental curve and the theoretical curve. The maximum error at this stage is more than 10.4%. At the same time, the growth rate of the measured shear angle slows down, while the theoretical shear angle continues to increase. This can be due to slippage between the two yarns or yarn elongation. However, theoretical models do not take these two factors into account and thus cannot continue to describe the shear behavior of fabrics.

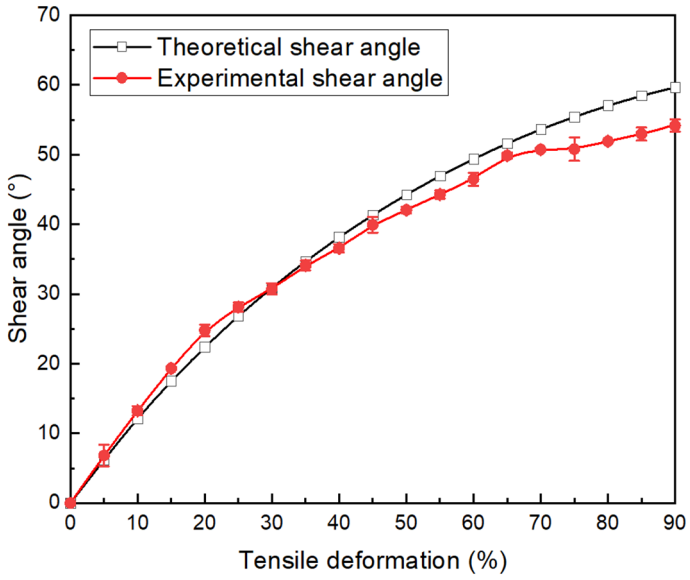

Fig. 2.23 Comparison of experimental and theoretical shear angle in the maximum shear zone of fabrics.

(2) Comparison of tensile behavior of flat braided fabric and tubular braided fabric

The mechanical behavior of flat braided fabrics depends on the bias-extension test. The details of the test with Flax/PA12 flat braided fabrics are given in the Chapter II and fabrics with an aspect ratio of 4.2 were selected to compare with tubular fabrics, the tensile schematic is shown in Fig. 2.24. Three distinct zones A, B and C are clearly indicated in Fig. 2.24 (a). There is no shearing deformation in zone A, half shearing deformation in zone B and pure shearing deformation in zone C. The sample is stretched to produce the pure in-plane shear angle in zone C and semi-angle in zone B. Compared with the stretching of flat fabrics, the deformation of tubular fabrics is more complicated. In the tensile test, the tubular fabric exhibits multiple different zones along its axial direction, and the shear angles of each zone are not equal. The distribution of the shear angle has a non-uniformity, the shear angle is largest near the middle part of the fabric and smallest near the ends. The shear angles are equal only if they are located on the same circumference of the fabric. At the same time, the maximum shear angle of flat fabric is in the pure shear zone, while the maximum shear angle of the tubular fabric is located on the minimum circumference of the fabric.

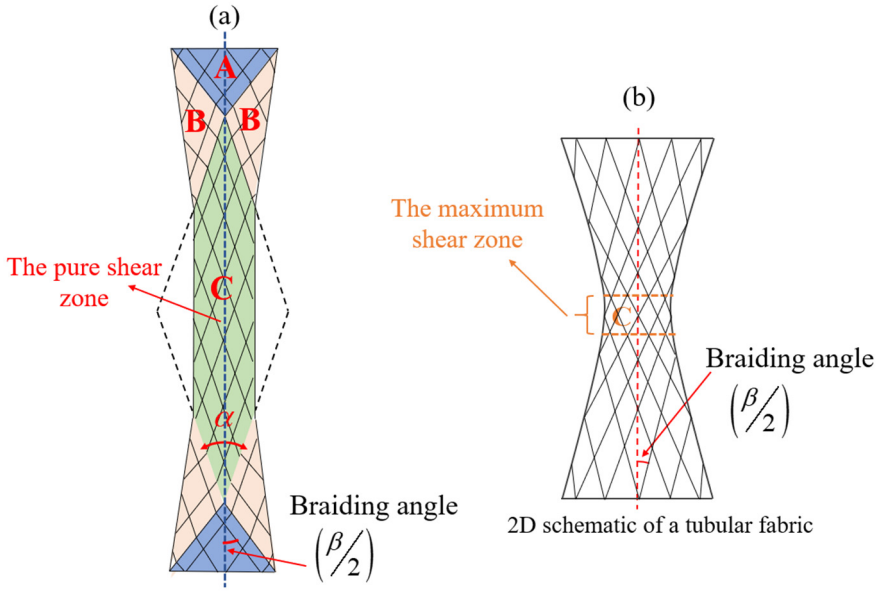

Fig. 2.24 Schematic diagram of deformation of flat braided fabric and tubular braided fabric.

The braiding angle, as one of the most important parameters of the braided preform, has a great influence on the mechanical properties of the braided composite materials.

The mechanical properties of braided preforms vary with the braiding angle. Therefore, the shear angle in the maximum shear zone of flat braided fabric in the literature and tubular braided fabric in the present paper is compared during the stretching process, as shown in Fig. 2.25. The maximum shear angle of two fabrics increases first and then tends to be constant with the increase of tensile displacement. Under the same tensile displacement, the shear angle of the tubular fabric changes faster than that of the flat fabric. This is mainly because the middle zone of the tubular fabric has a larger shear space.

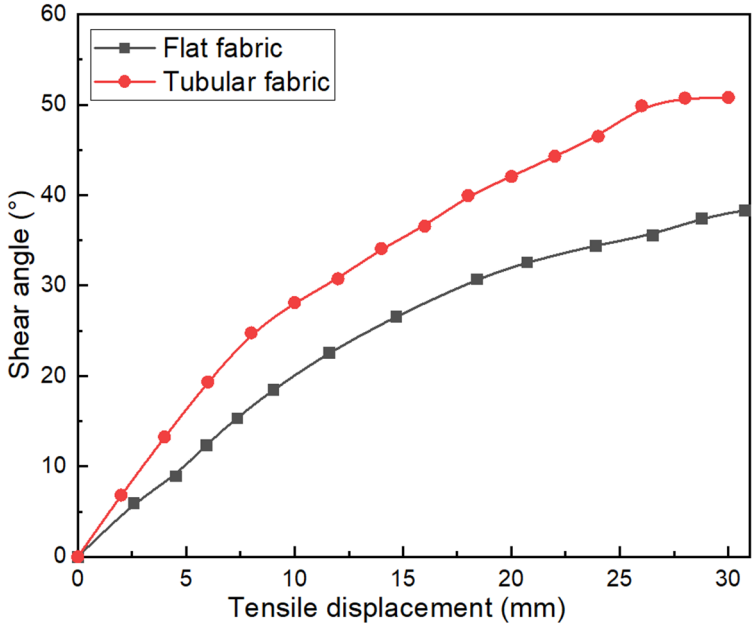

Fig. 2.25 Comparison of the shear angle for flat braided fabric in the pure shear zone and tubular braided fabric in the maximum shear zone.

2.4.4 Characterizations of tubular braided fabrics with Flax/PA12 Yarn

The load-displacement curves of the tubular fabric at different temperatures are shown in Fig. 2.26. The tensile curves of the fabric at different temperatures can be divided into three stages. In the first stage, the load increases relatively slowly with the increase of deformation. The load at this stage is necessary to overcome the adhesive friction between the yarns so that the yarns rotate with each other and start shearing until a deformation of about 35%~40%, which is consistent with the separation of the theoretical and experimental values of the shear angle mentioned in Fig. 2.23. Similar to the bias-extension test, the fabric at this stage exhibits pure shear behavior. Then, the

yarns contact each other and generate transversal compaction resulting in a rapid increase in load with the deformation increases. It is further explained that the growth rate of the in-plane shear angle slows down after the theoretical and experimental curves separate clearly. Finally, the load decreases due to the breakage of the fabric.

Although all of the curves in Fig. 2.26 present a similar non-linear evolution, the maximum load decreases with increasing temperature. The maximum load on the specimen at room temperature (T=20°C) is much larger than that at higher temperatures. In addition, the maximum deformation of the fabric also decreases with the temperature increases, and the fabric at 20 °C has a greater tensile deformation compared to 190 °C, which is strongly related to the melting point of PA12. The literature [167] gives the tensile results of single Flax/PA12 yarns at different temperatures, as shown in Fig. 2.27.

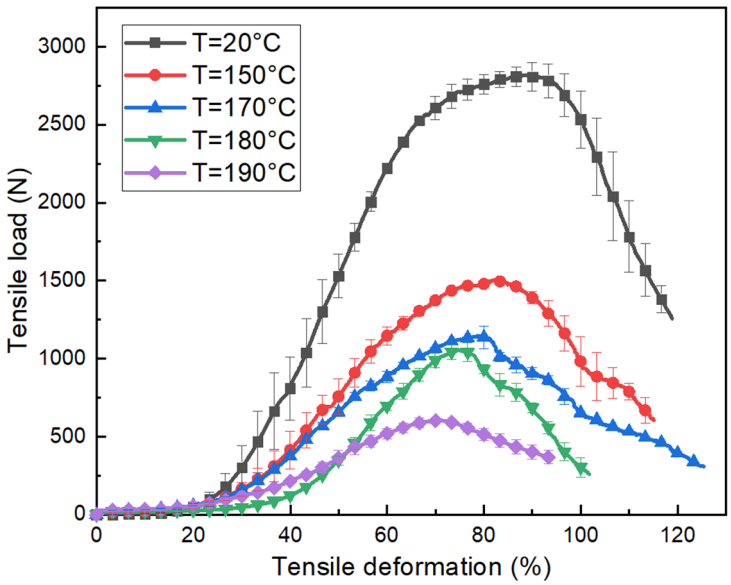

Fig. 2.26 The tensile load vs. tensile deformation of tubular fabrics under variation of temperature.

The tensile behavior of a single yarn at room temperature is analyzed, specifically showing a large deformation as a relatively large force, which can be divided into three stages: rapid increase (<3%), slow increase (3%-35%), and rapid decrease (>35%). The yarn in the first phase presents a shorter deformation corresponding to a large increase in tensile load. When the deformation reaches only about 3%, the slope of the curve changes, and the pure flax was broken, it has been proved by literature [168]. After the breakage of pure flax, PA12 was slightly deformed without breaking and it would still bear the load. The yarn retained a certain strength at this stage, the tensile process

continues to the next phase. In the second stage, the larger deformation of yarn could be observed but the slope of the increasing load is slower. At this phase, pure flax was broken, PA12 exhibited tensile behavior and the yarn presents a progressive deformation until PA12 was broken. The curve enters the third stage after a second slope change. In the third stage, the load decreases sharply, indicating an increased progression of a slip of fracture in flax and PA12.

From the above discussion, in Fig. 2.27, the tensile process of a single yarn at room temperature can be summarized as: (1) pure flax breakage; (2) PA12 breakage; (3) slippage of flax and PA12. Comparing the tensile behavior of the yarn at other temperatures, it was found that as the temperature increased, the tensile behavior of the yarn gradually changed from the initial 3 parts to 2 parts, and the maximum deformation also decreased from the initial 35% to 3 %. When the temperature was lower than the melting temperature (178 °C) of PA12, the tensile curves still included the three stages. While the deformation in the second stage decreased significantly as the temperature increased. This is because temperatures affect the strength of PA12, causing the force required to break and cause breakage in PA12 to decrease as the temperature approaches its melting value. Therefore, compared with room temperature, the deformation before PA12 reached fracture also decreased with increasing temperature. On the contrary, when the temperature was higher than the melting point of PA12, PA12 melted and the tensile behavior of the yarn was mainly characterized by pure flax and the curve consisted of only two stages. The maximum load drops sharply. This is also the reason why the maximum load and maximum deformation of tubular fabric as shown in Fig. 2.26 decrease with the increase in temperature during the stretching process. So, the thermomechanical behavior of the fabric depends largely on the temperature.

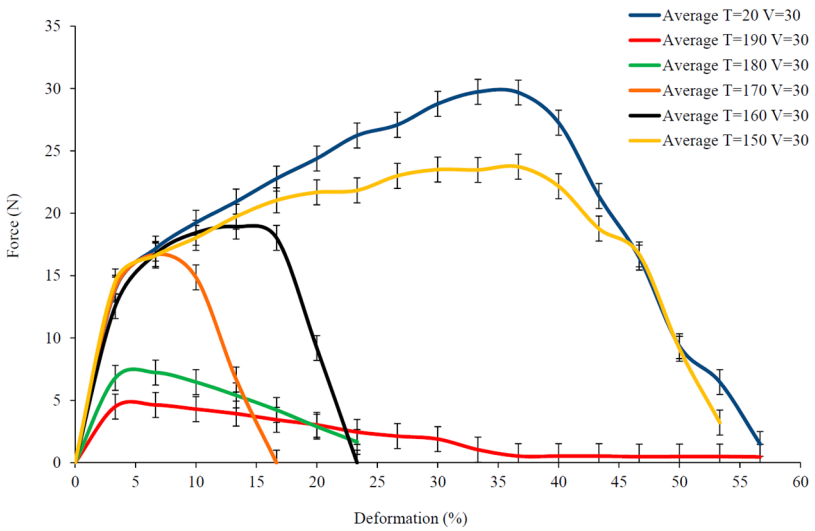

Fig. 2.27 The tensile load vs. tensile deformation of single flax/PA12 yarn under variation of temperature [167].

The shear angle is an important parameter to reflect the mechanical properties of the specimen. The relationship between the shear angle and the load at different temperatures is shown in Fig. 2.28. It can be found that at different temperatures, the shear angle and load present a non-linear evolution. Following the load augmentation, the shear angle increases. The increase in load can be divided into two stages. At first, the shear angle increases with a smaller load, then the shear angle becomes larger and the load also increases noticeably. It's due to the pure shear behavior of fabric at the initial stage of the tensile test and the transverse compaction of the yarns after "the locking angle". Similarly, the specimen at room temperature leads to load on the specimen that is much larger than for higher temperatures. This indicates that the shear stiffness of the fabric decreases with increasing temperature. When the state of the fabric tends to be stable, as the test temperature increases, the shear angle increases under the same load conditions. This is also caused by the melt state.

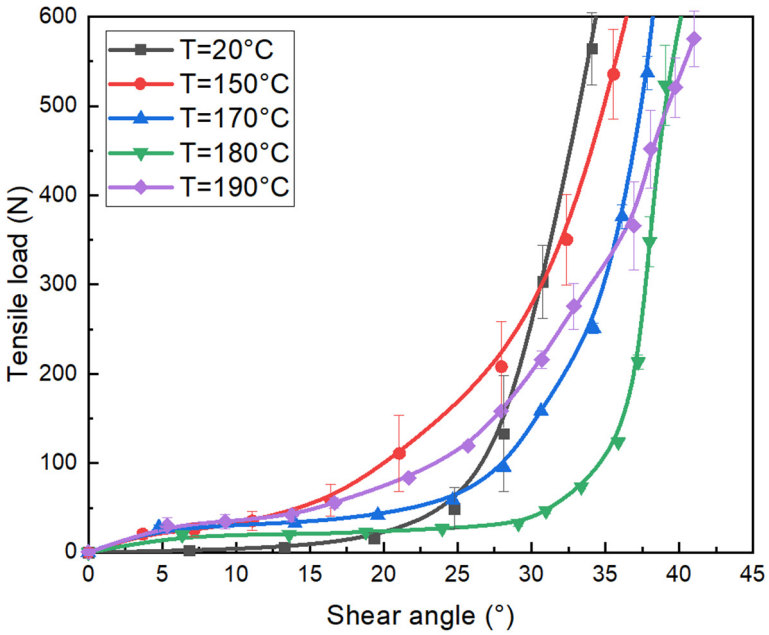

Fig. 2.28 The tensile load vs. shear angle under the different temperatures of tubular fabrics.

The load versus deformation curves are plotted in Fig. 2.29 corresponding to three different displacement rates. The temperature is maintained at 190°C. Firstly, the thermomechanical properties of the fabric show similar evolution for the different tensile speeds, which are also divided into three phases. Secondly, it can be found that the maximum load of the fabric at a speed of 20 mm/min increases noticeably compared with the maximum load at a speed of 10 mm/min and 5 mm/min. This indicates that the displacement rate has a certain influence on the properties of tensile behavior. The shear stiffness improved by increasing the tensile speed. Under faster speed conditions, PA12 doesn't melt enough and the fabric maintains a high level of tensile resistance to stretching.

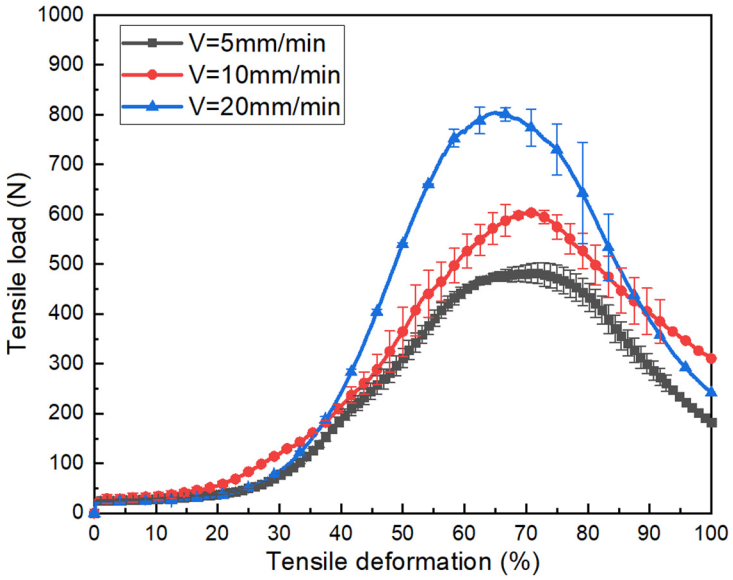

Fig. 2.29 The tensile load vs. tensile deformation curves under the different tensile speeds of tubular fabrics at 190 °C.

The shear angle characteristics corresponding to different tensile speeds of the fabric at 190 °C are shown in Fig. 2.30. It can be observed that fabric requires bigger effort at 20 mm/min than at 10 mm /min and 5 mm/min to achieve the same shear angle. Thus, this also proves that the strength of the fabric is influenced by the variation of the tensile speed. The strength of the fabric can be kept high by properly increasing the tensile speed.

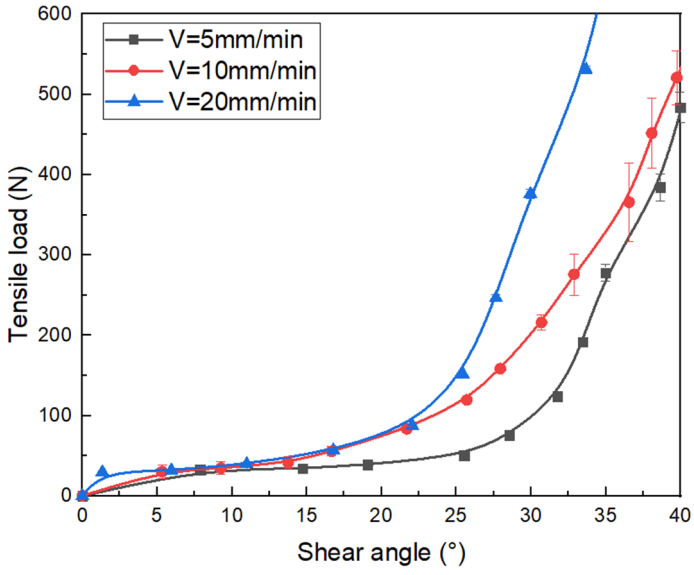

Fig. 2.30 The tensile load vs. shear angle under variation of speed for tubular fabrics at 190 °C.

2.5 Conclusion of chapter II

The forming of textile reinforcements is a complex process in which serval deformation modes are coupled. In this chapter, the shear properties of 2D braided fabrics are firstly analyzed by bias-extension test. Then, the mechanical response of tubular braided fabrics with hollow structures under an axial tensile load was investigated. This complex mechanical response was divided into three main parts from the tensile load/deformation curve. Pure shearing was the first part and generated the non-homogenous in-plane shear angles on the deformed tubular structure. A combination of in-plane shearing and yarn extension was observed in the second part until the lateral compaction of yarns completely blocked their rotation, and this phenomenon was called a “locking structure”. In the last part, after the “locking structure”, yarn extension became the dominant deformation mode, which finally led to structural damage. When it comes to the forming deformation, it was believed to take place within the first part, i.e., in the pure-shearing zone. For this, an analytical model was developed to describe the in-plane shear behaviour under axial tensile stress. The corresponding availability is verified by comparing experimental results produced by tubular fabrics.

Considering the effect of temperature on the fabric forming process, this chapter characterizes the thermomechanical properties of tubular fabrics at different forming temperatures and stretching speeds. Compared with the curves at different temperatures, the fabric at room temperature has the highest shear stiffness. As the temperature increases, the state of the yarn gradually transforms from a solid state at room temperature to a liquid state above the melt temperature. The effect of lubrication reduces the friction between the yarns, so the shear stiffness is reduced and the maximum load gradually decreases. The effect of tensile speed on the mechanical properties of the fabric is specifically shown by the fact that the strength of the fabric increases as the tensile speed increases. In the case of increasing the tensile speed, the fabric requires a bigger effort to achieve the same shear angle and the shear stiffness increases.

III. Numerical forming analysis of biaxial braided composite reinforcements

Résumé en français

Pour fabriquer des pièces composites à double courbure et de formes complexes, un renfort sec peut être utilisé dans les procédés LCM (Liquid Composite Molding), comme mentionné dans le chapitre I. Cependant, il s'agit d'une étape physique compliquée comprenant des comportements de déformabilité complexes. En raison des caractéristiques du renfort et des paramètres de fabrication, l'étape de préformage du renfort est également accompagnée de divers défauts. D'autre part, lorsque le tissu est drapé hors de la forme complexe attendue sur un moule à double courbure, cela entraîne une redistribution et une redirection des fibres, affectant ainsi les propriétés mécaniques du composant. En raison de la complexité du processus de préformage du tissu, il est difficile de se fier uniquement à des "essais", et seul une approche de simulations numériques peut permettre la prédiction la mise en forme du renfort et le réglage et l'optimisation des paramètres de fabrication.

La simulation numérique nécessite d'abord la sélection d'un modèle constitutif approprié pour décrire la loi de comportement du matériau. Ensuite, les paramètres requis pour la simulation sont déterminés en fonction des expériences. Lors de la mise en forme, ce modèle doit refléter avec précision les propriétés mécaniques des renforts et prédire le comportement anisotrope des composites finaux en raison de la réorientation et de la redistribution complexes des fils. Étant donné que la déformation du renfort pendant le préformage se manifeste au niveau macroscopique, selon le contexte théorique du chapitre I, le modèle de simulation numérique continu peut être choisi pour analyser et prédire efficacement le comportement mécanique des renforts pendant leur mise en forme d'un point de vue macroscopique. Le modèle continu comprend le modèle constitutif orthogonal et le modèle constitutif non-orthogonal. Les résultats de simulation du modèle non-orthogonal se rapprochent plus des expériences que ceux du modèle orthogonal. Actuellement, les modèles constitutifs non orthogonaux ont été utilisés pour l'analyse des déformablités pendant le procéde de mise en forme des renforts tissés, des NCF (Non-crimp fabrics) et des tissus 3D interlock.

Parmi les modèles continus, le modèle hyperélastique a été largement étudié et appliqué pour simuler le comportement mécanique macroscopique des tissus. Le modèle hyperélastique est basé sur la théorie de la mécanique des milieux continus et ses relations constitutives sont représentées par l'énergie de déformation et l'invariance plutôt que par une matrice de rigidité. Ce modèle constitutif prend en compte les

différents modes de déformation qui apparaissent dans le tissu pendant le procédé de mise en forme, tels que l'extension, le cisaillement dans le plan et la flexion, comme illustré dans la Fig. 3.1. Le modèle hyperélastique est un modèle élastique non linéaire typique pour les différents modes de déformation qui se produisent dans la mise en forme des renforts textiles, en supposant que les différents modes de déformation ne sont pas couplés les uns par rapport aux autres et que l'énergie totale de déformation du renfort est égale à la somme des énergies de déformation correspondant dans les différents modes de déformation indépendants. L'énergie de déformation est exprimée sous forme de fonction polynomiale des invariants en utilisant des invariants appropriés, et leur identification est réalisé par des tests mecaniques tels que le test de traction uniaxiale/biaxiale, le test de picture-frame test ou le bias-extension test.

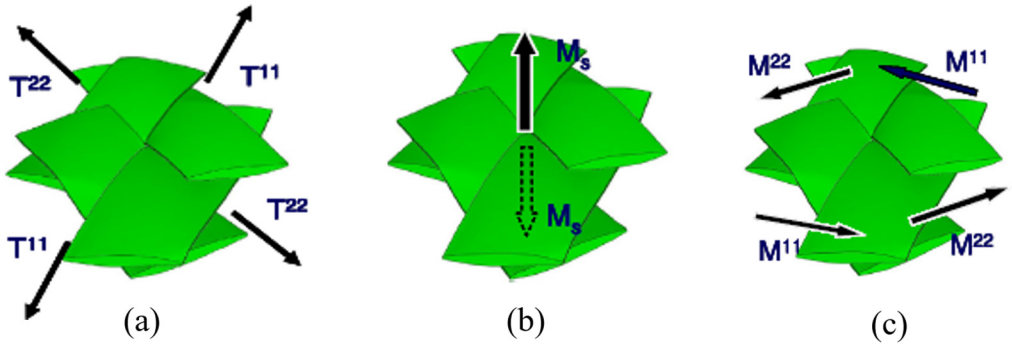

Fig. 3.1 Modes de deformation modes, (a) extension, (b) cisaillment dans le plan et (c) flexion.

Cependant, un grand nombre d'études de simulation sont limitées au cas des tissus où les directions de trame et de chaîne sont perpendiculaires les unes par rapport aux autres, et très peu d'investigations ont été consacrées aux tresses non orthogonales. Ce chapitre propose un modèle constitutif hyperélastique pour caractériser les propriétés mécaniques anisotropes des renforts tressés non orthogonaux afin de simuler le procédé de préformage. En se basant sur les modes de déformation, l'énergie de déformation a été définie par des invariants spécifiques correspondants. Les coefficients de la loi constitutive hyperélastique ont été identifiés dans le cas des renforts non orthogonaux grâce à l'établissement d'un modèle énergétique entre le tenseur de contrainte de Kirchhoff et l'effort de traction. La loi constitutive et le modèle énergétique ont ensuite été validés par comparaison avec le bias-extension test et le test d'emboutissage

hémisphérique.

Mots-clés: Textile composites; Renfort tressés; Simulation numérique; Modèle hyperélastique; Mise en forme

3.1 Introduction

The forming process of the preforms is crucial for the final properties of complex-shaped composites, and the deformation behavior of the fabrics is determined by the mechanical properties discussed in Chapter II. Based on the bias-extension test of flat fabrics, the objective of this chapter was thus to first improve a non-orthognal hyperelastic constitutive model to simulate the forming process of non-orthogonal composite braided fabrics, taking into account the tensile and shear effects of the fibers. The shear invariant proposed by this model can be used to characterize the shear deformation of fabrics with arbitrary braiding angles. The theoretical relations were introduced to obtain the in-plane shear component for the hyperelastic model for fabrics with arbitrary braiding angles. To prove the validity of the model and shear coefficients, the bias extension test and preforming test of non-orthogonal braided fabrics were simulated. The numerical simulation results are in good agreement with the experimental results, which effectively verified the correctness of each theoretical model.

3.2 Hyperelastic modeling for non-orthogonal fabrics

3.2.1 Description of non-orthogonal fabrics

Weaving, braiding and knitting are the main methods to produce textile preforms [157]. Among them, weaving is primarily used to create woven fabrics (two interlaced yarns that are orthogonal in the initial position). The braiding technology can obtain fabrics with arbitrary braiding angles (between 5° and 85°) by setting specific braiding process specifications and mandrel parameters [16,169,170]. The fabrics obtained by the braiding machine have a three-dimensional tubular structure, and needs to be cut and opened along their axial direction to become two-dimensional flat single-layer fabrics, as presented in Fig. 3.2. Braided fabrics are flexibly used in advanced composite parts due to their variable braiding angles. Compared with woven fabrics, braided fabrics present non-symmetrical structures in two directions, so the mechanical properties of the fabric should be defined simultaneously for different directions (axial direction and transversal direction) to achieve a comprehensive grasp of the in-plane shear and tensile behaviors.

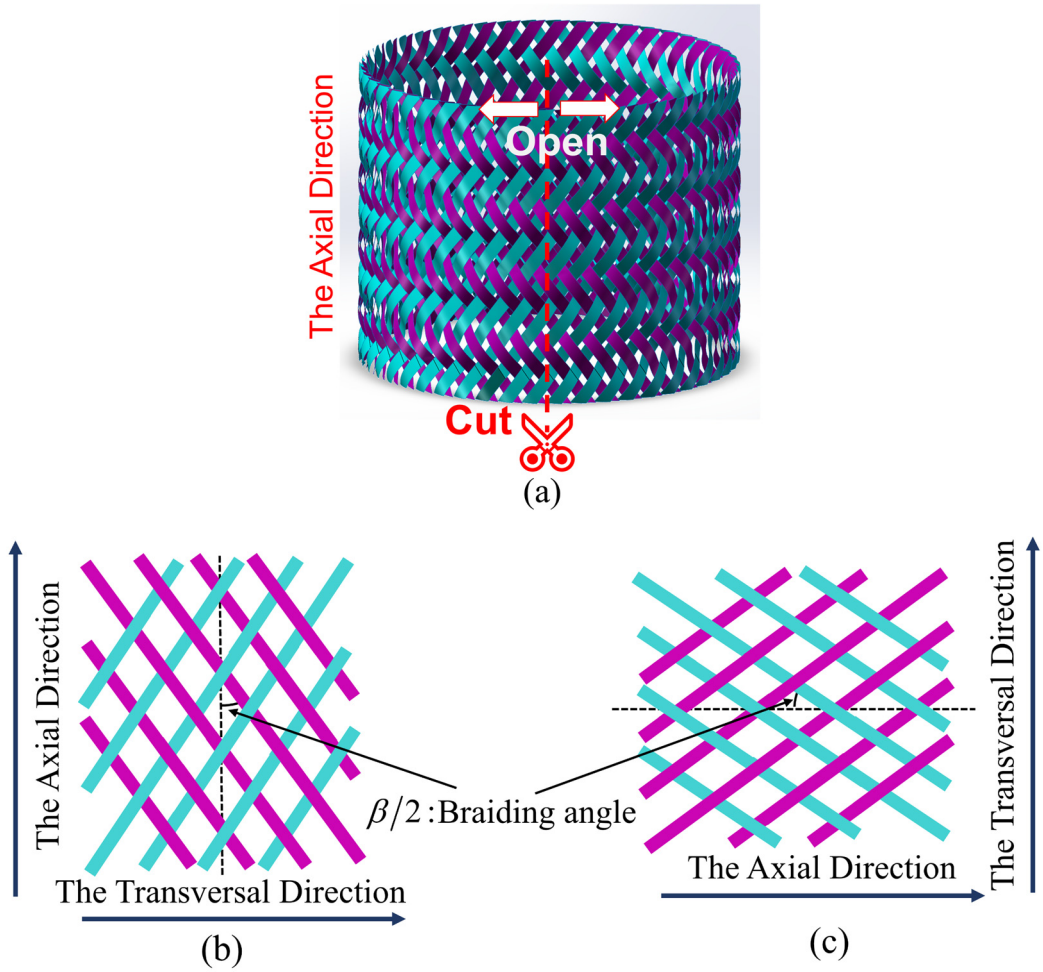

Fig. 3.2 Acquisition of 2D braided fabrics and structural diagram in two directions, (a) three-dimensional tubular braided structure, (b) the axial direction and (c) the transversal direction.

3.2.2 Description of the movement

The motion of any point in a solid region Ω in space with a boundary surface $\partial\Omega$ is described by the bijective function $\boldsymbol{\Phi}$:

$$\underline{x} = \boldsymbol{\Phi}(\underline{X}, t) \tag{3.1}$$

It provides the position vector $\underline{x}$ at time *t* for any particle that previously occupied position $\underline{X}$. For a fixed time *t*, this function defines the deformation of arbitrary point in the solid between the reference configuration C_0 and a current configuration C_t , as shown in Fig. 3.3.

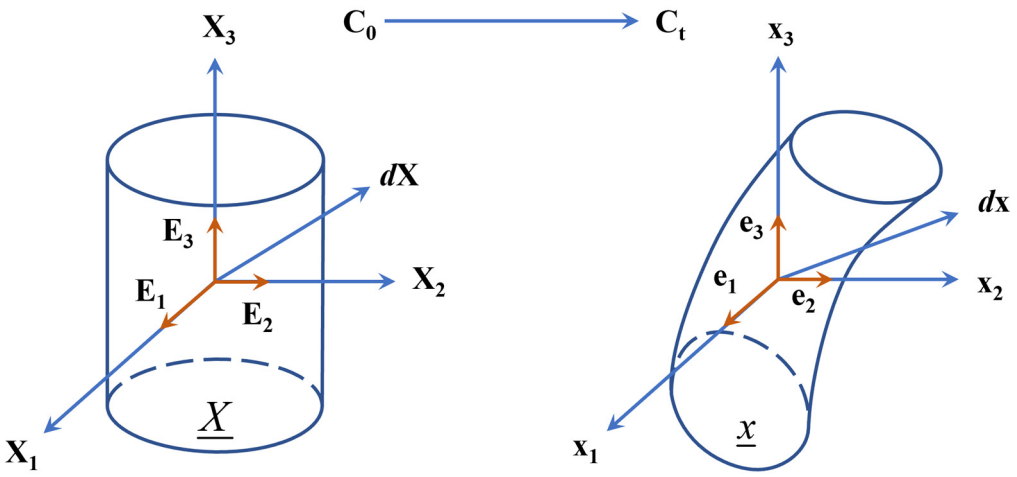

Fig. 3.3 Initial configuration C_0 and current deformed configuration C_t.

The displacement of a particle is given by the difference between its current position and its initial position. Therefore,

$$u(\underline{X},t)=\boldsymbol{\Phi}(\underline{X},t)-\boldsymbol{\Phi}(\underline{X},0)=\underline{x}-\underline{X} \tag{3.2}$$

A key quantity in deformation characterization is the deformation gradient $\underline{\underline{F}}$, which allows describing the relative spatial positions of two neighboring particles after deformation using their relative material positions before deformation. The deformation gradient is defined as:

$$\underline{\underline{F}}=\frac{\partial \underline{x}}{\partial \underline{X}} \tag{3.3}$$

Using the deformation gradient, an infinitesimal line segment $d\underline{x}$ in the current configuration can be described by the corresponding line segment $d\underline{X}$ in the reference configuration.

$$d\underline{x}=\underline{\underline{F}}\cdot d\underline{X} \tag{3.4}$$

In nonlinear continuum mechanics, various strain measurement methods are utilized, and the Green-Lagrange strain tensor $\underline{\underline{E}}$ only be considered here.

$$\begin{aligned} d\underline{x}\cdot d\underline{x}-d\underline{X}\cdot d\underline{X}&=2d\underline{X}\cdot\underline{\underline{E}}\cdot d\underline{X}\\ d\underline{x}\cdot d\underline{x}&=(\underline{\underline{F}}\cdot d\underline{X})\cdot(\underline{\underline{F}}\cdot d\underline{X})=d\underline{X}\cdot(\underline{\underline{F}}^{T}\cdot\underline{\underline{F}})\cdot d\underline{X} \end{aligned} \tag{3.5}$$

According to the above equations, the Green-Lagrange strain can be expressed as:

$$\underline{\underline{E}}=\frac{1}{2}(\underline{\underline{F}}^{T}\cdot\underline{\underline{F}}-\underline{\underline{I}}) \tag{3.6}$$

Typically, nonlinear problems involve three stress measures: Cauchy stress $\underline{\underline{\sigma}}$, the

first Piola-Kirchhoff stress $\underline{\underline{P}}$, and the second Piola-Kirchhoff stress $\underline{\underline{S}}$. In Fig. 3.4, the deformed body is virtually divided into two domains before and after deformation.

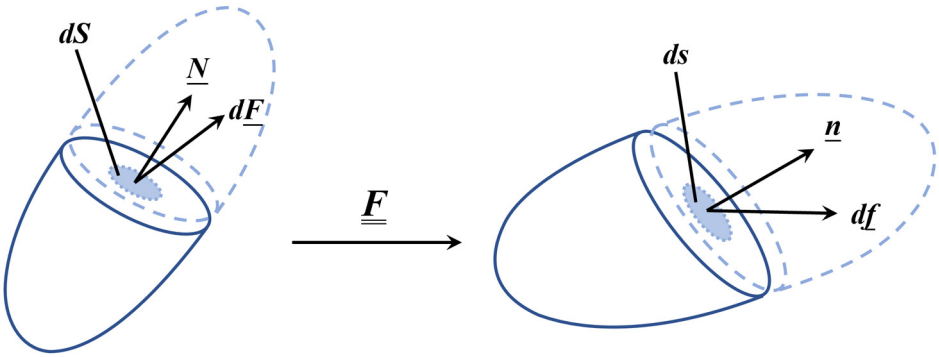

Fig. 3.4 Definition of the stress vector.

The Cauchy stress is defined as:

$$\frac{d\underline{f}}{ds} = \underline{\underline{\sigma}} \cdot \underline{n} \Leftrightarrow d\underline{f} = \underline{\underline{\sigma}} \cdot \underline{n} \cdot ds \tag{3.7}$$

Therefore, Cauchy stress represents the internal forces expressed in the current configuration. The internal forces, surface and normal vectors are all described differently. The first Piola-Kirchhoff stress $\underline{\underline{P}}$ is defined as:

$$d\underline{f} = \underline{\underline{P}} \cdot \underline{N} \cdot ds \tag{3.8}$$

The second Piola- Kirchhoff stress $\underline{\underline{S}}$ is defined by:

$$d\underline{F} = \underline{\underline{S}} \cdot \underline{N} \cdot dS \tag{3.9}$$

The relations between the three stresses can be denoted by the following equation

$$\begin{cases} \underline{\underline{\tau}} = J\underline{\underline{\sigma}} = \underline{\underline{F}}\,\underline{\underline{S}}\,\underline{\underline{F}}^T = \underline{\underline{P}}\,\underline{\underline{F}}^T \\ \underline{\underline{S}} = \underline{\underline{F}}^{-1}\underline{\underline{P}} = J\underline{\underline{F}}^{-1}\underline{\underline{\sigma}}\,\underline{\underline{F}}^{-T} \end{cases} \tag{3.10}$$

Where J is the determinant of the deformation gradient: $J = \det(\underline{\underline{F}})$

The definition of hyperelastic behavior law begins with the Clausius-Duhem inequality. The Clausius-Duhem inequality can be expressed in the initial configuration as follows.

$$\Phi_0 = -\rho_0(\dot{\Psi} - \dot{\theta}\eta) - \frac{1}{\theta}\underline{Q} \cdot \frac{\partial \theta}{\partial \underline{x}} + \underline{\underline{S}} : \underline{\underline{\dot{E}}} \geq 0 \tag{3.11}$$

With Φ_0 the dissipation per volume unit in the initial configuration, the Ψ specific

free energy per mass unit, θ the temperature, η the specific entropy, and the heat flux vector Q in the initial configuration. In the theory of "purely mechanics", thermal effects are usually overcome. The temperature is considered homogeneous in an isothermal system. So, the dissipation is written as:

$$\mathbf{\Phi}_0 = -\rho_0 \dot{\mathbf{\Psi}} + \underline{\underline{S}} : \dot{\underline{\underline{E}}} \tag{3.12}$$

A hyperelastic material is a material whose initial stain energy per unite volume $w = \rho_0 \mathbf{\Psi}$ is independent of its actual state. The material does not exhibit any dissipation or energy loss ($\mathbf{\Phi_0} = 0$) during deformation. Hence, two conditions related to the foundation of hyperelastic behavior laws are as follows:

$$\begin{cases} \dot{w}(\underline{\underline{F}}) = \underline{\underline{S}} : \dot{\underline{\underline{E}}} \\ w = w(\underline{\underline{F}}) = \rho_0 \mathbf{\Psi} \end{cases} \tag{3.13}$$

The results indicate that for the principle of material frame indifference, the strain energy is only a function of the right Cauchy-Green deformation tensor ($\underline{\underline{C}} = \underline{\underline{F}}^T \underline{\underline{F}}$).

$$\begin{aligned} w &= w(\underline{\underline{C}}) = \rho_0 \boldsymbol{\psi} \\ \dot{w}(\underline{\underline{C}}) &= \underline{\underline{S}} : \dot{\underline{\underline{E}}} = \frac{1}{2} \underline{\underline{S}} : \dot{\underline{\underline{C}}} \end{aligned} \tag{3.14}$$

Then

$$\dot{w}(\underline{\underline{C}}) = \frac{\partial w}{\partial \underline{\underline{C}}} : \frac{\partial \underline{\underline{C}}}{\partial t} = \frac{1}{2} \underline{\underline{S}} : \dot{\underline{\underline{C}}} \Leftrightarrow 0 = \left(\frac{\partial w}{\partial \underline{\underline{C}}} - \frac{1}{2} \underline{\underline{S}} \right) \Leftrightarrow \underline{\underline{S}} = 2 \frac{\partial w}{\partial \underline{\underline{C}}} \tag{3.15}$$

Eq. (3.15) is the general expression of hyperelastic behavior models. It only requires the definition of the strain-energy potential w related to the mechanical behavior of the material.

In addition, considering that the fabric materials studied in this chapter are orthotropic, the characteristics of materials are defined by three preferred directions: $\underline{M}_1$, $\underline{M}_2$ and $\underline{M}_3$. These directions allow to define the structural tensors, and it is defined as follows:

$$\underline{\underline{M}}_{ij} = \underline{M}_i \otimes \underline{M}_j, i, j = 1,3 \tag{3.16}$$

The representation theorem allows expressing the strain energy density expression as a function of transformation invariants that capture anisotropic behavior.

$$w^{orth} = w^{orth}(I_1, I_2, I_3, I_{41}, I_{42}, I_{43}, I_{412}, I_{413}, I_{423}, I_{51}, I_{52}, I_{53}) \tag{3.17}$$

Where I_1, I_2 and I_3 corresponding to the classical invariants of Cauchy-Green, and the mixed invariants are defined as:

$$\begin{aligned} I_{4i} &= \underline{\underline{C}} : \underline{\underline{\underline{\underline{M}}}}_{ii} = \underline{M}_i : \underline{\underline{C}} : \underline{M}_i \\ I_{4ij} &= \underline{\underline{C}} : \underline{\underline{\underline{\underline{M}}}}_{ij} = \underline{M}_i : \underline{\underline{C}} : \underline{M}_j \\ I_{5i} &= \underline{\underline{C}}^2 : \underline{\underline{\underline{\underline{M}}}}_{ii} = \underline{M}_i : \underline{\underline{C}}^2 : \underline{M}_i \end{aligned} \tag{3.18}$$

3.2.3 Establishment of hyperelastic model for the biaxial braided reinforcements

Hyperelastic materials refer to nonlinear elastic materials with large deformations. The stress work is only related to initial and current strain states, and is independent of deformation paths. Although friction between yarns consumes very little energy during deformation [38], the hyperelastic material can be approximately considered to have no energy dissipation in the deformation process without considering unloading, and the deformation energy required by the material is equivalent strain energy. For this reason, the constitutive model of the hyperelastic material is deduced from the strain energy function, where the energy density is usually defined by:

$$w(\underline{\underline{C}}) = \tilde{w}(I_1, I_2, \ldots, I_n) \tag{3.19}$$

Consequently, according to the section 3.2.2, the Lagrangian constitutive equation of a hyperelastic material can be written as:

$$\underline{\underline{S}} = 2\frac{\partial w(\underline{\underline{C}})}{\partial \underline{\underline{C}}} = 2\frac{\partial \tilde{w}}{\partial I_n}\frac{\partial I_n}{\partial \underline{\underline{C}}} \tag{3.20}$$

where w is the strain energy, I_n are the invariants, $\underline{\underline{S}}$ is the second Piola-Kirchhoff stress tensor, and $\underline{\underline{C}}$ is the right Cauchy-Green strain tensor. It can be directly represented by the deformation gradient tensor $\underline{\underline{F}}$ as:

$$\underline{\underline{C}}(x,t) = \underline{\underline{F}}^T \cdot \underline{\underline{F}} \tag{3.21}$$

In continuum mechanics, the deformation gradient tensor is then:

$$\underline{\underline{F}}(x,t) = \frac{\partial \underline{x}}{\partial \underline{X}} \tag{3.22}$$

where $\underline{X}$ and $\underline{x}$ are the position of a material particle in the referential configuration and the current configuration, respectively. The schematic diagram is shown in Fig. 3.3.

Finally, the Cauchy stress tensor can be expressed as:

$$\underline{\underline{\sigma}} = \frac{1}{J}\underline{\underline{F}} \cdot \underline{\underline{S}} \cdot \underline{\underline{F}}^{T} \tag{3.23}$$

where J is the Jacobian matrix. $J = \det\left(\underline{\underline{F}}\right) = \sqrt{I_3}$, I_3 represents the local change of volume during deformation.

To analyze the mechanical behavior of textile composite reinforcements, different hyperelastic models have been proposed describing the various structural types of fabrics. These models are based on formulations of physical invariants to portray the deformation modes by definition of strain energy.

The reorientation of the fabric fibers during the forming process is key to obtaining complex shapes. In the initial configuration, there are two privileged directions of fabric (as shown in Fig. 3.5), $\underline{M}_1$ and $\underline{M}_2$, respectively. The symmetry group for such a material is characterized by the structural tensors:

$$\underline{\underline{M}}_{ij} = \underline{M}_i \otimes \underline{M}_j \qquad i, j = 1, 2 \tag{3.24}$$

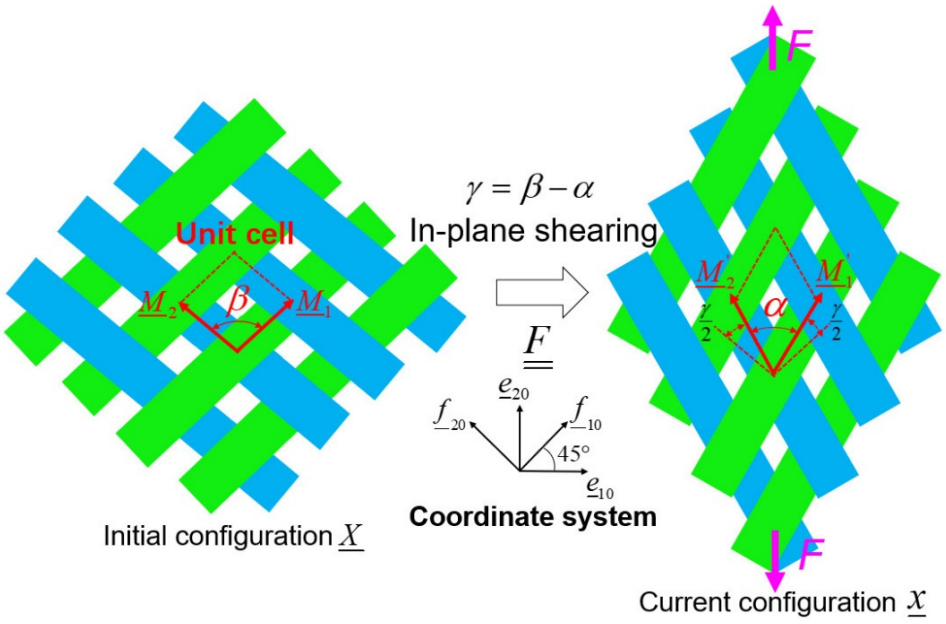

Fig. 3.5 Schematic diagram of the two principal directions in a unit cell in the initial and current configurations.

Let us assume that the deformation modes of 2D braided fabrics during formation are tension along the principal directions and shear between two threads; and that these are independent of each other. The total strain energy of the fabric can be written as the summation of the corresponding strain energies of these independent deformation modes [171]:

$$w(\underline{\underline{C}}) = w_{elong1}(I_{elong1}(\underline{\underline{C}}, \underline{\underline{M}}_{11})) + w_{elong2}(I_{elong2}(\underline{\underline{C}}, \underline{\underline{M}}_{22})) + w_{sh}(I_{sh}(\underline{\underline{C}}, \underline{\underline{M}}_{12})) \tag{3.25}$$

where w is the strain energy, $\underline{\underline{C}}$ is the right Cauchy-Green strain tensor, $\underline{\underline{M}}_{ij}$ is the structural tensors.

According to Eq. 3.25, the stress results become:

$$\underline{\underline{S}} = 2\frac{\partial w}{\partial \underline{\underline{C}}} = 2\left(\frac{\partial w_{elong1}}{\partial I_{elong1}} \cdot \frac{\partial I_{elong1}}{\partial \underline{\underline{C}}} + \frac{\partial w_{elong2}}{\partial I_{elong2}} \cdot \frac{\partial I_{elong2}}{\partial \underline{\underline{C}}} + \frac{\partial w_{sh}}{\partial I_{sh}} \cdot \frac{\partial I_{sh}}{\partial \underline{\underline{C}}}\right) \tag{3.26}$$

where I_{elong1}, I_{elong2}, I_{sh} are the invariants of elongation and in-plane shear.

The invariants along two privileged directions reflect the elongation of the yarn. As it is not affected by the braiding angle, it is the same as the tension invariants for woven fabrics and can be expressed as:

$$I_{elongi} = \ln(\sqrt{I_{4i}}) \quad i = 1,2 \tag{3.27}$$

where $I_{4i} = \underline{\underline{C}} : \underline{\underline{M}}_{ii} \quad i = 1,2$

The derivative of the elongation invariant concerning $\underline{\underline{C}}$ is given by:

$$\frac{\partial I_{elongi}}{\partial \underline{\underline{C}}} = \frac{1}{2I_{4i}} \underline{\underline{M}}_{ii} \quad i = 1,2 \tag{3.28}$$

The shear angle is a visual representation of the shear deformation mode and is the basis for calculating the shear strain energy. The definition of the shear invariant depends on the shear angle, expressed as $I_{sh} = \cos(\alpha) - \cos(\beta)$, as seen in Fig. 3.5. For woven fabrics, the shear invariant is equal to zero in the initial state. In non-orthogonal materials, due to the arbitrariness of the braiding angle, the shear invariant characterizes the angle variation between the principal directions, and the braiding angle of the fabric needs to be taken into account (Eq. 3.29). This is completely different from woven fabrics, which is also the perspective of this work.

$$I_{sh} = \frac{I_{412}}{\sqrt{I_{41} I_{42}}} - \underline{M}_1 \cdot \underline{M}_2 \tag{3.29}$$

Consequently, the derivative of the shear invariant concerning $\underline{\underline{C}}$ is given by Eq. 3.30.

$$\frac{\partial I_{sh}}{\partial \underline{\underline{C}}} = \frac{1}{2\sqrt{I_{41} I_{42}}}\left(\underline{\underline{M}}_{12} + \underline{\underline{M}}_{21}\right) - \frac{1}{2}\frac{I_{sh1}}{I_{41}}\underline{\underline{M}}_{11} - \frac{1}{2}\frac{I_{sh1}}{I_{42}}\underline{\underline{M}}_{22} \tag{3.30}$$

where $I_{412} = \underline{\underline{C}} : \underline{\underline{\underline{\underline{M}}}}_{12}$, $I_{sh1} = \dfrac{I_{412}}{\sqrt{I_{41} I_{42}}}$

3.3 Strain energy and material parameters identification

Now that the expressions for the physical invariants have been presented, each contribution to the strain energy can be expressed, in terms of the respective physical invariants, as a polynomial function. The identification of the polynomial coefficients (material parameters) is achieved by fitting simple tests, such as the uniaxial and/or biaxial tension test [134,172], the picture frame test [173–176] and the bias extension test [84].

3.3.1 Expression of elongation strain energy and shear strain energy

The strain energy associated with the tension of 2D braids is closely related to the elongation of the yarns. Consider that the elongation behavior in the two main directions is the same, but that each contribution is independent of the other. The strain energy can be expressed as an even function of the type:

$$w_{elong1} = \sum_{i=1}^{n} c_i \left(I_{elong1} \right)^{2i} \qquad w_{elong2} = \sum_{i=1}^{n} c_i \left(I_{elong2} \right)^{2i} \tag{3.31}$$

where $c_i (i = 1,2,...)$ are the tension strain energy coefficients, and the identification of which can be performed directly from a uniaxial tensile test in one of the principal directions. In this chaper, the coefficients are obtained by fitting the force-displacement curve of the single yarn under the uniaxial tensile test, more details are given in Appendix A. According to Eq. 3.31, the partial derivative of tensile strain energy with respect to the invariant is:

$$\frac{\partial w_{elongi}}{\partial I_{elongi}} = \sum_{i=1}^{N} 2i \cdot c_i \left(I_{elongi} \right)^{2i-1} \tag{3.32}$$

The in-plane shear mechanical behavior of the material is determined by using a bias-extension test or a picture frame test. The shear strain energy is expressed by a polynomial function;

$$w_{sh} = \sum_{i=1}^{n} k_i (I_{sh})^{2i} \tag{3.33}$$

In the formula, $k_i (i = 1,2,...)$ are the shear coefficients of the strain energy. The derivative with respect to the shear invariants is given by Eq. 3.34:

$$\frac{\partial w_{sh}}{\partial I_{sh}} = \sum_{i=1}^{n} 2i \cdot k_i \left(I_{sh}\right)^{2i-1} \tag{3.34}$$

3.3.2 Relations between tensile load and second Piola-Kirchhoff shear stress tensor

Determining fabric shear parameters has been widely discussed in the literature [38,177] and most of the investigations used the picture frame test to carry out the identification. For the picture frame test, the fabric is in a pure shear state under the assumption that there is no sliding between yarns and that all the power created by the external force is converted into shear strain energy. Consequently, it becomes easier to obtain shear parameters. During frame testing, misalignment can easily be introduced during clamping, which induces spurious tension during testing. At the same time, the fibers on the boundary of the picture frame are not purely sheared due to the clamping [174].

In contrast, attempting to obtain the shear parameters of materials by the bias-extension test is more accurate. It is worth noting that the pure shear behavior in the bias-extension test only occurs in a partial area of the fabric, so it is a challenge to identify the shear parameters. In this section, based on an energetic approach, the second Piola-Kirchhoff (PK2) shear stress was directly related to the traction load of the bias-extension test.

In the initial configuration, the fabric was not deformed, and the principal directions in a unit cell can be represented in the global coordinate system, as shown in Fig. 3.5.

$$\underline{M}_1 = \sin\left(\frac{\beta}{2}\right)\underline{e}_{10} + \cos\left(\frac{\beta}{2}\right)\underline{e}_{20} \tag{3.35}$$

$$\underline{M}_2 = -\sin\left(\frac{\beta}{2}\right)\underline{e}_{10} + \cos\left(\frac{\beta}{2}\right)\underline{e}_{20} \tag{3.36}$$

When the fabric was stretched, the fibers became reoriented, and the components of the principal directions were thus:

$$\underline{M}_1^{'} = \sin\left(\frac{\beta-\gamma}{2}\right)\underline{e}_{10} + \cos\left(\frac{\beta-\gamma}{2}\right)\underline{e}_{20} \tag{3.37}$$

$$\underline{M}_2^{'} = -\sin\left(\frac{\beta-\gamma}{2}\right)\underline{e}_{10} + \cos\left(\frac{\beta-\gamma}{2}\right)\underline{e}_{20} \tag{3.38}$$

From the kinematics of the bias-extension test one can obtain the deformation gradient $\underline{\underline{F}}$:

$$\underline{\underline{F}} = \frac{1}{\sin\left(\frac{\beta}{2}\right)} \cdot \sin\left(\frac{\beta}{2} - \frac{\gamma}{2}\right) \underline{e}_{10} \otimes \underline{e}_{10} + \frac{1}{\cos\left(\frac{\beta}{2}\right)} \cdot \cos\left(\frac{\beta}{2} - \frac{\gamma}{2}\right) \underline{e}_{20} \otimes \underline{e}_{20} \quad (3.39)$$

When $\beta = 90°$, the deformation gradient is expressed as:

$$\underline{\underline{F}} = \sqrt{2} \cdot \sin\left(\frac{\pi}{4} - \frac{\gamma}{2}\right) \underline{e}_{10} \otimes \underline{e}_{10} + \sqrt{2} \cdot \cos\left(\frac{\pi}{4} - \frac{\gamma}{2}\right) \underline{e}_{20} \otimes \underline{e}_{20} \quad (3.40)$$

where $(\underline{e}_{10}, \underline{e}_{20})$ is the global coordinate system and $\underline{e}_{20}$ follows the tensile direction. From the deformation gradient, the right Cauchy Green strain tensor $\underline{\underline{C}} = \underline{\underline{F}}^T \underline{\underline{F}}$ and its derivative with respect to time $\dot{\underline{\underline{C}}}$ are:

$$\begin{cases} \underline{\underline{C}} = \left(\dfrac{\sin\left(\frac{\beta - \gamma}{2}\right)}{\sin\left(\frac{\beta}{2}\right)} \right)^2 \underline{e}_{10} \otimes \underline{e}_{10} + \left(\dfrac{\cos\left(\frac{\beta - \gamma}{2}\right)}{\cos\left(\frac{\beta}{2}\right)} \right)^2 \underline{e}_{20} \otimes \underline{e}_{20} \\ \dot{\underline{\underline{C}}}(t) = \dfrac{1}{2} \cdot \dot{\gamma}(t) \cdot \sin(\beta - \gamma) \left(\dfrac{-1}{\sin^2\left(\frac{\beta}{2}\right)} \underline{e}_{10} \otimes \underline{e}_{10} + \dfrac{1}{\cos^2\left(\frac{\beta}{2}\right)} \underline{e}_{20} \otimes \underline{e}_{20} \right) \end{cases} \quad (3.41)$$

At the same time, for the woven fabrics:

$$\begin{cases} \underline{\underline{C}} = (1 - \sin(\gamma)) \underline{e}_{10} \otimes \underline{e}_{10} + (1 + \sin(\gamma)) \underline{e}_{20} \otimes \underline{e}_{20} \\ \dot{\underline{\underline{C}}}(t) = \dot{\gamma}(t) \cdot \cos(\gamma) (-\underline{e}_{10} \otimes \underline{e}_{10} + \underline{e}_{20} \otimes \underline{e}_{20}) \end{cases} \quad (3.42)$$

where γ is the shear angle.

As mentioned in the literature [178], the fabric consists of three different partitions (A, B and C) during the bias-extension test. Zone A namely “no-deformed zone”, Zone B called “semi-shear zone” and Zone C is “pure shear zone”, as shown in Chapter II (Fig. 2.2). Assuming that the only mode of deformation in the specimen is pure shear, the external power due to machine forces can be related to the internal power due to shear forces in each zone. However, the only deformation mode involved in this balance are zones B and C, since zone A is not deformed. In a quasi-static tensile test, the load (F) on the specimen is related to the second Piola-Kirchhoff stress according to the

principle of equal internal (P_{int}) and external power (P_{ext}).

$$F(\gamma)\dot{u} = P_{int}^{(B)} + P_{int}^{(C)} = \frac{1}{2}\int_{\Omega_0} \underline{\underline{S}} : \dot{\underline{\underline{C}}} dV_0 \tag{3.43}$$

By integrating the energy on the initial effective surfaces of the specimen, the relationship between the external force and the components of the PK2 tensor can be deduce

$$F(\gamma) = \frac{1}{4}\dot{\gamma}(u)\cdot h\cdot\left(\sin(\beta-\gamma)\cdot Z_C\left(-\frac{S_{11}(\gamma)}{\sin^2\left(\frac{\beta}{2}\right)}+\frac{S_{22}(\gamma)}{\cos^2\left(\frac{\beta}{2}\right)}\right)+\sin\left(\beta-\frac{\gamma}{2}\right)\cdot\frac{Z_B}{2}\left(-\frac{S_{11}\left(\frac{\gamma}{2}\right)}{\sin^2\left(\frac{\beta}{2}\right)}+\frac{S_{22}\left(\frac{\gamma}{2}\right)}{\cos^2\left(\frac{\beta}{2}\right)}\right)\right) \tag{3.44}$$

Where $S_{11}(\gamma)$ and $S_{22}(\gamma)$ are diagonal stress components in the pure shear zone of the specimen, $S_{11}\left(\frac{\gamma}{2}\right)$ and $S_{22}\left(\frac{\gamma}{2}\right)$ are stress components in the semi-shear zone, Z_B and Z_C are the initial surface area of zones B and C. u is the tensile displacement of the sample, $\dot{\gamma}(u) = \frac{1}{L_c\cdot\sin\left(\frac{\alpha}{2}\right)}$. h is the thickness of the sample. The specific geometric relationship can be found in Chapter II (section 2.2.1).

3.4 Forming simulation of 2D biaxial braided reinforcements

3.4.1 Simulation of bias-extension test

(1) Experimental setup

The specific setup of bias-extension tests has been described in Section 2.2.2 of Chapter II. The properties of fabrics are in Table 2.1. To comprehensively investigate the mechanical properties of the fabric, the test was carried out on the axial and transversal directions of the fabric. The dimensions of the samples are shown in Table 2.2. The tests were selected to analyze the fabric in the axial direction corresponding to different aspects (r=4 and r=6). The experiments were carried out by the Gemtex laboratory in the university of Lille.

(2) Simulation analysis

The relation, resulting from the energy approach, between the load and the shear stress PK2 was used to obtain the shear parameters. The Levenberg–Marquardt algorithm is proposed to get a numerical solution for nonlinear minimization. According to Eq. 3.44, by using the Levenberg–Marquardt algorithm to interpolate the

average experimental results of bias-extension tests (shown in Fig. 3.6) with geometric ratios, which were 4 in the axial direction and 1.67 in the transversal direction, the shearing coefficients in Eq. 3.33 could be determined, and are summarized in Table 3.1. Using this algorithm, only three sets of shear coefficients were obtained without an overfitting problem.

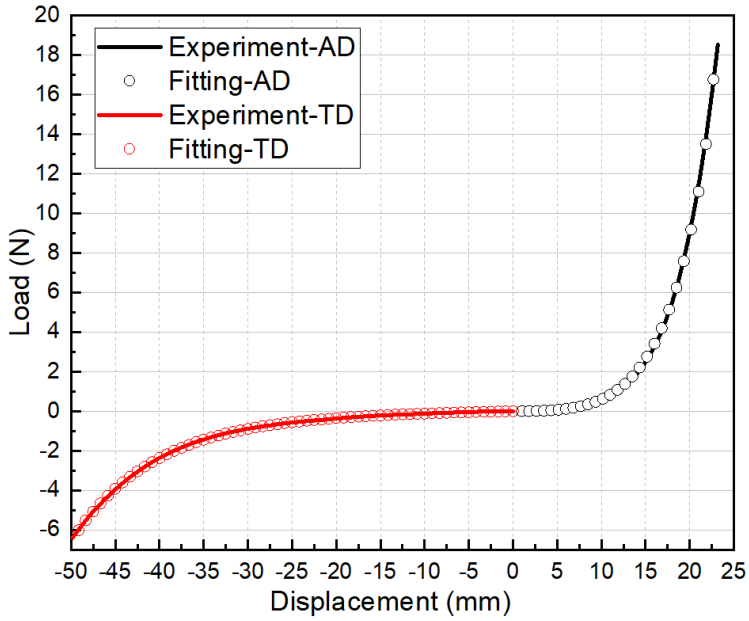

Fig. 3.6 Identification of shear parameters for flax/PA12 in the axial and transversal directions.

Table 3.1 The shear coefficients of the strain energy

Fabric types	Axial direction (J/mm^2)	Transversal direction (J/mm^2)
Flax/PA12	$k_1=0.000251$, $k_2=0.0563$, $k_3=0.2086$	$k_1=0.0023$, $k_2=0.0019$, $k_3=0.0011$

Different directions of Flax/PA12 were selected to simulate the bias-extension test. According to the experimental conditions, one end of the fabric was fixed and the other end was subjected to a displacement load along the tensile direction. The simulation results of the bias-extension test and a comparison with an experimental approach are shown in Fig. 3.7, which presents the distribution of the shear angles. According to the simulation results, the fabric was asymmetrical in the axial and transversal directions due to the non-orthogonal structure of the braided preform. The three different zones could be clearly seen in both types of fabrics (as mentioned in Fig. 2.2 of Chapter II: no

deformation in zone A, semi-shear deformation in zone B and pure shear deformation in zone C).

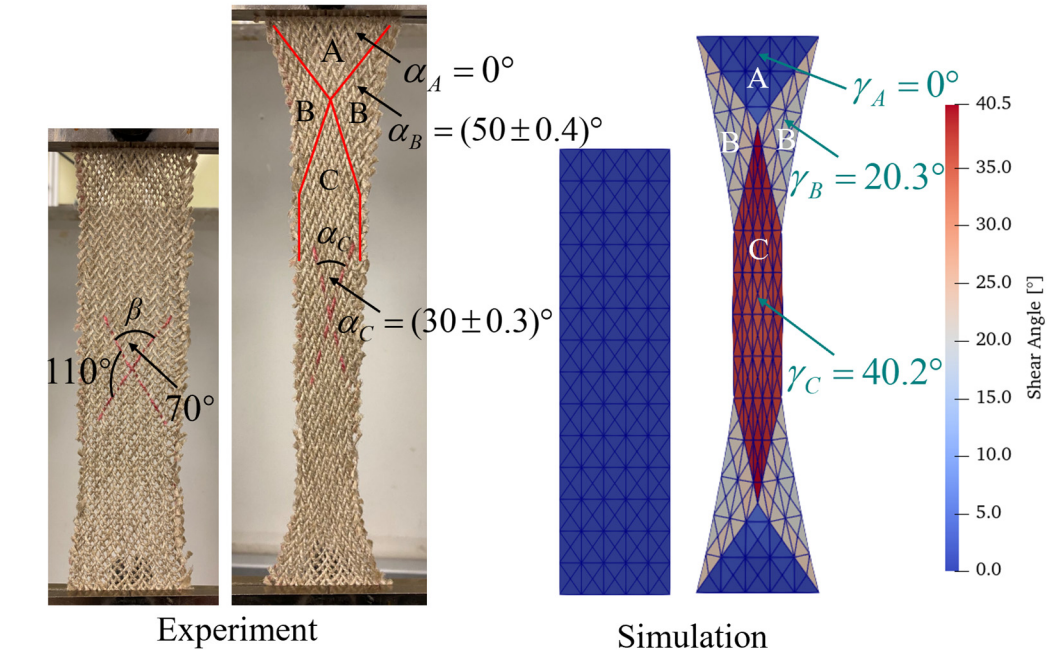

(a) axial direction

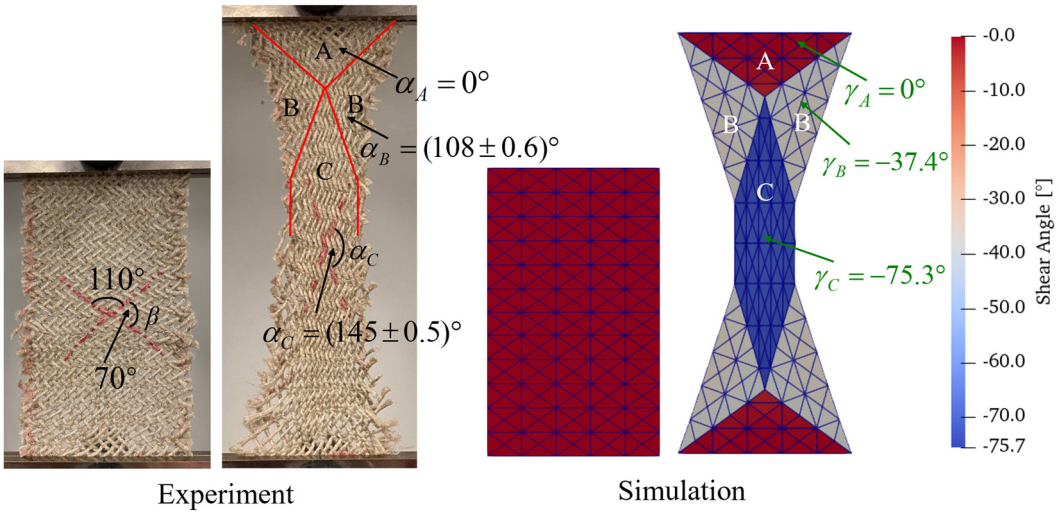

(b) transversal direction

Fig. 3.7 In-plane shear angles during the bias-extension tests.

Eq. 2.6 in Chapter II gives the theoretical model for calculating the shear angle in the pure shear zone (zone C), and the theoretical value of the in-plane shear angle in the tensile process can be obtained by substituting the experimental displacement into the equation. Comparing the simulation results of the selected fabric in the axial and

transversal directions with the theoretical model, the relation between the shear angle (in the pure shear zone) and displacement could be determined and is portrayed in Fig. 3.8. The different ratios (r) of the length to the width of the fabric were compared. The predicted shear angle using the shearing parameters (Table 3.1) was in good agreement with its theoretical counterpart.

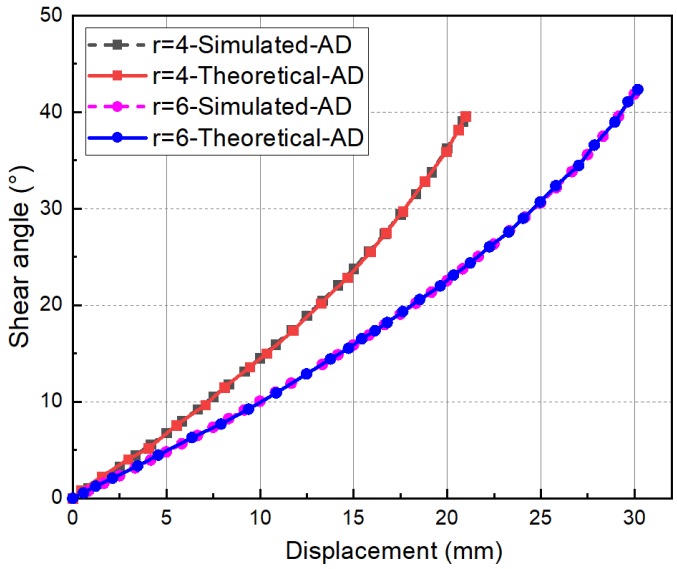

(a)

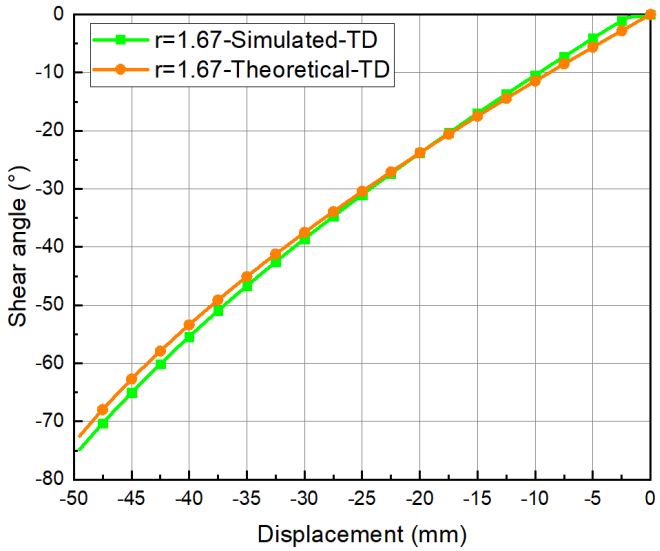

(b)

Fig. 3.8 Comparison of shear angle between theoretical and simulated values in (a) the axial direction (AD) and (b) the transversal direction (TD).

3.4.2 Simulation of hemispherical forming process

(1) Experimental setup

Forming experiments with hemispherical punches were carried out on a specific preforming device at room temperature, and the schematic diagram of the device is shown in Fig. 3.9 (a). The device was able to provide a variation of forming conditions for the textile reinforcement to achieve the desired double-curved shape. The flax/PA12 fabric was used in the forming test, and was initially a 155mm×155mm square. The thickness of the fabric was 2.06 mm and the braiding angle was 35° (Fig. 3.9 (b)). The main properties of the textile were the same as those in Table 2.1. During the forming process of non-orthogonal braided fabrics, both tensile and shear strain energies need to be considered. The coefficients used to characterize the tensile strain energy and the shear strain energy are obtained by experiments. It is noteworthy that the coefficients (c_i) of tensile strain energy obtained from the data of uniaxial tensile tests of a single yarn (flax/PA12) and the value is 181. The coefficients (k_i) of shear strain energy were obtained from bias-extension test as described in Table 3.1. The pressure required during the test was provided by pneumatic jacks. In order to compare the preforming results, draping experiments were conducted with 0.05 and 0.2 MPa pressure.

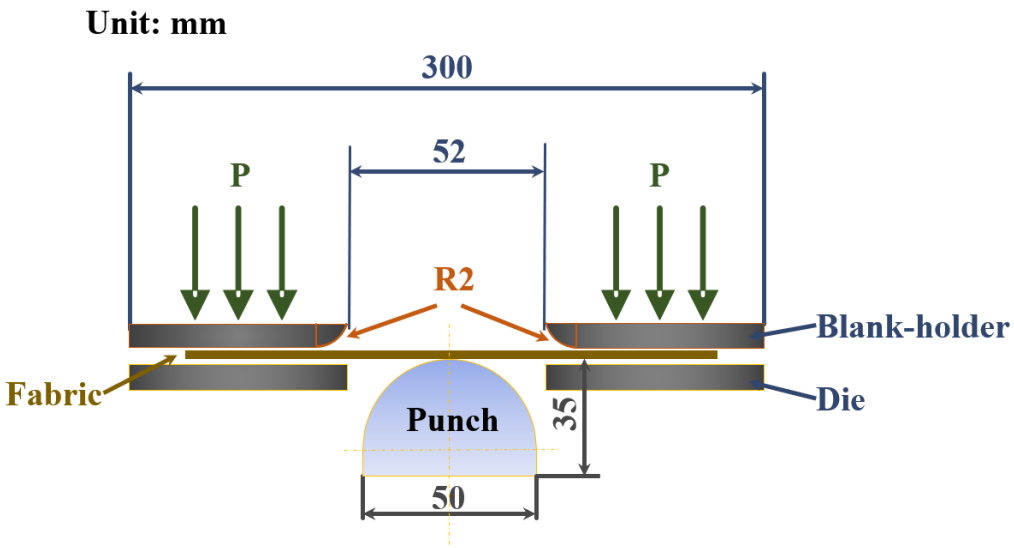

(a)

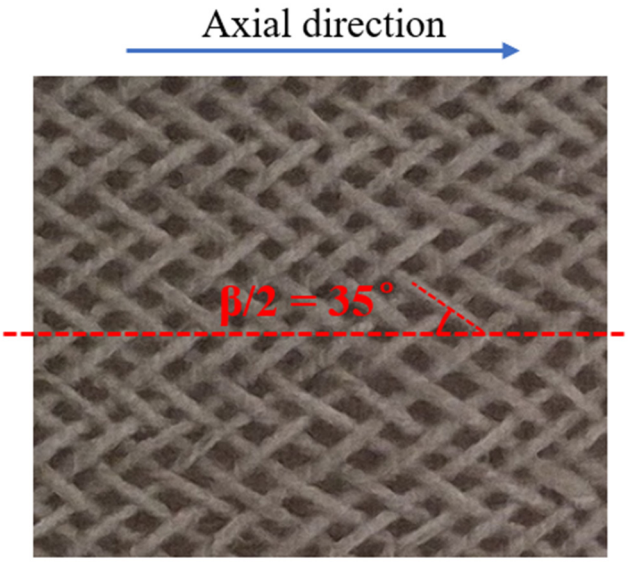

(b)

Fig. 3.9 (a) Schematic diagram of the preforming test and (b) the flax/PA12 braided fabric sample.

(2) Simulation analysis

The preforming process of hemispheric stamping was simulated by using the non-orthogonal hyperelastic model proposed in section 3.2. This model was implemented in a nonlinear explicit finite element code provided by Innovamics. In the draping simulation of the fabric, finite element models of the fabric and the experimental setup were constructed. The blank was modeled by triangular membrane elements (the element size was 3 mm) and a penalty approach was used to model the contact. For the punch and die, the contact-triangle elements were used and the size of the elements was 3mm. For the fabric, the membrane elements were used and the size was 2mm.

For the preforming simulation by the FE analysis, the geometry of the forming tool (punch, die and holder) is given in Fig. 3.10. The different pressures were uniformly applied to the holder and the friction coefficient between the fabric and the tool was set to 0.2. To improve the computational efficiency, only a quarter of the fabric was modeled to take into account the symmetry of the forming process. The entire draping simulation process is summarized as: the fabric is placed flat on the die, the pressure was applied on the blank to press the fabric and the velocity boundary condition was used to control the punch speed (50 mm/min) to drape the fabric.

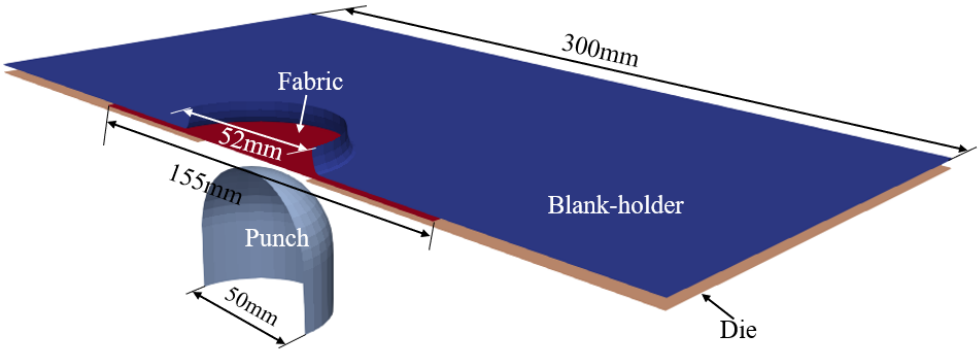

Fig. 3.10 The geometry of the forming tool in numerical simulation analysis.

Fig. 3.11 shows the comparison between the deformed shape of a braided fabric predicted by the hyperelastic model and its experimental counterpart at 0.2 MPa pressure of the blank-holder. The two shapes exhibited decent consistency. It was found that the non-orthogonal braiding angles led to deformation differences in the fabric in the axial and transversal directions. The forming of the hemisphere of the braided fabric is asymmetric. The fabric presented a draw-in phenomenon along the axial direction, accompanied by in-plane shear. Furthermore, small changes were observed in the transversal direction. At the same time, two significant intra-ply shear behaviors appeared in the axial direction, and the local fiber volume fraction in the shearing regions was higher than in other regions.

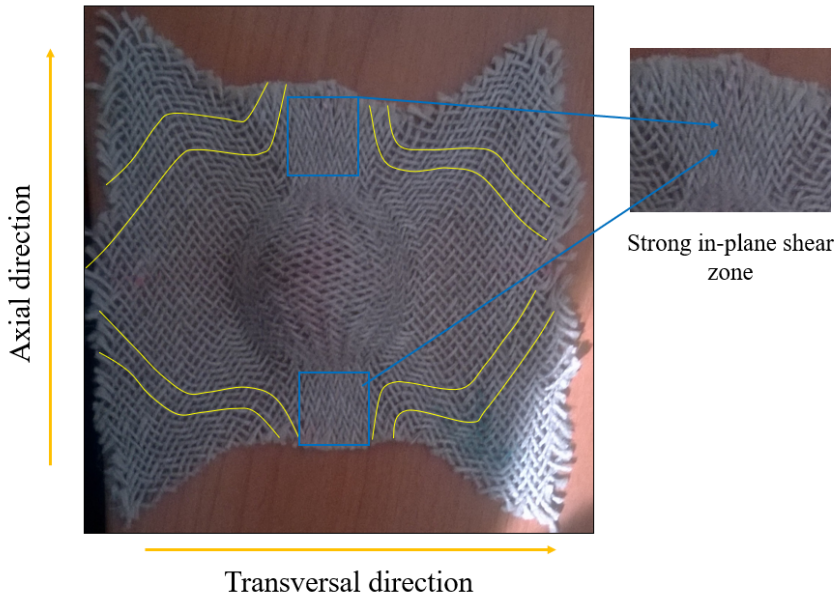

(a)

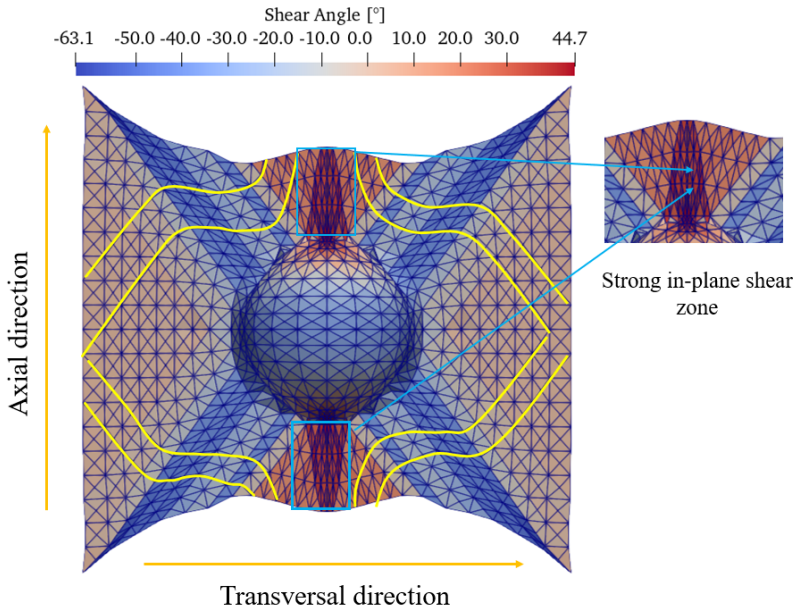

(b)

Fig. 3.11 Deformed braids after preforming under 0.2 MPa pressure of the blank-holder, (a) experimental approach and (b) numerical simulation.

Under the pressure of 0.05 and 0.2 MPa, the deformed boundary profile of the simulated fabric was compared with the experiment, as shown in Fig. 3.12. According to a direct comparison of the area of maximum error, the simulation results were consistent with their experimental counterparts. The simulation could thus give a satisfactory portrayal of the preformed shapes, with errors ranging from approximately 0% to 12%, which could be reasonably accepted.

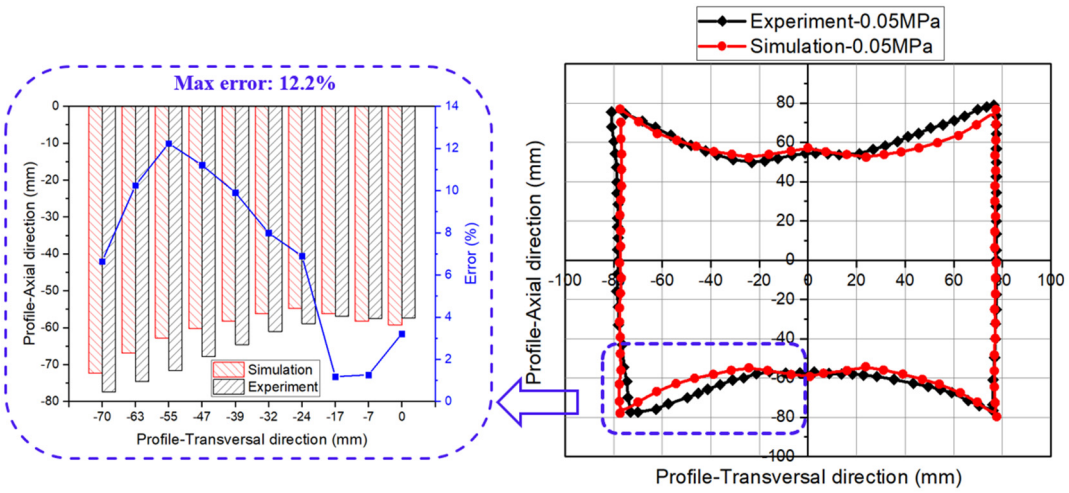

(a)

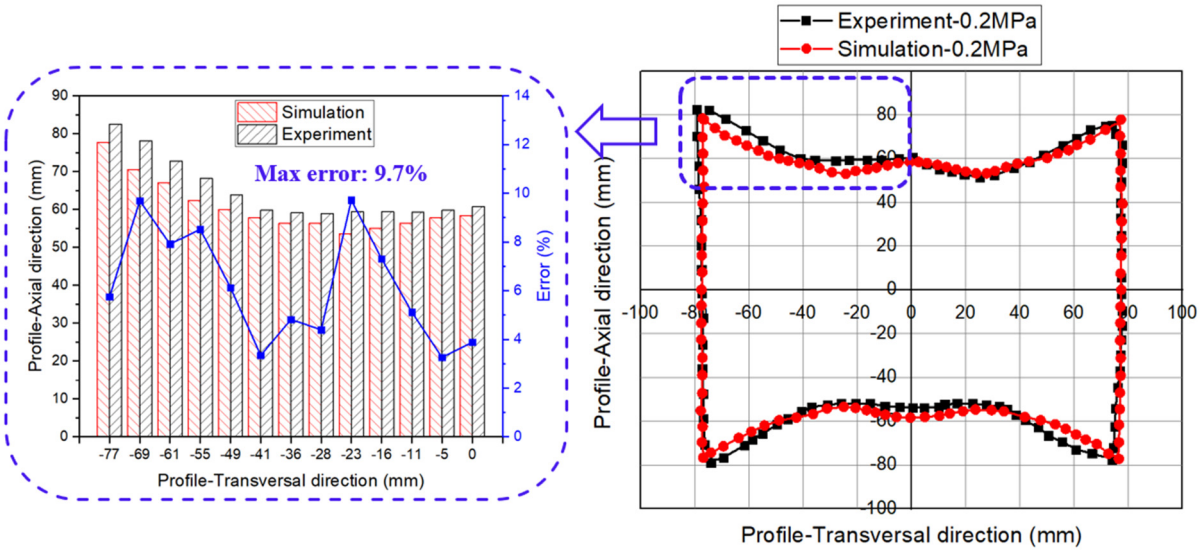

(b)

Fig. 3.12 Comparison of the deformed boundary profile under different preforming conditions, (a) 0.05 MPa and (b) 0.2 MPa blank-holder pressure.

The shear angle is an important reference when it comes to predicting the wrinkling of the deformed part and the key to calculating the fiber volume fraction. Accurate prediction of the shear angle distribution is of great significance for fabric forming optimization. In order to obtain accurate shear angle results, the fabric was divided into 17 zones according to the shear angle distribution presented by the test, as shown in Fig. 3.13. The average value of the shear angle for each zone was computed and compared with the simulation results, as can be seen in Fig. 3.14. The maximum errors of shear angle at a pressure of 0.05 MPa and 0.2 MPa were 9.3% and 8.2%, respectively. The maximum shear angle occurred in the transition region between the double dome curve surface and the flat area of the fabric (zone 13). So, the effectiveness and accuracy of the numerical predictions on the shear angles were vindicated from the comparison. Furthermore, the measured shear angles and deformed profiles and simulation results showed excellent agreement establishing the reliability of the hyperelastic model.

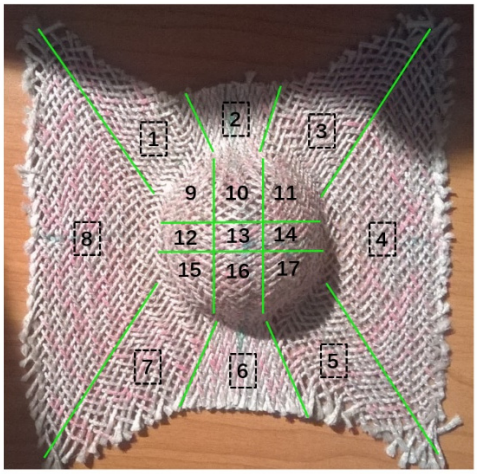

(a) 0.05 MPa-Experiment

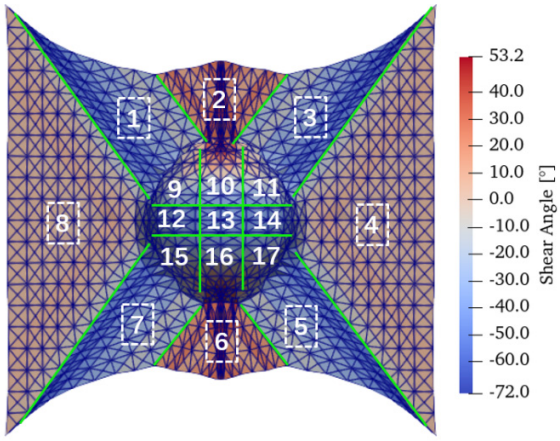

(b) 0.05 MPa-Simulation

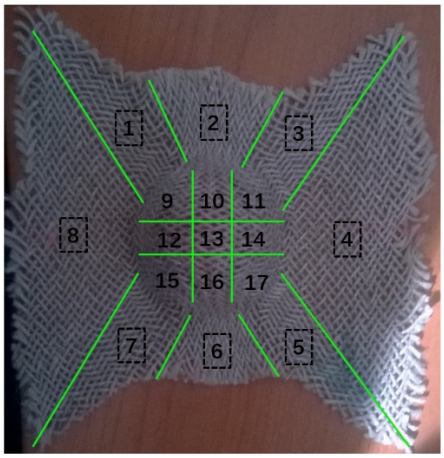

(c) 0.2 MPa-Experiment

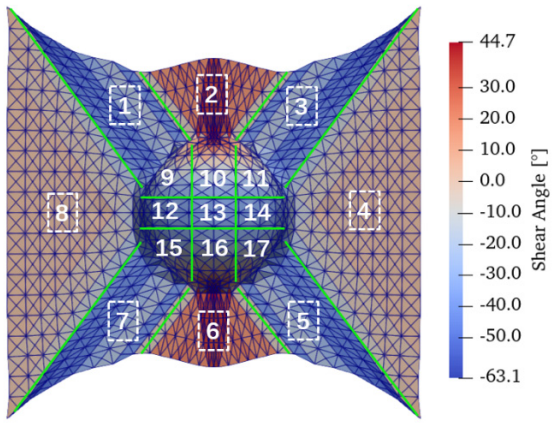

(d) 0.2 MPa-Simulation

Fig. 3.13 Deformed braids after hemispherical preforming obtained by experimental and numerical simulation approaches under different blank-holder pressures.

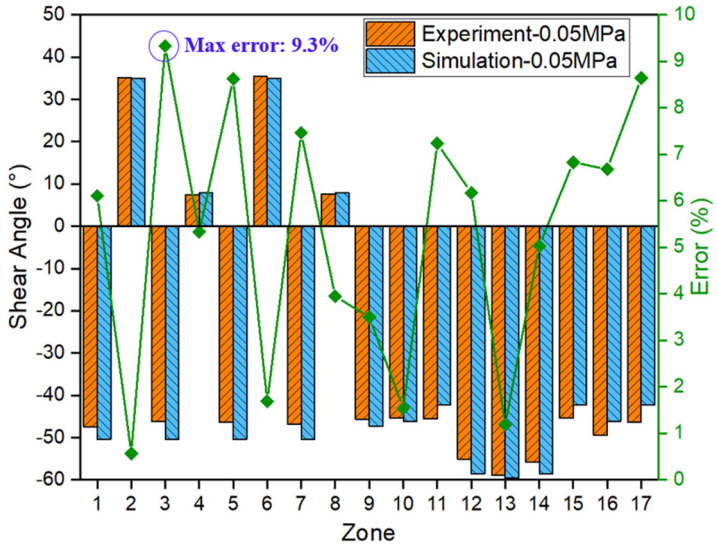

(a) blank-holder pressure of 0.05 MPa

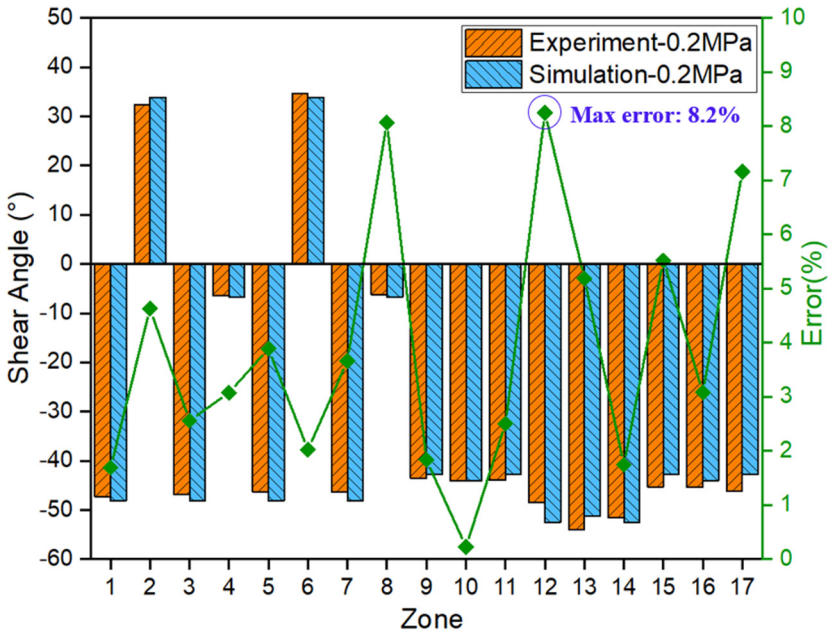

(b) blank-holder pressure of 0.2 MPa

Fig. 3.14 Comparison of in-plane shears between experiment and numerical simulation approaches in 17 different zones.

3.5 Conclusion of Chapter III

The present chapter proposed a new hyperelastic model to characterize the mechanical behavior of non-orthogonal braided fabrics during a preforming process. Tension and shear deformation modes were introduced to describe the relationship between strain energy and invariants. In particular, the shear invariant presented in this chapter can be applied to braided fabrics with arbitrary angles and is not limited to woven fabrics. At the same time, a theoretical relation between the second Piola-Kirchhoff stress tensor and the tensile load was established to predict the shear coefficients in the hyperelastic model by utilizing the data of the bias-extension test. To examine the validity of the model, the bias-extension test and hemispherical test of non-orthogonal braided fabrics were also simulated, and good agreement was found between the numerical simulation results and their experimental counterparts, thus proving the validity of the numerical model. Furthermore, the hyperelastic constitutive model improved in this chapter will be continued to analyze the forming of tubular fabrics in Chapter IV.

IV. Analysis and simulation on formability behaviors of tubular

Résumé en français

Les composites tubulaires tridimensionnels sont des matériaux multi-composants composés d'une matrice et de préformes textiles tridimensionnelles. Ils présentent des propriétés mécaniques similaires à celles des métaux, mais sont plus légers et offrent une meilleure résistance à la corrosion que les métaux. Ce matériau composite est une structure tubulaire complexe à plusieurs couches avec un intérieur creux et d'une certaine épaisseur. Le textile sert de matériau de renforcement pour la structure tubulaire et présente un grand potentiel. Ce renforcement tubulaire peut être directement formé par mise en forme en continue, ce qui entraîne une grande stabilité structurelle comme illustré dans la Fig. 4.1. Par rapport aux renforcements tubulaires formés après coup, il évite les concentrations de contraintes causées par les défauts de la mise en forme, ce qui se traduit par une distribution de charge plus uniforme sur le renfort textile. Les renforcements tubulaires tridimensionnels peuvent être préparés par tissage, tressage et tricotage. Les renforts tissés ont des angles de tissage fixes et un seul motif structural, tandis que les renforts tricotés ont un facteur de couverture plus faible et une rigidité moindre, ce qui les rend inadaptés aux structures de grande portée. Par conséquent, les renforcements préparés par des méthodes de tressage sont devenus l'objet d'attention dans les matériaux composites tubulaires. Les tressés offrent une flexibilité dans les angles de tressage, permettant l'ajustement de la direction et de la quantité de fil en fonction des besoins spécifiques, ce qui entraîne une plus grande variété de motifs de tissu et des performances supérieures. Ces excellentes propriétés font que les composites tressés tubulaires soient largement utilisés dans les domaines de l'aérospatiale, de l'armement, de la médecine et du sport, ainsi que dans le transport de pétrole et de gaz naturel (pipeline).

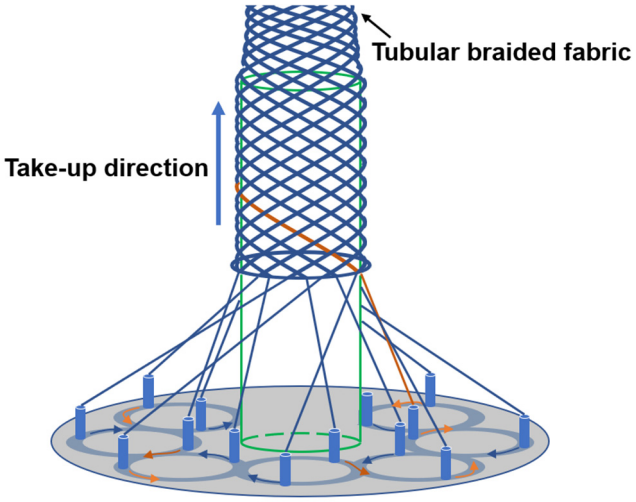

Fig. 4.1 Tressage et le renfort tubulaire.

À l'heure actuelle, les composants composites tubulaires sont encore confrontés à des défis importants pour réduire davantage le poids et les coûts tout en améliorant leurs propriétés mécaniques. Les propriétés mécaniques de ces composants dépendent largement des propriétés mécaniques des renforts qui les composent. Le chapitre II portait sur l'analyse de la réponse mécanique des tresses tubulaires à structure creuse sous des charges de traction axiale, révélant que ce type de renfort subit une contraction radiale tout en s'étirant axialement. Ce comportement est étroitement lié au cisaillement dans le plan du renfort textile. De plus, ce comportement facilite la mise en forme de la tresse tubulaire sur différents moules. En plaçant le renfort à structure creuse sur des moules de formes diverses et en soumettant le renfort textile à des charges de traction axiale, le textile adhère à la surface extérieure des moules. Sous l'influence de la charge de traction, le renfort textile présente un comportement de cisaillement, qui est supprimé au contact du moule. Compte tenu de la complexité de la déformation du textile, il est difficile d'étudier de manière exhaustive les facteurs qui influencent le comportement mécanique des renforts textiles uniquement par des expériences. Par conséquent, sur la base de l'analyse expérimentale, la méthode de simulation est un moyen efficace d'éviter un développement expérimental coûteux.

En analyse numérique, les modèles constitutifs appropriés sont cruciaux. La tresse tubulaire étudiée dans cet article est préparée à partir de fibres naturelles, ce qui peut être considéré comme un continuum. Par conséquent, en se basant sur la mécanique des milieux continus, le chapitre III a établi un modèle hyperélastique pour caractériser le

comportement mécanique des tresses non orthogonales. Ce chapitre continue d'utiliser le modèle hyperélastique pour analyser les propriétés mécaniques des renforts tubulaires tressés. Selon les tests mécaniques des tresses tubulaires, les caractéristiques de contraction radiale et l'inhomogénéité de cisaillement sont reflétées dans la simulation.

Mots-clés: Renforts tressés tubulaires, Simulation numerique, Modèle hyperelastique, Mise en forme

4.1 Introduction

Tubular braided fabrics prepared directly from braiding machines are widely used due to their excellent integrity. The mechanical properties of the fabric are crucial, which determine the mechanical performance of the composite tubes. In order to investigate the mechanical characteristics of the fabric, this thesis explores both experimental and simulation aspects. In Chapter II, experimental tests on tubular braided fabrics are conducted to investigate the deformation of the fabrics under axial tensile loads and a theoretical model for characterizing the shear behavior of the fabrics is developed. In this chapter, the tensile and preforming of tubular fabrics are simulated based on the hyperelastic constitutive model proposed in Chapter III to simulate the mechanical behavior of non-orthogonal fabrics. Firstly, the mechanical parameters used to characterize the shear behavior of the tubular fabric are fitted based on the experimental data and the theoretical model obtained from Chapter II. Then, the shear parameters were used to simulate the stretching process of the fabric, and the profile of the fabric under different tensile deformation conditions (25%, 50%, 75%) was obtained and compared with the experiment. The good comparison results showed the validity of the simulation model. Furthermore, based on the radial contraction effect of the fabric under tensile loads, this chapter analyzes the preforming process of tubular fabrics. It is found that the shear deformation of the fabric facilitates preforming on molds of different shapes, leading to different preforming shapes. Meanwhile, the shear behavior during the forming process is also investigated.

4.2 Materials and Methods

4.2.1 Tensile test of tubular fabrics.

To investigate the mechanical properties of the tubular braided reinforcement, tensile tests have been conducted to obtain the mechanical response of the fabrics, as described in section 2.3.1 of Chapter II. The tubular fabric is made of commingled yarns with 64% flax and 36% polyamide 12 (flax/PA12), the braiding angle (β/2) shown in Fig. 2.4 (a) is 55°. The length of the fabric is 40 mm (excluding the clamping area) and the diameter is 50 mm. The specific parameters are shown in Table 2.3. The tensile test was carried out on the Instron tensile machine in the LPMT Laboratory with a load cell is 250 kN. The experimental setting can be shown in Fig. 2.5. The two ends of the fabric are fixed

to the tensile machine by the corresponding clamps to avoid sliding. All of the tests were performed at a constant speed of 10 mm/min and repeated at least three times. The shear angle was measured by an optical measurement and deformation was recorded by 3D scanning equipment (GOM) during the test. The variation of tensile load with displacement is output by the tensile machine.

4.2.2 Preforming test of tubular fabrics

It can be seen from Section 2.3 of Chapter II that a fabric will undergo radial shrinkage along its circumference under axial load, which depends on the elongation and shear effect of the yarn in the fabric. Taking advantage of this characteristic of the fabric, the preforming test of fabric was investigated under tensile load. Tetrahedral and cylindrical models were chosen in the present section to investigate the formability of tubular braided fabrics.

The preforming test of the tubular fabric is set up as shown in Fig. 4.2 and the experiment is still conducted on the Instron tensile machine. Firstly, the mold is fixed on the tensile machine, and then the tubular fabric is placed over the outer surface of the mold. During this process, it is important to maintain the original shape of the fabric to prevent it from being stretched. One end of the fabric is fixed to the mold, while the other end is connected to the tensile machine. The fabric is stretched by the tensile machine at a speed of 10 mm/min and gradually fitted to the mold to obtain the desired shape. Moreover, to get the elongation of a single yarn, the fabric will be marked by points along the same yarn (Fig. 4.2). The experimental results recorded by the camera used in the experiment will be processed in Image J software, and the marker-based tracking approach is used to get the material deformation.

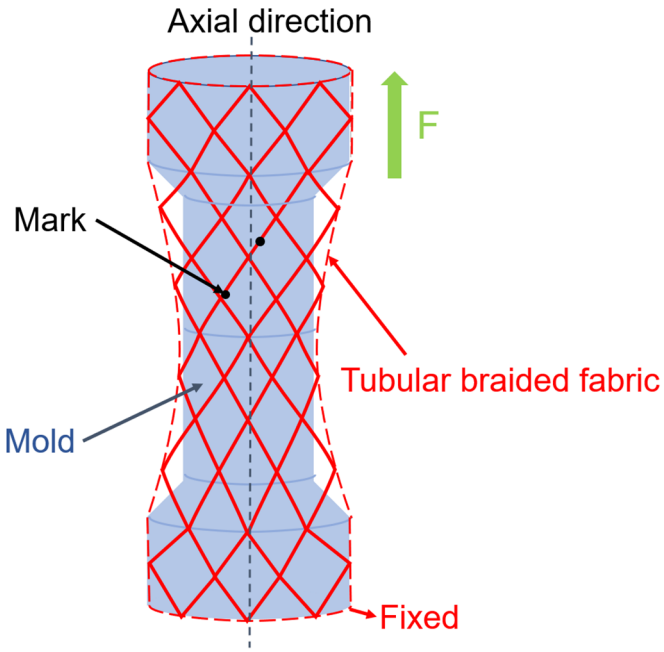

Fig. 4.2 Schematic illustration of the tubular braided fabric preforming process.

4.2.3 Identification of shear coefficients of tubular fabrics in the hyperelastic model

The simulation analysis theory of fabric adopts the hyperelastic constitutive model proposed in Chapter III. The constitutive model uses the invariant in deformation to describe the corresponding strain energy. For the tensile strain energy, its magnitude depends on the material properties of the fabric and is independent of the fabric structure, the coefficient c_i of tensile strain energy is consistent with that mentioned in Chapter III. For the shear strain energy, the shear coefficient in the constitutive model changes as the structure of the fabric changes. Therefore, the theory for determining the shear coefficient of the fabric needs to be re-established. For a three-dimensional (3D) tubular fabric, when a tensile load is applied along its axial direction, the intersecting yarns in the fabric will mutually rotate along the intersection point causing the shear effect, which is the same as the in-plane shear behavior of a flat fabric.

The shear deformation gradient ($\underline{\underline{F}}$) and the right Cauchy Green strain tensor ($\underline{\underline{C}}$) of the fabric are easily obtained:

$$\underline{\underline{F}} = \frac{\partial \underline{x}}{\partial \underline{X}} = \frac{1}{\sin\left(\frac{\beta}{2}\right)} \cdot \sin\left(\frac{\beta}{2} - \frac{\gamma}{2}\right) \underline{e}_{10} \otimes \underline{e}_{10} + \frac{1}{\cos\left(\frac{\beta}{2}\right)} \cdot \cos\left(\frac{\beta}{2} - \frac{\gamma}{2}\right) \underline{e}_{20} \otimes \underline{e}_{20} \tag{4.1}$$

$$\underline{\underline{C}} = \underline{\underline{F}}^T \underline{\underline{F}} = \left(\frac{\sin\left(\frac{\beta - \gamma}{2}\right)}{\sin\left(\frac{\beta}{2}\right)} \right)^2 \underline{e}_{10} \otimes \underline{e}_{10} + \left(\frac{\cos\left(\frac{\beta - \gamma}{2}\right)}{\cos\left(\frac{\beta}{2}\right)} \right)^2 \underline{e}_{20} \otimes \underline{e}_{20} \tag{4.2}$$

where $\underline{X}$ and $\underline{x}$ are the position of a material particle in the referential configuration and the current configuration, respectively. β is the braiding angle, $\gamma/2$ is the shear angle. $(\underline{e}_{10}, \underline{e}_{20})$ are the global coordinate systems.

The tubular fabric used in this chapter is a non-orthogonal fabric with a braiding angle of 55°, and its shear invariant is expressed as:

$$I_{sh} = \frac{I_{412}}{\sqrt{I_{41} I_{42}}} - \underline{M}_1 \cdot \underline{M}_2 \tag{4.3}$$

where $I_{41} = \underline{\underline{C}} : \underline{\underline{M}}_{11}$, $I_{42} = \underline{\underline{C}} : \underline{\underline{M}}_{22}$, $I_{412} = \underline{\underline{C}} : \underline{\underline{M}}_{12}$. I_{4i} are the mixed invariants. $\underline{\underline{M}}_{ij}$ are the structural tensors.

According to Eq. 3.20 in Chapter III, the second Kirchhoff shear stress tensor is expressed as:

$$\underline{\underline{S}}_{sh} = 2\frac{\partial w_{sh}}{\partial \underline{\underline{C}}} = 2 \cdot \frac{\partial w_{sh}}{\partial I_{sh}} \cdot \frac{\partial I_{sh}}{\partial \underline{\underline{C}}} \tag{4.4}$$

where w_{sh} is the shear strain energy, $\underline{\underline{C}}$ is the right Cauchy-Green strain tensor, I_{sh} is the in-plane shear invariant.

According to Eq. 3.33 ($w_{sh} = \sum_{i=1}^{n} k_i \left(I_{sh}\right)^{2i}$) in Chapter III, the derivative with respect to the shear invariants:

$$\frac{\partial w_{sh}}{\partial I_{sh}} = \sum_{i=1}^{n} 2i \cdot k_i \cdot \left(I_{sh}\right)^{2i-1} \tag{4.5}$$

where $k_i (i = 1, 2, ...)$ are the shear coefficients of the strain energy. They are determined by experiment.

Eq. 4.3 gives the relationship between I_{sh} and $\underline{\underline{C}}$. And then, the derivative of the shear invariant concerning $\underline{\underline{C}}$ can be expressed as:

$$\frac{\partial I_{sh}}{\partial \underline{\underline{C}}} = \frac{1}{2\sqrt{I_{41}I_{42}}}\left(\underline{\underline{M}}_{12} + \underline{\underline{M}}_{21}\right) - \frac{1}{2}\frac{I_{sh1}}{I_{41}}\underline{\underline{M}}_{11} - \frac{1}{2}\frac{I_{sh1}}{I_{42}}\underline{\underline{M}}_{22} \tag{4.6}$$

where $I_{sh1} = \dfrac{I_{412}}{\sqrt{I_{41}I_{42}}}$.

Considering that the shear deformation of fabric depends on the coordinates of the yarn, the coordinates of Eq. (4.6) are expressed as:

$$\frac{\partial I_{sh}}{\partial \underline{\underline{C}}} = \begin{pmatrix} -\sin^2\left(\dfrac{\beta}{2}\right) & 0 \\ 0 & \cos^2\left(\dfrac{\beta}{2}\right) \end{pmatrix} - \begin{pmatrix} \sin^2\left(\dfrac{\beta}{2}\right) & 0 \\ 0 & \cos^2\left(\dfrac{\beta}{2}\right) \end{pmatrix} \cdot I_{sh1} \tag{4.7}$$

The diagonal stress components in the different shear zones of the specimen are given by:

$$\begin{cases} S_{11}(\gamma_i) = -2 \cdot \sin^2\left(\dfrac{\beta}{2}\right) \cdot (1 + I_{sh1}) \cdot \sum_{i=1}^{n} 2i \cdot k_i \cdot \left(I_{sh}\right)^{2i-1} \\ S_{22}(\gamma_i) = 2 \cdot \cos^2\left(\dfrac{\beta}{2}\right) \cdot (1 - I_{sh1}) \cdot \sum_{i=1}^{n} 2i \cdot k_i \cdot \left(I_{sh}\right)^{2i-1} \end{cases} \tag{4.8}$$

Considering that the tubular fabric first undergoes pure shear deformation under axial tensile load, the external power generated by the machine force (F) is the sum of the internal power generated by the shear forces in each shear zone.

$$F\dot{u}(t) = \frac{1}{2}\int_{\Omega_0} \underline{\underline{S}} : \dot{\underline{\underline{C}}}(t) dV_0 \tag{4.9}$$

where F is the tensile load, u is the tensile displacement, V_0 is the volume of fabric in the initial state.

According to Eq. 4.2, the derivative of $\underline{\underline{C}}$ with respect to time is given by:

$$\dot{\underline{\underline{C}}}(t) = \frac{1}{2} \cdot \dot{\gamma}(t) \cdot \sin\left(\beta - \gamma\right) \left(\frac{-1}{\sin^2\left(\dfrac{\beta}{2}\right)} \underline{e}_{10} \otimes \underline{e}_{10} + \frac{1}{\cos^2\left(\dfrac{\beta}{2}\right)} \underline{e}_{20} \otimes \underline{e}_{20} \right) \tag{4.10}$$

From Eq. 4.8 and Eq. 4.10,

$$\underline{\underline{S}} : \dot{\underline{\underline{C}}}(t) = \frac{\dot{\gamma}_i(t)}{2} \sin\left(\beta - \gamma_i\right) \left(-\frac{S_{11}(\gamma_i)}{\sin^2(\frac{\beta}{2})} + \frac{S_{22}(\gamma_i)}{\cos^2(\frac{\beta}{2})} \right) \tag{4.11}$$

The shear angle of the tubular fabric is not uniform, and according to Eq. 2.17 in Chapter II, the shear angle in the i[th] shear zone can be expressed by:

$$\gamma_i = \beta - 2\arcsin\left[\left(\frac{4 \cdot (W - 2b_0)}{W(u+L)^2} \cdot z_i^{\,2} + \frac{2b_0}{W} \right) \cdot \sin\left(\frac{\beta}{2}\right) \right] \tag{4.12}$$

Integrating the energy of the initial effective surfaces of the fabric, the relations between the tensile load and components of the shear tensor can be obtained:

$$F = 2 \cdot \sum_{i=1}^{N} \frac{4(W - 2b_0) \cdot \sin\left(\frac{\beta}{2}\right) \cdot z_i^{\,2}}{W(u+L)^3 \sqrt{1 - \left[\left(\frac{4 \cdot (W - 2b_0)}{W(u+L)^2} \cdot z_i^{\,2} + \frac{2b_0}{W} \right) \cdot \sin\left(\frac{\beta}{2}\right) \right]^2}} \cdot h \cdot \left(\sin\left(\beta - \gamma_i\right) \cdot A_i \left(-\frac{S_{11}(\gamma_i)}{\sin^2(\frac{\beta}{2})} + \frac{S_{22}(\gamma_i)}{\cos^2(\frac{\beta}{2})} \right) \right) \tag{4.13}$$

where u is the tensile displacement, b_0 presents the minimum radius of the deformed tubular fabric, A_i is the initial surface area of different shear zones, h is the thickness of the fabric, N is the number of shear zones of the fabric, and L and W symbolize the original length and diameter of the fabric, respectively.

Eq. 4.13 gives the relationship between the tensile load and the second Kirchhoff shear stress tensor, and the parameters (k_i) of the shear strain energy are obtained using this relation. Chapter II has demonstrated that tubular braided fabrics under the axial tensile load undergo radial shrinkage resulting in a non-uniform distribution of the shear angle in the fabric. Meanwhile, the shear theory presented in Chapter II was verified by four different partitions (zone A, zone B, zone C and zone D) in the axial direction of the fabric, as shown in Fig. 2.15. Therefore, in the study of this chapter, N=4 in Eq. 4.13. The numerical solution for nonlinear minimization can be obtained via Levenberg–Marquardt algorithm. The shear coefficients of the tubular fabric are identified by using the Levenberg–Marquardt algorithm to interpolate the force-displacement data of the fabric under the action of axial tension, as shown in Fig. 4.3.

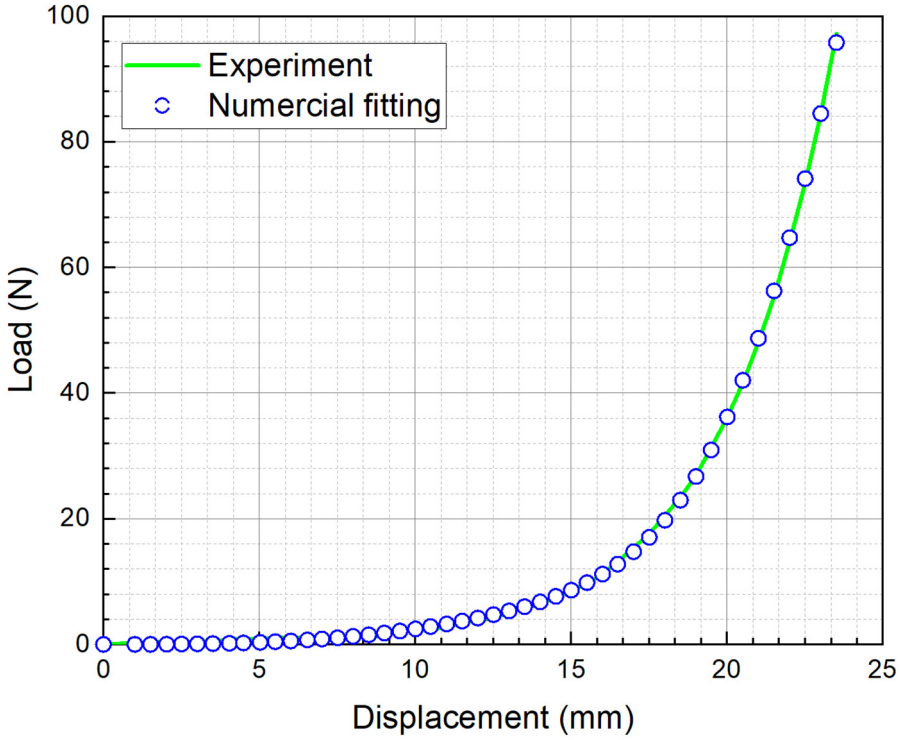

Fig. 4.3 Identification of shear parameters for flax/PA12 of tubular braided fabrics.

Table 4.1 The shear coefficients of the strain energy

Fabric types	Shear Coefficients (J/mm^2)
Flax/PA12	$k_1=0.1608,\ k_2=-0.1823,\ k_3=0.4335$

4.3 Numerical simulation settings

4.3.1 Simulation of uniaxial tensile test for tubular braided fabrics

The hyperelastic constitutive model proposed in Chapter III was used to simulate the uniaxial tensile process of tubular braided fabric. The fabric initially has a hollow cylindrical shape, and the finite element model is established based on the experimental specimen, as shown in Fig. 4.4. The dimensions of the simulation model are consistent with the experiments (diameter is 50 mm, height is 40 mm, thickness is 2.06 mm). It is worth noting that the direction of yarns is crucial in the numerical simulation of tubular fabric as they reflect the fabric's deformation behavior (Eq. 4.1). The deformation gradient of the fabric at different stages of stretching is achieved by tracking the

coordinates of yarns, which depend on the relation between the local and global coordinate systems. Considering the special structure of the tubular fabric, the orientation of the yarns constituting the fabric is not unique, which makes the characterization of the yarns difficult. Interestingly, the distribution of these yarns also seems to exhibit a certain law. All the interlaced yarns in the same group of axial columns in the fabric have consistent directions, as shown in Fig. 4.4 (b). Therefore, in this study, the yarns of the tubular fabric are divided into different groups according to the axial columns in which they are located by using the grouping method, and the yarns of all units located in the same group are set in the same direction. By utilizing this method, the fabric is divided into different columns and assigned different orientations. So, all intersecting yarn orientations in the fabric are completely described.

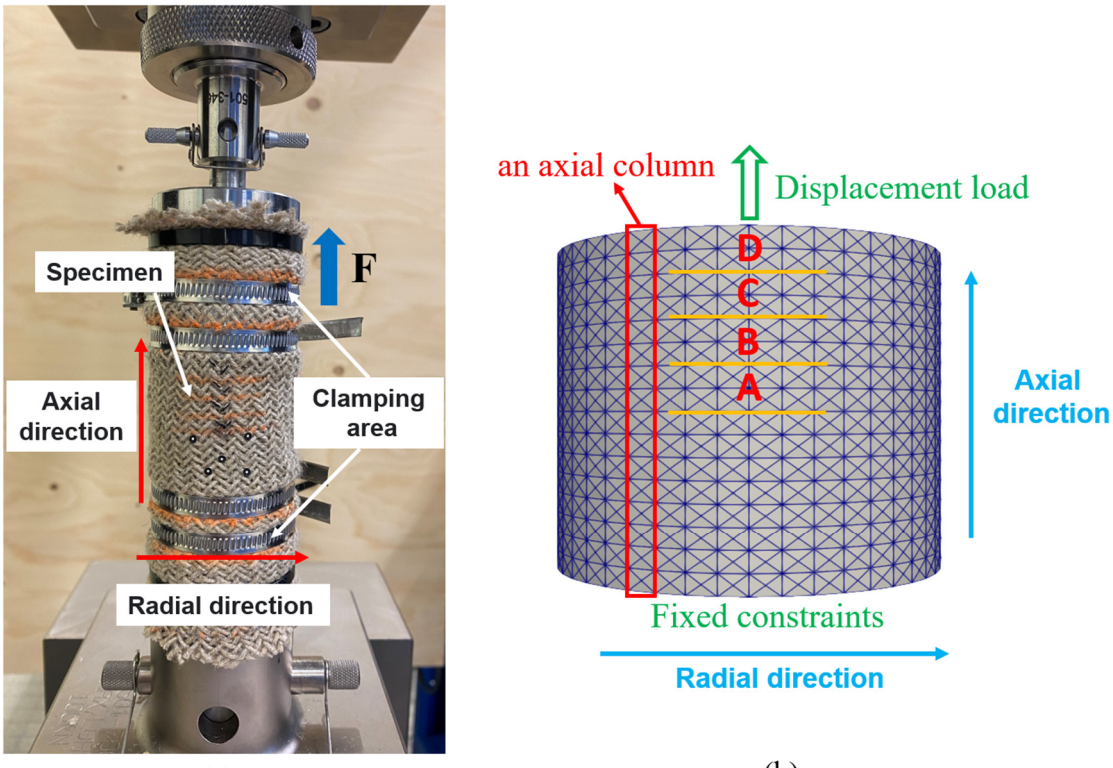

(a) (b)

Fig. 4.4 Tensile test of tubular braided fabric, (a) experimental setup and (b) finite element model of the fabric.

The simulation analysis of the fabric under uniaxial tensile load is implemented using the C++ code developed by Innovamics mentioned in Chapter III. According to the experimental setup, a fixed constraint is applied to the bottom of the fabric, while a displacement load is applied to the top of the fabric along its axial direction. The material properties of the fabric are chosen to be hyperelastic and the triangular membrane elements are used and the element size is set to 2.5 mm. The uniaxial tensile test of the tubular fabric is conducted at room temperature and the profile of the fabric under different tensile deformation conditions can be obtained from the tensile test. In order to compare with the experimental results in Chapter II, the profile of the fabric at 25%, 50% and 75% deformation were also selected for the simulation analysis, and the comparison results are shown in Fig. 4.5. Meanwhile, the errors of the experimental and simulated values of the fabric profiles under different tensile deformations were calculated, the corresponding errors under 25%, 50% and 75% tensile deformations were 14.7%, 10.2% and 10.8%, respectively. The errors are in a reasonable range and validate the effectiveness of the hyperelastic model and simulation methods.

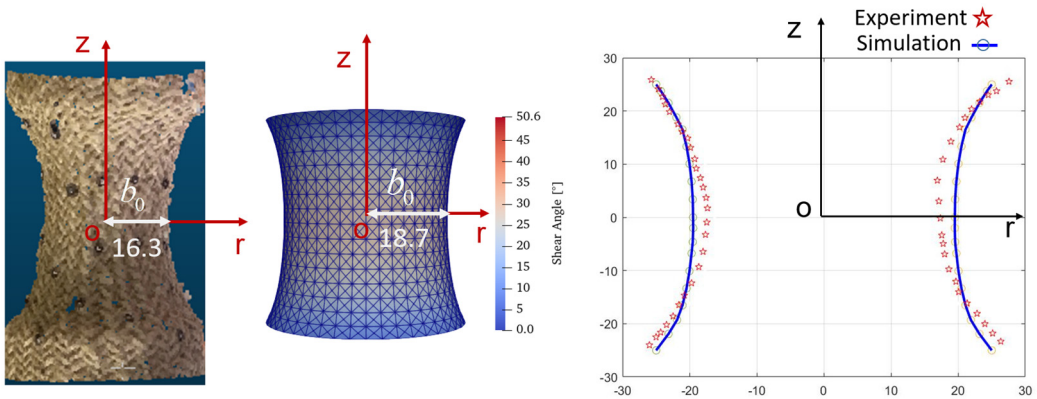

(a)

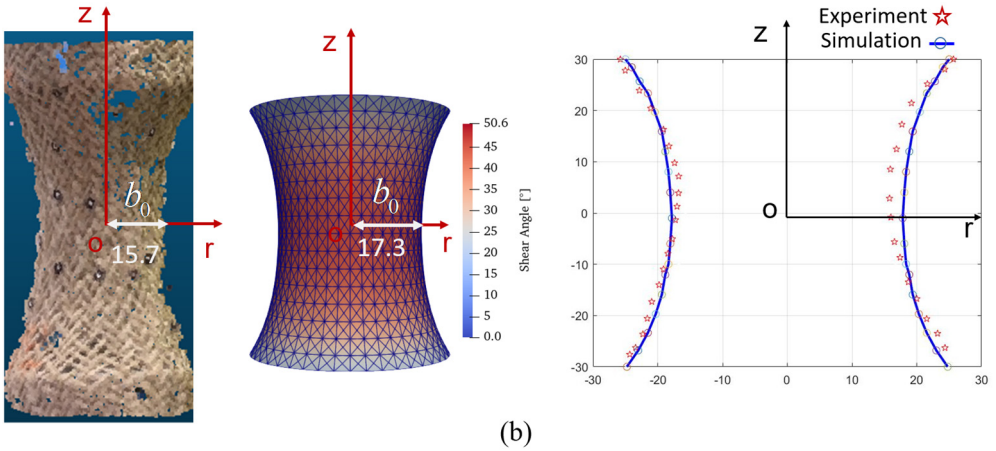

(b)

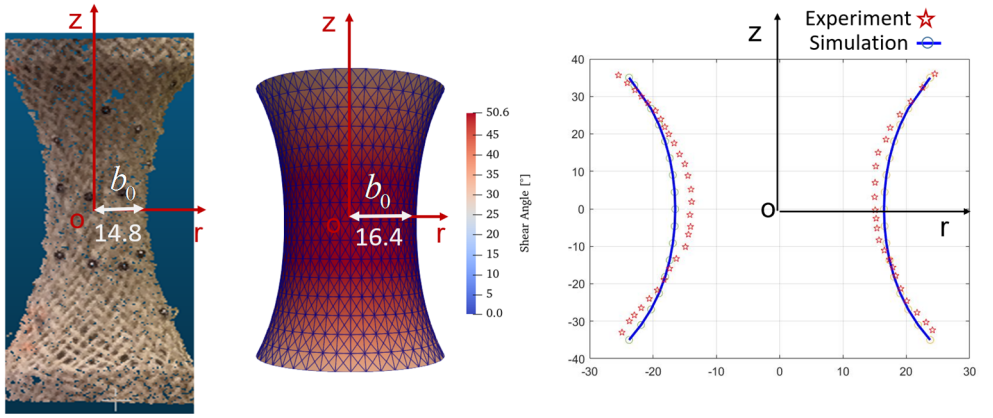

(c)

Fig. 4.5 Comparison of experimental and simulated profiles of tubular fabrics at different tensile deformations, (a) 25% tensile deformation, (b) 50% tensile deformation and (c) 75% tensile deformation.

As described in Section 2.3 of Chapter II, the mechanical behavior of the fabric in uniaxial tensile tests is divided into three stages: pure shear, a combination of shear and yarn extension, and pure yarn extension. The theoretical model of the shear angle described in Eq. 4.12 has been validated and it can effectively describe the shear angle variation of the fabric in the pure shear stage. Therefore, the shear parameters of the fabric obtained by using Eq. 4.3 (shown in Table 4.1) are also applicable to the simulation of the pure shear stage. In the experiments to analyze the shear behavior of the fabric, four different zones (zone A, zone B, zone C, zone D) were selected along the axial direction of the fabric in Chapter II, so the analysis of the simulation results was also divided into four corresponding zones (zone A, zone B, zone C, zone D). In order to verify the accuracy of the simulation analysis, the in-plane shear angle was

measured for shear zones from A to D (Fig. 4.6). The values were compared to the shear angle calculated by the simulation and were found to be in fairly good agreement.

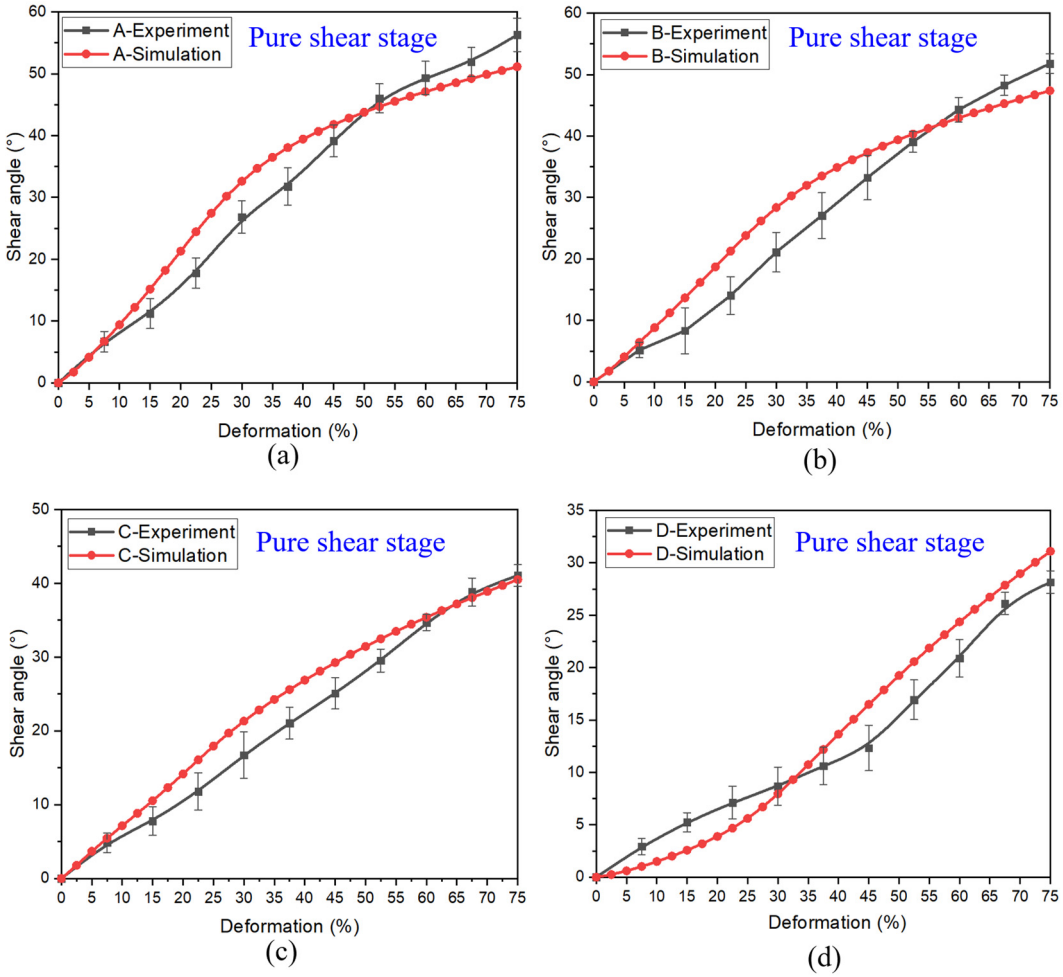

Fig. 4.6 Comparison of experimental and simulation results in different shear zones of tubular fabrics.

4.3.2 Simulation of forming process about the tubular fabrics

(1) The details of the simulation method

Consistent with the simulation of the uniaxial tensile test of the tubular fabric, the simulation of the forming process still uses the nonlinear explicit finite element code provided by Innovamics. The finite element modeling of the forming setup includes the tubular specimen and the different shapes of forming molds. The forming specimen will be deformed under the action of the tensile loads. The modeling of a tubular braided specimen is presented in Fig. 4.7. The specimen model is meshed using the triangular

MEMBRANE elements, and the length of the right-angle side of the triangular element is 2.5 mm. As the forming tools, the deformation of the molds is much smaller than that of the test samples. Therefore, the forming tools are considered as rigid bodies without deformation in the simulation process. Each part will be meshed by the triangle rigid body element and the mesh size is 3 mm. Furthermore, the coefficient of friction between the fabric and the model was set to 0.2.

The forming simulation presented in this chapter includes two types of forming: cylinder and tetrahedron. For these two models, they are both centrally symmetrical shapes. In order to save time and improve simulation efficiency, only a quarter of the model is created and the symmetrical boundary conditions are set in the simulation. Then, the entire model can be obtained by using the reflect function of Paraview software (shown in Fig. 4.7).

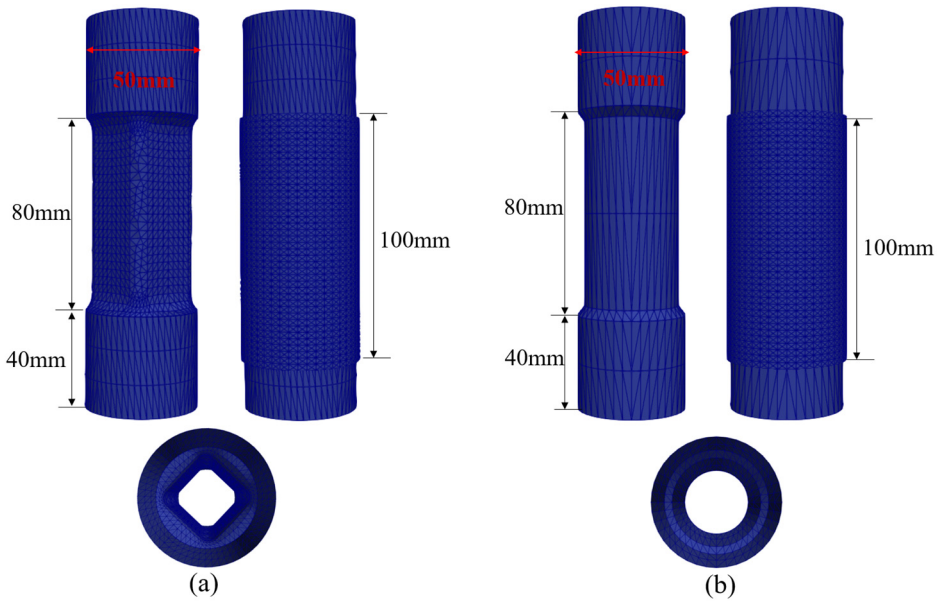

Fig. 4.7 Forming of tubular braided fabrics on the different molds, (a) tetrahedron and (b) cylinder.

(2) Simulation analysis of the preforming process with tetrahedral

According to the above-mentioned, the tubular braided fabric was stretched and preformed on a tetrahedral mold, the mold is shown in Fig. 4.8 (a). The preforming

experimental results of the fabric under the tensile displacement of 25 mm are shown in Fig. 4.8 (b). From the experimental results, it can be seen that the tubular fabric is finally attached to the mold to form the expected shape. This indicates that under the action of tensile load, the fabric undergoes shear behavior, resulting in a certain degree of shrinkage in the radial direction of the fabric. When the fabric contacts the mold, the radial shrinkage weakens. Interestingly, compared with the preforming process of 2D fabrics, the defects in preforming process of 3D tubular fabrics are more related to yarn slippage rather than wrinkles. Using the shear parameters of the tubular fabric obtained in Section 3.2.3 and the improved hyperelastic constitutive model in Chapter III, the preforming process of the tubular fabric is simulated and analyzed. The boundary conditions of the simulation are set according to the tensile test. The simulation result of the tetrahedron is shown in Fig. 4.8 (c). The simulation results and the experimental results show a good consistency in the final formed shape of the fabric, and the fabric has uneven shearing. According to the degree of shearing, the fabric is divided into 7 different zones, which are closely related to the shape of the mold.

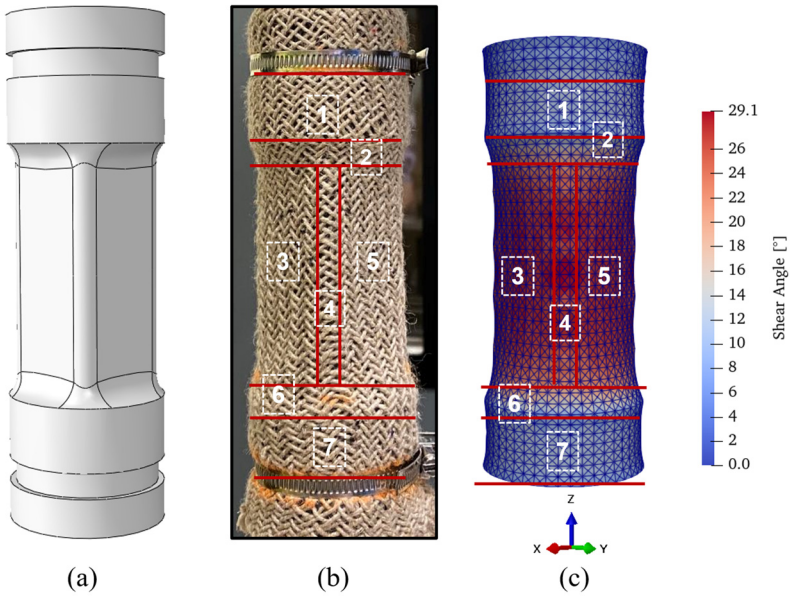

(a) (b) (c)

Fig. 4.8 Preforming of tubular braided fabrics on tetrahedral mold, (a) preforming mold, (b) experimental result and (c) simulation result.

In order to analyze more intuitively the mechanical behavior of the fabrics during the tensile process and the shape changes of preforming, it is difficult to obtain the shapes of the fabric in the entire forming process from experiments. Therefore, this section is investigated by using the simulation method. In the simulation process, tubular fabrics under different tensile displacements of 0, 10, 20 and 25 mm were selected for investigation. The slide function of the post-processing software Paraview was utilized to cut along the deformed part of the tubular fabric to obtain the shape of the fabric under different tensile displacements, as shown in Fig. 4.9. Through comparison, it was found that as the stretching displacement increased, the hollow part of the fabric gradually changed from the initial circular shape to a quadrilateral shape until the fabric adhered to the mold and became a tetrahedron shape. With a further increase in tensile, the fabric became more conformal to the mold, resulting in the desired preformed shape.

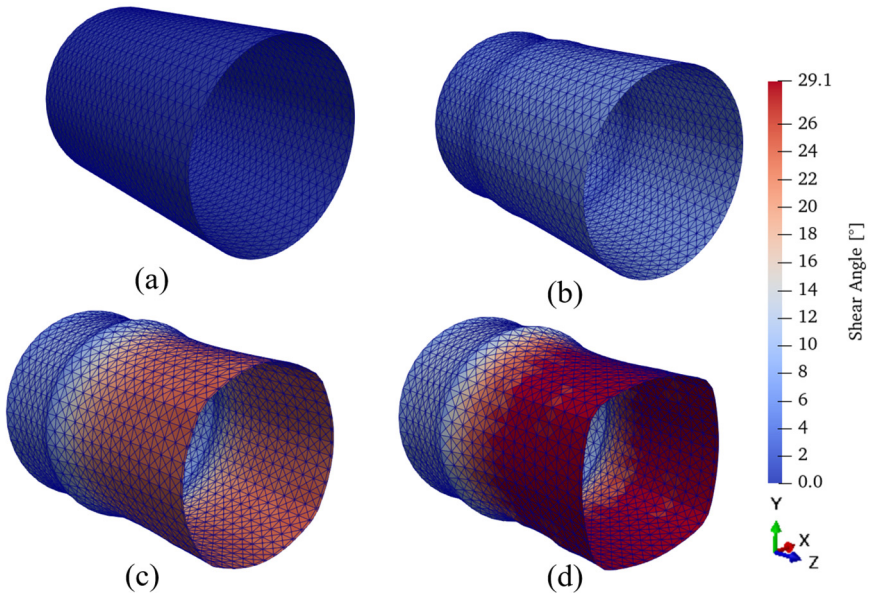

Fig. 4.9 Evolution of preformed shapes of tubular braided fabrics under different tensile displacements, (a) tensile displacement of 0 mm, (b) tensile displacement of 10 mm, (c) tensile displacement of 20 mm and (d) tensile displacement of 25 mm.

The achievement of preforming tubular braided fabrics mainly relies on the shear interaction between yarns, which determines the shape and mechanical properties of the preforms during the forming process. Therefore, accurate prediction of the shear angle

distribution plays an important role in fabric forming optimization, which is also one of the indicators to verify the accuracy of the simulation method. Considering that the tubular fabric is symmetrical, what is illustrated in Fig. 4.8 only shows half of the fabric. After preforming the tubular fabric on the tetrahedron mold, it is divided into 7 zones based on the distribution of shear angles. The optical measurement methods can be used to obtain the shear angle in any zone of the fabric. The shear angle of each zone is calculated and the average value is taken as the final shear angle of this zone. At the same time, the distribution of shear angle obtained by simulation was used to compare with the experimental results, as shown in Fig. 4.10, the maximum error in shear angle was 10.4%. The maximum shear angle of the fabric occurs on the four faces of the mold (zone 3 and zone 5). Therefore, the validity and accuracy of the numerical prediction on the shear angle were confirmed from the comparison.

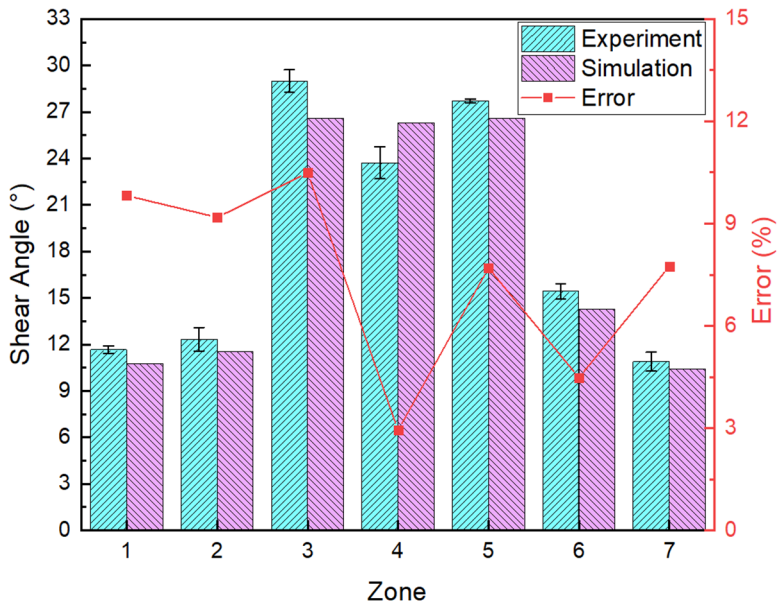

Fig. 4.10 Comparison of in-plane shears between experiment and numerical simulation approaches in 7 different zones.

Since the maximum shear angle of the fabric is in zone 3 and zone 5, the yarn in this region is stretched earlier than in other regions, and the yarn elongation of the fabric during stretching can be obtained through the marking points on the fabric, as

mentioned in Section 4.2.2. At the same time, the simulation results of fabrics with the same tensile displacement are selected for comparison, as shown in Fig. 4.11. The yarn elongation during the test is in good agreement with the simulation results, which further confirms the validity of the simulation. It is worth noting that Ref. [167] has given that Flax would be broken when the elongation of a single yarn reached about 3%. Therefore, the comparative results of the test and simulation in this part are selected before the Flax is broken.

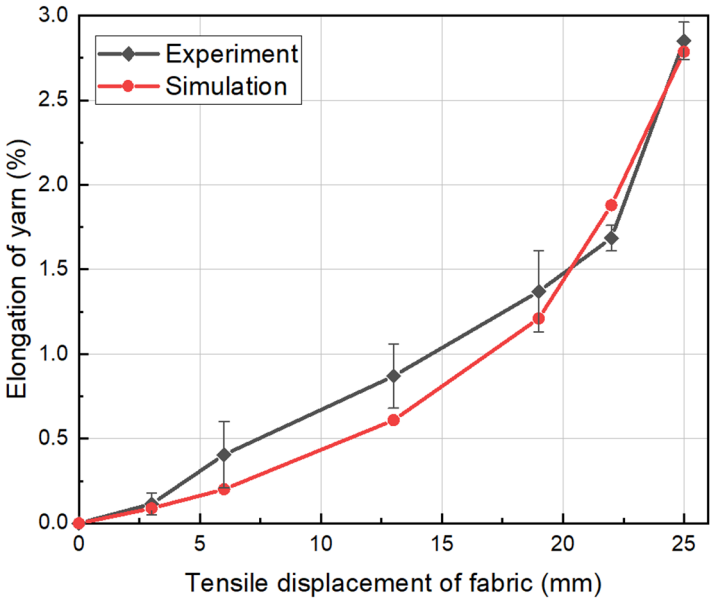

Fig. 4.11 Comparison of experimental and numerical simulation of yarn elongation in zone 3.

(3) Simulation analysis of the preforming process with cylinder

The preforming process of the tubular braided fabric on the cylindrical mold was achieved by the same tensile test as the tetrahedral preforming. The cylindrical mold is shown in Fig. 4.12 (a), and Fig. 4.12 (b) shows the experimental results of the fabric with a tensile displacement of 25 mm. From the figures, it can be found that the tubular fabric was finally molded into the expected shape under the tensile load, and the preformed fabric presented five zones depending on the shear angle. Meanwhile, the preforming process of the tubular fabric is numerically simulated using the hyperelastic

model, and the simulation results are shown in Fig. 4.12 (c). The figure displays the shear angle distribution of the fabric and the the partition of the shear angle is consistent with the experiment.

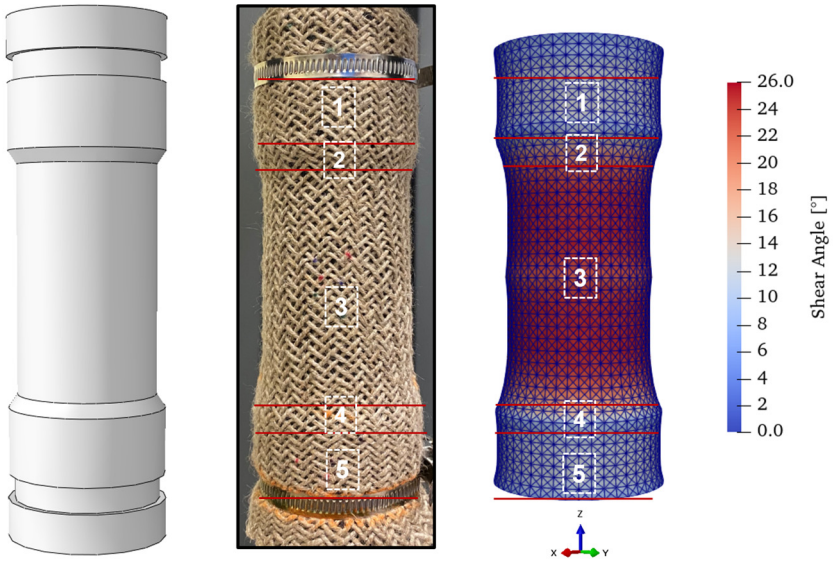

Fig. 4.12 Preforming of tubular braided fabrics on cylinder mold, (a) mold, (b) experimental result and (c) simulation result.

Forming of tetrahedra of tubular braided fabrics has been investigated in terms of shape changes of fabrics under different tensile displacements. The same method was used to study the forming of the fabric on a cylindrical mold. The shape changes of the tubular fabric under different tensile displacements are shown in Fig. 4.13. From the analysis of the figure, it can be observed that the fabric exhibits more noticeable radial shrinkage behavior under the action of tensile load. The hollow part of the fabric gradually decreases and conforms to the mold as the tensile displacement increases. When the fabric is in complete contact with the mold, the radial shrinkage ends and the fabric takes on a cylindrical shape.

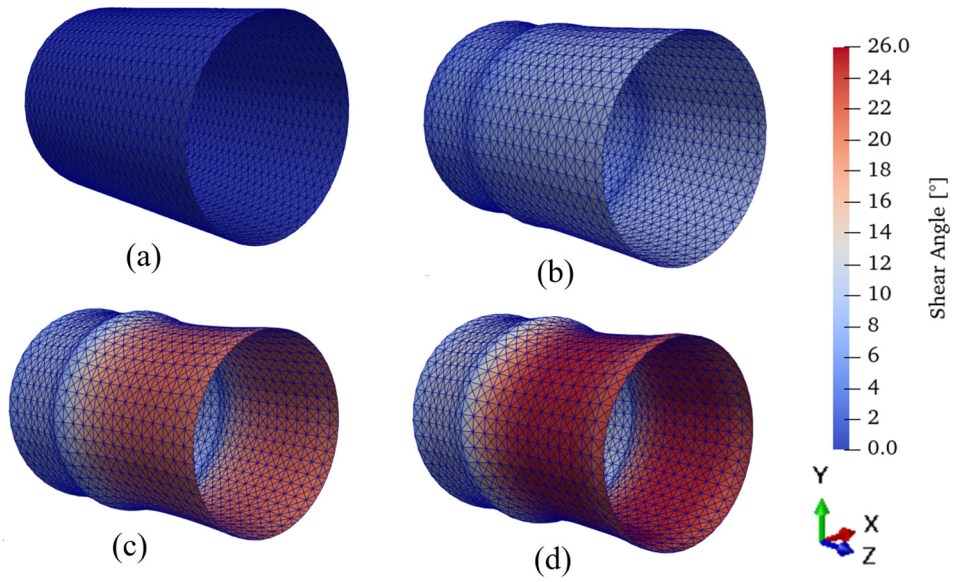

Fig. 4.13 Evolution of preformed shapes of tubular braided fabrics under different tensile displacements, (a) tensile displacement of 0 mm, (b) tensile displacement of 10 mm, (c) tensile displacement of 20 mm and (d) tensile displacement of 25 mm.

Fig. 4.12 displays the shear angle distribution of the fabric after forming on a cylindrical mold, which is mainly divided into five different shear zones. Based on the experimental results, the average shear angles of the fabric in each region were calculated and compared with the simulation results, as shown in Fig. 4.14. In the comparison of the shear angles of the five different zones, the largest error was found in zone 1, with an average value of 12.16° for the test and 11.36° for the simulation, resulting in a maximum error of 6.6%. In addition, the maximum shear angle of the fabric appeared in the middle part of the cylinder (zone 3). Furthermore, the elongation of a single yarn in zone 3 was measured and compared with the simulation results, showing good consistency (Fig. 4.15). It is confirmed that the use of a non-orthogonal hyperelastic model to simulate the preforming of tubular braids is reasonable.

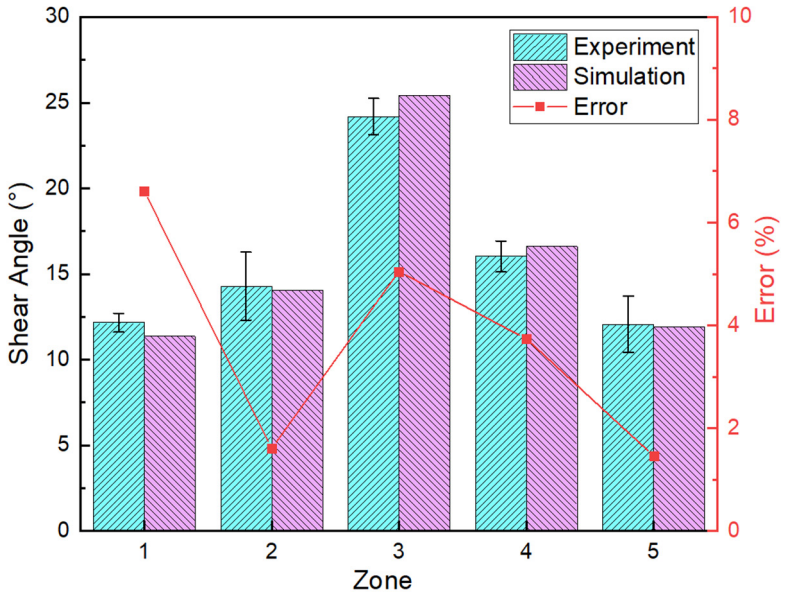

Fig. 4.14 Comparison of in-plane shears between experiment and numerical simulation approaches in 5 different zones.

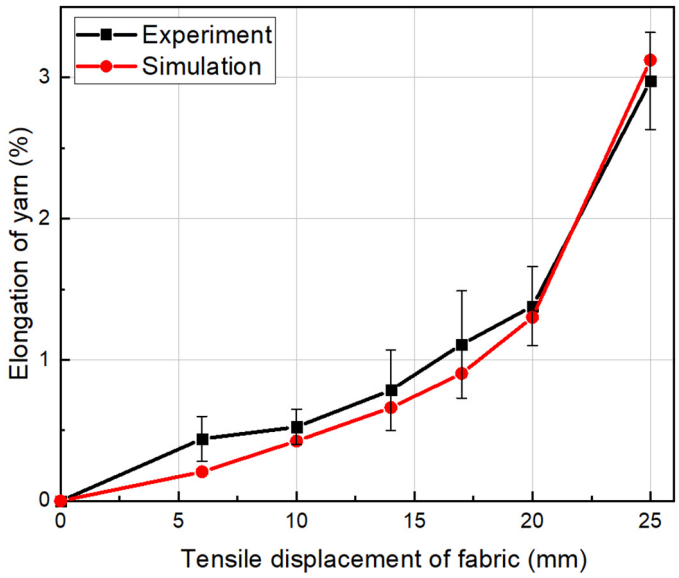

Fig. 4.15 Comparison of experimental and numerical simulation of yarn elongation in zone 3.

(4) Forming of tubular fabrics under variation of tensile direction

The simulation analysis of uniaxial tensile tests and preforming tests on tubular fabrics has demonstrated the effectiveness of the hyperelastic model. On this basis, the influence of changes in the tensile direction on the mechanical behavior of the fabric is considered. The forming of fabrics in different tensile directions is analyzed by using

numerical simulation, and the deformation behaviors of tubular fabrics on L-shaped pipes with the angles between the tensile direction and the horizontal direction of 135° and 165° are investigated respectively. The finite element model is shown in Fig. 4.16.

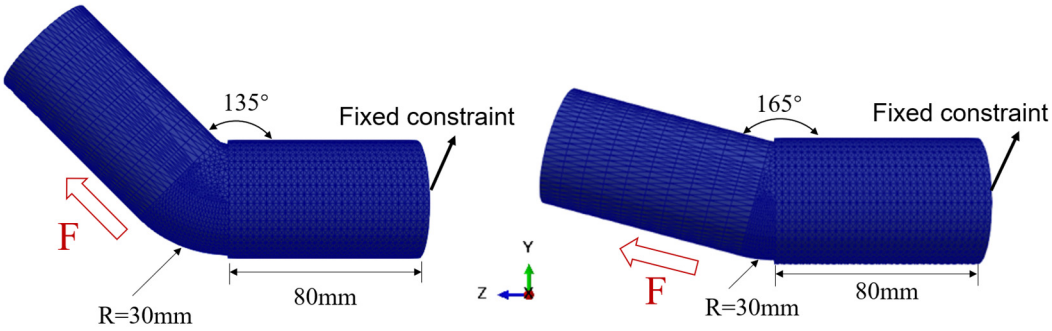

Fig. 4.16 Finite element model under different tensile directions.

During the simulation process of fabric forming, one end of the tubular fabric is fixed on the mold, and the other end is applied with a load along the bending direction of the mold. Under the action of the load, the fabric takes on a shape consistent with the mold, as shown in Fig. 4.17. The simulation results reveal different shear angle distributions on the inside and outside of the fabric, and the tensile direction also has an impact on the shear angles.

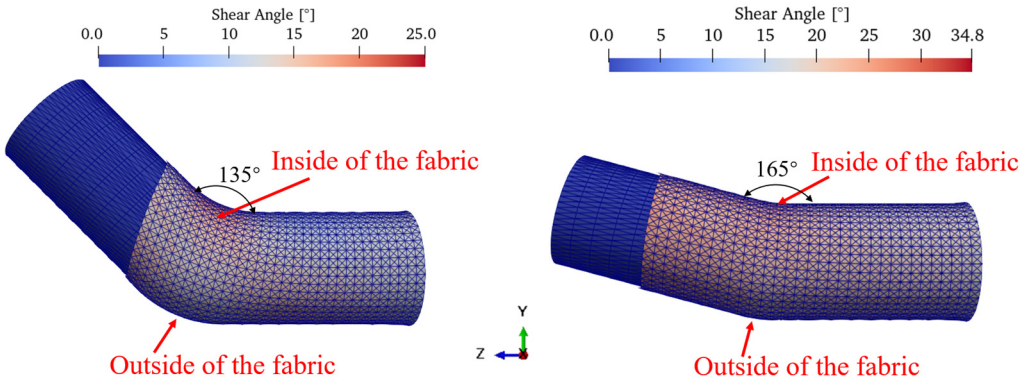

Fig. 4.17 The distribution of shear angles under different tensile directions.

To further investigate the mechanical behavior of the tubular fabrics, the shear angles of the inside and outside of the fabrics as well as the elongation of a single yarn are

compared, as shown in Fig. 4.18. Under the same mold, the shear angle on the inside of the fabric is greater than that on the outside, and the elongation of yarns on the inside is smaller than that on the outside. This is because, during the bending of the fabric, the outer-side yarns experience tensile stress, leading to yarn elongation, and the shearing effect between yarns is reduced. On the other hand, the inner-side yarns are subjected to compressive stress, reducing their elongation, and the shearing behavior of the yarns is more pronounced on the inner side compared to the outer side. In addition, the tensile direction of the load affects the degree of fabric bending. The shear angle of the inner and outer parts of the fabric increases with the increase of the mold angle. When the mold angle is larger, the fabric experiences less bending, and the pure shearing process of the fabric is less affected by the tensile direction, allowing for more shearing space.

Comparing the elongation of yarns under different tensile directions, it is observed that the elongation of yarns on the inside of the fabric increases with an increase in the mold angle, and the elongation of yarns on the outside of the fabric decreases with the increase of the mold angle. This is due to the fact that the fabric bends less on the mold at 165°, and the outer tensile and inner compressive stresses on the fabric are smaller than those on the mold at 135°.

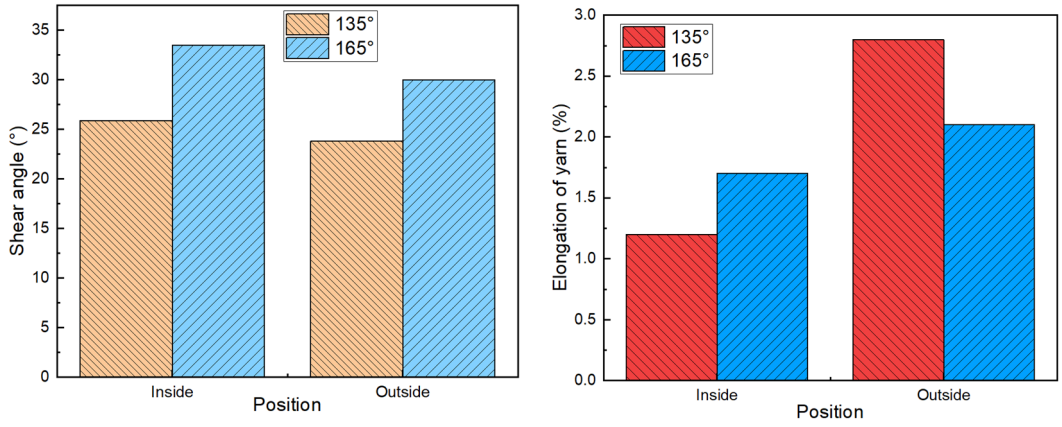

(a) (b)

Fig. 4.18 Comparison of results for tubular fabrics in different tensile directions, (a) shear angle and (b) elongation of the yarn.

4.4 Conclusion of Chapter IV

In this chapter, the mechanical behavior of tubular braided fabrics under the uniaxial tensile test proposed in Chapter II and the improved non-orthogonal hyperelastic constitutive model in Chapter III are used to simulate the preforming process of tubular fabrics. The theoretical relationship between the fabric load and the second Piola-Kirchhoff stress tensor was established, and the strain energy coefficients used to characterize the shear deformation of the fabric were obtained by fitting the force-displacement curves of the fabric using this theoretical relationship. To validate the effectiveness of the shear parameters and the hyperelastic model, the uniaxial tensile process of tubular fabrics was simulated in this chapter. It was found that the fabric contracted in its radial direction under the axial tensile load, which was consistent with the experimental results. Meanwhile, the experimental and simulated results of the fabric profile at different tensile displacements were compared, and the maximum radial shrinkage error was 14.7%. Considering the non-uniform shear of the fabric, four different zones of the fabric in the axial direction were investigated in Chapter II. In this chapter, the experimental and simulated shear angles in these four zones are compared, and the better agreement proves the validity of the hyperelastic model for characterizing the shear behavior of tubular braided fabrics.

Secondly, this chapter investigates the deformability of fabrics on different-shaped molds by studying the radial contraction mechanical behavior of tubular fabrics under tensile load. Axial tensile tests were conducted on the fabrics to obtain the results of fabric preforming on tetrahedral and cylindrical molds. It was found that the shear angle distribution of the fabrics after preforming was non-uniform. Additionally, when the fabric preforming process was simulated by using the hyperelastic model and compared with the experimental results, the shear angles were in good agreement. This is conducive to further research on various factors affecting the preforming results of the fabric. Finally, the deformation behavior of tubular fabrics under different tensile directions was also investigated. It was found that the shear behavior of the inner side

of the fabric was more pronounced than that of the outer side during the tensile process. Meanwhile, the tensile direction affected the bending degree of the fabric, resulting in the shear behavior of the fabrics decreasing with the increase of the degree of bending.

V. GENERAL CONCLUSION

Résumé en français

Cette thèse a étudié les propriétés mécaniques et les déformabilités des renforts textiles au cours du préformage. En se basant sur l'analyse cinématique, la performance en cisaillement des renforts tressés bidimensionnels lors du Bias-extension test a été étudiée. L'étude a révélé que le comportement en cisaillement des tresses plates est asymétrique dans les directions transversale et axiale. Le comportement mécanique des renforts tressés avec la structure 3D-tubulaires a été étudié en utilisant des tests de traction uniaxiale. Sous une charge axiale, le renfort tubulaire présente une contraction radiale, et sa réponse mécanique est divisée en trois parties : cisaillement pur, combinaison de cisaillement et d'allongement des fils, et allongement pur des fils. Lors de l'étude de la déformabilité pendant la mise en forme du renfort tressé tubulaire, la déformation dans la phase de cisaillement pur est essentielle. Un modèle analytique est établi pour décrire le comportement de cisaillement pur sous tension axiale. L'efficacité de ce modèle a été vérifiée en comparant avec des résultats expérimentaux. L'effet de la température sur les propriétés thermomécaniques des tresses tubulaires avec des fils comélés thermoplastiques a été étudié. Les résultats montrent que la rigidité au cisaillement des tresses est la plus élevée à température ambiante pour la même vitesse de traction. À mesure que la température augmente, le changement de l'état des fils diminue la rigidité au cisaillement. A une même température, la rigidité au cisaillement augmente avec l'augmentation de la vitesse de traction.

La réponse mécanique des tresses plates et tubulaires sous charge de traction a également été simulée à l'aide d'un modèle constitutif hyperélastique amélioré. Les invariants de traction et de cisaillement sont utilisés pour décrire les modes de déformation correspondants des tresses lors de la mise en forme. La validité de la simulation numérique a été vérifiée par des Bias-extension tests et des tests d'emboutissage hémisphérique sur les tissus tressés non orthogonaux. Les résultats indiquent que tant le comportement en cisaillement que le préformage des tresses présentent une asymétrie. En particulier, les invariants de cisaillement proposés dans le chapitre III peuvent être appliqués à un renfort textile biaxial avec un angle arbitraire et non pas limité au 90°.

Les déformabilités des tresses tubulaires ont été étudiées à l'aide d'un modèle hyperélastique amélioré. Des tests mécaniques sur les tresses tubulaires ont été réalisés pour simuler les caractéristiques de contraction radiale et l'inhomogénéité de

cisaillement. Les profils de déformation des tresses ont été comparés aux résultats des tests, ce qui a confirmé la rationalité de l'utilisation du modèle hyperélastique pour simuler la déformation des tresses tubulaires. De plus, la contraction radiale des tresses tubulaires sous charge de traction favorise la mise en forme avec des différentes moules (cylindres, tétraèdres, en forme de L), cela dépend l'effet de cisaillement.

5.1 Conclusion

The present study aims to analyze and simulate the forming process of 2D and 3D tubular biaxial braided composite reinforcements. The mechanical properties and deformation behavior of textile fabrics were investigated. The preforming process is typically the first step in manufacturing complex-shaped composites. During the preforming, various forming defects can easily occur in the preform due to the influence of many factors, which can impact the final forming quality and mechanical performance of the composite component. Therefore, characterizing forming defects, studying deformation mechanisms and optimizing process parameters are of great significance for improving the forming quality of textile preforms. It can identify the suitable forming conditions for textile reinforcements to minimize the defects during the forming. At present, the research on textile-reinforced materials mainly relies on experimental methods. The diverse structures of textile reinforcements, varied manufacturing parameters and diverse preforming shapes increase the difficulty of experiments. Simulation methods, as an auxiliary approach, can conduct numerous parameter studies without repetitive experiments, thereby improving the research efficiency and saving the research time and cost. Therefore, this thesis employed a combination of experimental and simulation methods to investigate the preforming process of braided reinforcements.

The main achievements of the research are concluded as follows:

1) Based on the kinematic analysis, the shear performance of two-dimensional braided fabrics under the bias extension test was investigated. The study revealed that the shear performance of flat braided fabrics is asymmetric in the transverse and axial directions. The mechanical behavior of tubular braided fabrics was studied utilizing uniaxial tensile tests. Under axial loading, the tubular fabric was accompanied by radial shrinkage, and their mechanical responses were mainly divided into three parts: pure shear, the combination of shear and yarn's elongation, and yarn's elongation. When studying the forming deformation, the deformation in the pure shear stage is essential.

An analytical model is established to describe the pure shear behavior under axial tension. The effectiveness of the corresponding method was verified by comparing the experimental results of tubular fabrics. In addition, the effect of temperature on the mechanical properties of fabrics was also investigated. It was shown that the shear stiffness of fabrics was highest at room temperature for the same tensile speed. As temperature increases, the change of yarn state decreases the shear stiffness of fabrics. At the same temperature, fabric strength and shear stiffness increase with increasing tensile rate.

2) The mechanical response of flat braided fabrics under tensile load was simulated via an improved hyperelastic constitutive model. The model used the relation between invariant and strain energy to characterize the deformation modes of braided fabrics during the preforming process. The non-orthogonal structure of the fabric results in significant differences in strain energy under shear deformation compared to woven fabrics. Meanwhile, the relationship between the tensile load and the second Piola-Kirchhoff stress tensor was established to identify the shear strain energy coefficients. The validity of numerical simulations was verified through the bias-extension tests and hemispherical stamping tests on non-orthogonal braided fabrics. The results indicated that the shear behavior of the braided fabrics under the bias-extension test is asymmetric, and the fabrics have different in-plane shear angles in the transverse and axial directions. In addition, the shear angles in different sizes of fabric proved that the shear behavior of fabrics was influenced by the width of the yarn. In the simulated preforming process of braided fabrics, the fabric exhibited different shear deformations in the axial and transverse directions. The fabric has an obvious draw-in behavior in the axial direction. The maximum shear angle occurred in the transition region between the double dome curve surface and the flat area of the fabric. In particular, the shear invariants proposed in this study can be applied to braided fabrics with arbitrary angles and are not limited to woven fabrics.

3) The forming properties of tubular braided fabrics were also investigated using an improved non-orthogonal hyperelastic model. The coefficients of shear strain energy were obtained from the relationship between the tensile load and the shear stress tensor. From the simulation results of mechanical tests on tubular braided fabrics, the radial contraction under the axial tensile load was obtained, which was consistent with the experimental results. Meanwhile, the experimental and simulated results of the fabric profile at different tensile displacements were compared, which verified the effectiveness of the simulation. The mechanical tests in Chapter II confirmed the shear inhomogeneity of the fabric and investigated four different regions along the axial direction of the fabric. In this chapter, the simulation results of the shear angle in these four regions were compared with the experimental results and the results are in good agreement. The formability of tubular braids on different-shaped molds was investigated by studying the radial contraction mechanical behavior of fabrics under tensile load. The preforming results of the fabric on tetrahedral and cylindrical molds were also obtained through axial tensile tests, which depend on the radial shrinkage behavior of tubular fabrics. The fabrics exhibited different shear partitions after forming on different molds. By utilizing the hyperelastic model to simulate the fabric preforming process and comparing the simulation results with the experimental results, the shear angles of the different shear zones are in good agreement. This is conducive to further investigating various factors that influence the preforming results of the fabric.

5.2 Perspectives

With the expanding use of braided reinforcements in the manufacturing industry, the analysis of their mechanical properties is crucial. This thesis has studied the mechanical properties of flat braided fabrics and tubular braided fabrics, primarily employing experimental and simulation methods to study the fabric's mechanical behavior during the preforming process. Additionally, a preliminary exploration of the thermomechanical properties of tubular braided fabrics has been carried out. Based on

the research conclusions obtained in the thesis work, further research work can be done in the following items:

- The thermomechanical properties of tubular fabrics need to be simulated using finite element models. This includes the establishment of fabric constitutive models, validation of thermomechanical properties, and the prediction of thermoforming properties. It will provide a reference for the production of composite components.
- The deformation modes during the fabric preforming process are not only limited to tensile and shear. The tension of yarn generated by the outside bending of the fabric also needs to be analyzed. In subsequent research, experiments for characterizing the bending properties of braided fabrics need to be conducted. Corresponding mechanical models also need to be established and validated to obtain simulation parameters for the bending deformation of the fabric. Furthermore, the constitutive models used for simulating the textile reinforcements forming process should incorporate the relevant theory to express the bending deformation.
- Preforming of braided fabrics can be considered using other punch shapes (e.g., square and triangle) for preforming tests. Simultaneously, numerical simulations can be employed to study the effect of various parameters on the preforming shape of the fabric. This optimization of the forming process can enhance the quality of preforming and subsequently expand the range of applications for braided fabrics.
- The coupling characteristics of the various deformation modes affect the shape and quality of fabric preforms and also need to be investigated at a deeper level. For example, the effects of coupled tension-shear and shear-bending on the forming quality of braided fabrics. Conducting experiments involving different coupled deformation modes and establishing corresponding mechanical models to provide the basis for simulation analysis.

Reference

[1] Corman G, Upadhya R, Sinha S, Sweeney S, Wang S, Biller S, et al. General Electric Company: Selected Applications of Ceramics and Composite Materials. vol. 224. 2016. https://doi.org/10.1007/978-3-319-23419-9.

[2] Chen H, Li S, Wang J, Ding A. A focused review on the thermo-stamping process and simulation progresses of continuous fibre reinforced thermoplastic composites. Compos Part B Eng 2021;224:109196. https://doi.org/10.1016/j.compositesb.2021.109196.

[3] Saboktakin A. International Journal of Aviation , Aeronautics , and Aerospace 3D TEXTILE PREFORMS AND COMPOSITES FOR AIRCRAFT STRCUTURES : A REVIEW 2019;6.

[4] Byun, J. The analytical characterization of 2-D braided textile composites. Compos Sci Technol 2000;60:705–16.

[5] Saleh MN, Yudhanto A, Potluri P, Lubineau G, Soutis C. Characterising the loading direction sensitivity of 3D woven composites: Effect of z-binder architecture. Compos Part A Appl Sci Manuf 2016;90:577–88. https://doi.org/10.1016/j.compositesa.2016.08.028.

[6] Ngo T. Composite and Nanocomposite Materials - From Knowledge to Industrial Applications. Compos Nanocomposite Mater - From Knowl to Ind Appl 2020. https://doi.org/10.5772/intechopen.80186.

[7] Zhao Z, Li B, Ma P. Advances in mechanical properties of flexible textile composites. Compos Struct 2023;303:116350. https://doi.org/10.1016/j.compstruct.2022.116350.

[8] Poe CC, Dexter HB, Raju IS. Review of the NASA Textile Composites Research. 1997.

[9] Boris D, Xavier L, Damien S. The tensile behaviour of biaxial and triaxial braided fabrics. J Ind Text 2018;47:2184–204. https://doi.org/10.1177/1528083716654469.

[10] Sathishkumar TP, Satheeshkumar S, Naveen J. Glass fiber-reinforced polymer composites - A review. J Reinf Plast Compos 2014;33:1258–75. https://doi.org/10.1177/0731684414530790.

[11] Joshi S V., Drzal LT, Mohanty AK, Arora S. Are natural fiber composites environmentally superior to glass fiber reinforced composites? Compos Part A Appl Sci Manuf 2004;35:371–6. https://doi.org/10.1016/j.compositesa.2003.09.016.

[12] Totry E, Molina-Aldareguía JM, González C, LLorca J. Effect of fiber, matrix and interface properties on the in-plane shear deformation of carbon-fiber reinforced composites. Compos Sci Technol 2010;70:970–80. https://doi.org/10.1016/j.compscitech.2010.02.014.

[13] Cheng Z, Zhang L, Jiang C, Dai Y, Meng C, Luo L, et al. Aramid fiber with excellent interfacial properties suitable for resin composite in a wide polarity

range. Chem Eng J 2018;347:483–92. https://doi.org/10.1016/j.cej.2018.04.149.
[14] Kyosev Y, Gleßner P. Extended horn gears in 3D maypole braiding. J Text Fibrous Mater 2018;1:251522111878674. https://doi.org/10.1177/2515221118786741.
[15] Mouritz AP, Bannister MK, Falzon PJ, Leong KH. Review of applications for advanced three-dimensional fibre textile composites. Compos Part A Appl Sci Manuf 1999;30:1445–61. https://doi.org/10.1016/S1359-835X(99)00034-2.
[16] Potluri P, Rawal A, Rivaldi M, Porat I. Geometrical modelling and control of a triaxial braiding machine for producing 3D preforms. Compos Part A Appl Sci Manuf 2003;34:481–92. https://doi.org/10.1016/S1359-835X(03)00061-7.
[17] Fujita A, Maekawa Z, Hamada H, Yokoyama A. Mechanical Behavior and Fracture Mechanism in Flat Braided Composites. Part 1: Braided Flat Bar. J Reinf Plast Compos 1992;11:600–17. https://doi.org/10.1177/073168449201100602.
[18] Fujita A, Maekawa Z, Hamamda H, Yokoyama A. Mechanical Behavior and Fracture Mechanism in Flat Braided Composites. Part 2: Braided Flat Bar with a Circular Hole. J Reinf Plast Compos 1992;11:618–32. https://doi.org/10.1177/073168449201100603.
[19] Fujita A, Hamada H, Maekawa Z, Ohno E, Yokoyama A. Mechanical Behavior and Fracture Mechanism in Flat Braided Composites. Part 3: Mechanically Fastened Joint in Flat Braided Bar. J Reinf Plast Compos 1994;13:740–55. https://doi.org/10.1177/073168449401300805.
[20] Birkefeld K, Röder M, Von Reden T, Bulat M, Drechsler K. Characterization of biaxial and triaxial braids: Fiber architecture and mechanical properties. Appl Compos Mater 2012;19:259–73. https://doi.org/10.1007/s10443-011-9190-2.
[21] Kyosev Y. Geometrical modeling and computational mechanics tools for braided structures. Elsevier Ltd; 2016. https://doi.org/10.1016/b978-0-08-100407-4.00021-1.
[22] Gessler A. Braided reinforcements for composites. Compos Reinf Optim Perform 2011:116–56. https://doi.org/10.1533/9780857093714.2.116.
[23] Xiao S, Wang P, Soulat D, Legrand X. Structure and mechanics of braided fabrics. 2nd ed. Elsevier Ltd.; 2019. https://doi.org/10.1016/B978-0-08-102619-9.00007-9.
[24] Cichosz JA. Composites Experimental Characterization and Numerical Modeling of the Mechanical Response for Biaxial Braided Composites 2016.
[25] Chai BX, Eisenbart B, Nikzad M, Fox B, Blythe A, Blanchard P, et al. Simulation-based optimisation for injection configuration design of liquid composite moulding processes: A review. Compos Part A Appl Sci Manuf 2021;149:106540. https://doi.org/10.1016/j.compositesa.2021.106540.

[26] Zade A, Kuppusamy RRP. A review on numerical optimization in liquid composite moulding processes. Mater Today Proc 2019;19:329–32. https://doi.org/10.1016/j.matpr.2019.07.605.
[27] Trofimov A, Ravey C, Droz N, Therriault D, Lévesque M. A review on the Representative Volume Element-based multi-scale simulation of 3D woven high performance thermoset composites manufactured using resin transfer molding process. Compos Part A Appl Sci Manuf 2023;169:107499. https://doi.org/10.1016/j.compositesa.2023.107499.
[28] Wang P, Legrand X, Boisse P, Hamila N, Soulat D. Experimental and numerical analyses of manufacturing process of a composite square box part: Comparison between textile reinforcement forming and surface 3D weaving. Compos Part B Eng 2015;78:26–34. https://doi.org/10.1016/J.COMPOSITESB.2015.03.072.
[29] Limaye M, Pradeep SA, Kothari A, Savla S, Agha A, Pilla S, et al. Thermoforming process effects on structural performance of carbon fiber reinforced thermoplastic composite parts through a manufacturing to response pathway. Compos Part B Eng 2022;235:109728. https://doi.org/10.1016/j.compositesb.2022.109728.
[30] Guzman-Maldonado E, Hamila N, Naouar N, Moulin G, Boisse P. Simulation of thermoplastic prepreg thermoforming based on a visco-hyperelastic model and a thermal homogenization. Mater Des 2016;93:431–42. https://doi.org/10.1016/j.matdes.2015.12.166.
[31] Zhang W, Ren H, Liang B, Zeng D, Su X, Dahl J, et al. A non-orthogonal material model of woven composites in the preforming process. CIRP Ann - Manuf Technol 2017;66:257–60. https://doi.org/10.1016/j.cirp.2017.04.112.
[32] Wei K, Liang D, Mei M, Yang X, Chen L. A viscoelastic model of compression and relaxation behaviors in preforming process for carbon fiber fabrics with binder. Compos Part B Eng 2019;158:1–9. https://doi.org/10.1016/j.compositesb.2018.09.038.
[33] Li XK, Bai SL. Sheet forming of the multi-layered biaxial weft knitted fabric reinforcement. Part I: On hemispherical surfaces. Compos Part A Appl Sci Manuf 2009;40:766–77. https://doi.org/10.1016/j.compositesa.2009.03.007.
[34] Jauffrès D, Sherwood JA, Morris CD, Chen J. Discrete mesoscopic modeling for the simulation of woven-fabric reinforcement forming. Int J Mater Form 2010;3:1205–16. https://doi.org/10.1007/s12289-009-0646-y.
[35] Peng X, Ding F. Validation of a non-orthogonal constitutive model for woven composite fabrics via hemispherical stamping simulation. Compos Part A Appl Sci Manuf 2011;42:400–7. https://doi.org/10.1016/j.compositesa.2010.12.014.
[36] Chen S, McGregor OPL, Harper LT, Endruweit A, Warrior NA. Defect formation during preforming of a bi-axial non-crimp fabric with a pillar stitch pattern. Compos Part A Appl Sci Manuf 2016;91:156–67. https://doi.org/10.1016/j.compositesa.2016.09.016.

[37] Peng X, Rehman ZU. Textile composite double dome stamping simulation using a non-orthogonal constitutive model. Compos Sci Technol 2011;71:1075–81. https://doi.org/10.1016/j.compscitech.2011.03.010.
[38] Peng X, Guo Z, Du T, Yu WR. A simple anisotropic hyperelastic constitutive model for textile fabrics with application to forming simulation. Compos Part B Eng 2013;52:275–81. https://doi.org/10.1016/j.compositesb.2013.04.014.
[39] Harrison P, Gomes R, Curado-Correia N. Press forming a 0/90 cross-ply advanced thermoplastic composite using the double-dome benchmark geometry. Compos Part A Appl Sci Manuf 2013;54:56–69. https://doi.org/10.1016/j.compositesa.2013.06.014.
[40] Khan MA, Mabrouki T, Vidal-Sallé E, Boisse P. Numerical and experimental analyses of woven composite reinforcement forming using a hypoelastic behaviour. Application to the double dome benchmark. J Mater Process Technol 2010;210:378–88. https://doi.org/10.1016/J.JMATPROTEC.2009.09.027.
[41] Huang J, Boisse P, Hamila N, Gnaba I, Soulat D, Wang P. Experimental and numerical analysis of textile composite draping on a square box. Influence of the weave pattern. Compos Struct 2021;267:113844. https://doi.org/10.1016/j.compstruct.2021.113844.
[42] Iwata A, Inoue T, Naouar N, Boisse P, Lomov S V. Coupled meso-macro simulation of woven fabric local deformation during draping. Compos Part A Appl Sci Manuf 2019;118:267–80. https://doi.org/10.1016/j.compositesa.2019.01.004.
[43] Boisse P, Hamila N, Vidal-Sallé E, Dumont F. Simulation of wrinkling during textile composite reinforcement forming. Influence of tensile, in-plane shear and bending stiffnesses. Compos Sci Technol 2011;71:683–92. https://doi.org/10.1016/j.compscitech.2011.01.011.
[44] Allaoui S, Boisse P, Chatel S, Hamila N, Hivet G, Soulat D, et al. Experimental and numerical analyses of textile reinforcement forming of a tetrahedral shape. Compos Part A Appl Sci Manuf 2011;42:612–22. https://doi.org/10.1016/j.compositesa.2011.02.001.
[45] Allaoui S, Hivet G, Soulat D, Wendling A, Ouagne P, Chatel S. Experimental preforming of highly double curved shapes with a case corner using an interlock reinforcement. Int J Mater Form 2014;7:155–65. https://doi.org/10.1007/s12289-012-1116-5.
[46] Nosrat Nezami F, Gereke T, Cherif C. Active forming manipulation of composite reinforcements for the suppression of forming defects. Compos Part A Appl Sci Manuf 2017;99:94–101. https://doi.org/10.1016/j.compositesa.2017.04.011.
[47] Guzman-Maldonado E, Hamila N, Naouar N, Moulin G, Boisse P. Simulation of thermoplastic prepreg thermoforming based on a visco-hyperelastic model

and a thermal homogenization. Mater Des 2016;93:431–42. https://doi.org/10.1016/j.matdes.2015.12.166.
[48] Labanieh AR, Garnier C, Ouagne P, Dalverny O, Soulat D. Intra-ply yarn sliding defect in hemisphere preforming of a woven preform. Compos Part A Appl Sci Manuf 2018;107:432–46. https://doi.org/10.1016/j.compositesa.2018.01.018.
[49] Boisse P, Hamila N, Madeo A, Lyon U De. Modelling the development of defects during composite reinforcements and prepreg forming Subject Areas : 2016.
[50] Shen H, Yao L, Legrand X, Wang P. Characterization of wrinkle morphologies by surface waviness evaluation method during deep forming of multilayer composite preforms. Compos Struct 2023;306:116586. https://doi.org/10.1016/j.compstruct.2022.116586.
[51] Allaoui S, Cellard C, Hivet G. Effect of inter-ply sliding on the quality of multilayer interlock dry fabric preforms. Compos Part A Appl Sci Manuf 2015;68:336–45. https://doi.org/10.1016/j.compositesa.2014.10.017.
[52] Bloom LD, Wang J, Potter KD. Damage progression and defect sensitivity: An experimental study of representative wrinkles in tension. Compos Part B Eng 2013;45:449–58. https://doi.org/10.1016/j.compositesb.2012.05.021.
[53] Jacquot PB, Wang P, Soulat D, Legrand X. Analysis of the preforming behaviour of the braided and woven flax/polyamide fabrics. J Ind Text 2016;46:698–718. https://doi.org/10.1177/1528083715591592.
[54] Sharma SB, Sutcliffe MPF, Chang SH. Characterisation of material properties for draping of dry woven composite material. Compos Part A Appl Sci Manuf 2003;34:1167–75. https://doi.org/10.1016/j.compositesa.2003.09.001.
[55] Gatouillat S, Bareggi A, Vidal-Sallé E, Boisse P. Meso modelling for composite preform shaping - Simulation of the loss of cohesion of the woven fibre network. Compos Part A Appl Sci Manuf 2013;54:135–44. https://doi.org/10.1016/j.compositesa.2013.07.010.
[56] Xiao S, Wang P, Soulat D, Legrand X, Gao H. Towards the deformability of triaxial braided composite reinforcement during manufacturing. Compos Part B Eng 2019;169:209–20. https://doi.org/10.1016/j.compositesb.2019.04.017.
[57] Gereke T, Döbrich O, Hübner M, Cherif C. Experimental and computational composite textile reinforcement forming: A review. Compos Part A Appl Sci Manuf 2013;46:1–10. https://doi.org/10.1016/j.compositesa.2012.10.004.
[58] Bussetta P, Correia N. Numerical forming of continuous fibre reinforced composite material: A review. Compos Part A Appl Sci Manuf 2018;113:12–31. https://doi.org/10.1016/j.compositesa.2018.07.010.
[59] Boisse P, Gasser A, Hivet G. Analysis of the mechanical behaviour : determination of the biaxial tensio-strain surfaces and their use in forming simulations. Exp Mech 2001;32:260–9.

[60] Hivet G, Boisse P. Consistent mesoscopic mechanical behaviour model for woven composite reinforcements in biaxial tension. Compos Part B Eng 2008;39:345–61. https://doi.org/10.1016/j.compositesb.2007.01.011.
[61] Sagar T V., Potluri P, Hearle JWS. Mesoscale modelling of interlaced fibre assemblies using energy method. Comput Mater Sci 2003;28:49–62. https://doi.org/10.1016/S0927-0256(03)00056-9.
[62] Boisse P, Borr M, Buet K, Cherouat A. Finite element simulations of textile composite forming including the biaxial fabric behaviour. Compos Part B Eng 1997;28:453–64. https://doi.org/10.1016/S1359-8368(96)00067-4.
[63] Gong Y, Song Z, Ning H, Hu N, Peng X, Wu X, et al. A comprehensive review of characterization and simulation methods for thermo-stamping of 2D woven fabric reinforced thermoplastics. Compos Part B Eng 2020;203:108462. https://doi.org/10.1016/j.compositesb.2020.108462.
[64] LIANG B, BOISSE P. A review of numerical analyses and experimental characterization methods for forming of textile reinforcements. Chinese J Aeronaut 2021;34:143–63. https://doi.org/10.1016/J.CJA.2020.09.027.
[65] Boisse P, Hamila N, Guzman-Maldonado E, Madeo A, Hivet G, dell'Isola F. The bias-extension test for the analysis of in-plane shear properties of textile composite reinforcements and prepregs: a review. Int J Mater Form 2017;10:473–92. https://doi.org/10.1007/s12289-016-1294-7.
[66] Cao J, Akkerman R, Boisse P, Chen J, Cheng HS, Graaf E, et al. Characterization of mechanical behavior of woven fabrics: Experimental methods and benchmark results. Compos Part A Appl Sci & Manuf 2008;39:1037–53.
[67] Colman AG, Bridgens BN, Gosling PD, Jou GT, Hsu XY. Shear behaviour of architectural fabrics subjected to biaxial tensile loads. Compos Part A Appl Sci Manuf 2014;66:163–74. https://doi.org/10.1016/j.compositesa.2014.07.015.
[68] Shi T, Chen W, Gao C, Hu J, Zhao B, Zhang D, et al. Shear behavior of architectural coated fabrics under biaxial bias-extension. Constr Build Mater 2018;187:964–73. https://doi.org/10.1016/j.conbuildmat.2018.08.030.
[69] Spivak SM, Treloar LRG. The Behavior of Fabrics in Shear: Part III: The Relation Between Bias Extension and Simple Shear. Text Res J 1968;38:963–71. https://doi.org/10.1177/004051756803800911.
[70] Kawabata S, Niwa M, Kawai H. 3-THE FINITE-DEFORMATION THEORY OF PLAIN-WEAVE FABRICS PART I: THE BIAXIAL-DEFORMATION THEORY. J Text Inst 1973;64:47–61. https://doi.org/10.1080/00405007308630417.
[71] Grosberg P, Park BJ. The Mechanical Properties of Woven Fabrics: Part V: The Initial Modulus and the Frictional Restraint in shearing of Plain Weave Fabrics. Text Res J 1966;36:420–31. https://doi.org/10.1177/004051756603600505.

[72] Nosrat-Nezami F, Gereke T, Eberdt C, Cherif C. Characterisation of the shear-tension coupling of carbon-fibre fabric under controlled membrane tensions for precise simulative predictions of industrial preforming processes. Compos Part A Appl Sci Manuf 2014;67:131–9. https://doi.org/10.1016/j.compositesa.2014.08.030.
[73] Lomov S V., Boisse P, Deluycker E, Morestin F, Vanclooster K, Vandepitte D, et al. Full-field strain measurements in textile deformability studies. Compos Part A Appl Sci Manuf 2008;39:1232–44. https://doi.org/10.1016/j.compositesa.2007.09.014.
[74] Mohammed U, Lekakou C, Dong L, Bader MG. Shear deformation and micromechanics of woven fabrics. Compos Part A Appl Sci Manuf 2000;31:299–308. https://doi.org/10.1016/S1359-835X(99)00081-0.
[75] Nguyen M, Herszberg I, Paton R. The shear properties of woven carbon fabric. Compos Struct 1999;47:767–79. https://doi.org/10.1016/S0263-8223(00)00051-9.
[76] Launay J, Hivet G, Duong A V, Boisse P. Experimental analysis of the influence of tensions on in plane shear behaviour of woven composite reinforcements. Compos Sci & Technol 2008;68:506–15.
[77] Harrison P, Abdiwi F, Guo Z, Potluri P, Yu WR. Characterising the shear-tension coupling and wrinkling behaviour of woven engineering fabrics. Compos Part A Appl Sci Manuf 2012;43:903–14. https://doi.org/10.1016/j.compositesa.2012.01.024.
[78] Endruweit A, Long AC. A model for the in-plane permeability of triaxially braided reinforcements. Compos Part A Appl Sci Manuf 2011;42:165–72. https://doi.org/10.1016/j.compositesa.2010.11.003.
[79] Lindberg J, Behre B, Dahlberg B. Part III: Shearing and buckling of various commercial fabrics. Text Res J 1961;31:99–122.
[80] Skordos AA, Monroy Aceves C, Sutcliffe MPF. A simplified rate dependent model of forming and wrinkling of pre-impregnated woven composites. Compos Part A Appl Sci Manuf 2007;38:1318–30. https://doi.org/10.1016/j.compositesa.2006.11.005.
[81] Potluri P, Manan A. Mechanics of non-orthogonally interlaced textile composites. Compos Part A Appl Sci Manuf 2007;38:1216–26. https://doi.org/10.1016/j.compositesa.2006.04.008.
[82] Potluri P, Ciurezu DAP, Ramgulam RB. Measurement of meso-scale shear deformations for modelling textile composites. Compos Part A Appl Sci Manuf 2006;37:303–14. https://doi.org/10.1016/j.compositesa.2005.03.032.
[83] Hivet G, Duong A V. A contribution to the analysis of the intrinsic shear behavior of fabrics. J Compos Mater 2011;45:695–716. https://doi.org/10.1177/0021998310382315.

[84] Zhu B, Yu TX, Tao XM. Large deformation and slippage mechanism of plain woven composite in bias extension. Compos Part A Appl Sci Manuf 2007;38:1821–8. https://doi.org/10.1016/j.compositesa.2007.04.009.
[85] Härtel F, Harrison P. Evaluation of normalisation methods for uniaxial bias extension tests on engineering fabrics. Compos Part A Appl Sci Manuf 2014;67:61–9. https://doi.org/10.1016/j.compositesa.2014.08.011.
[86] Harrison P, Alvarez MF, Anderson D. Towards comprehensive characterisation and modelling of the forming and wrinkling mechanics of engineering fabrics. Int J Solids Struct 2018;154:2–18. https://doi.org/10.1016/j.ijsolstr.2016.11.008.
[87] Potluri P, Manan A, Francke M, Day RJ. Flexural and torsional behaviour of biaxial and triaxial braided composite structures. Compos Struct 2006;75:377–86. https://doi.org/10.1016/j.compstruct.2006.04.046.
[88] Del Rosso S, Iannucci L, Curtis PT. Experimental investigation of the mechanical properties of dry microbraids and microbraid reinforced polymer composites. Compos Struct 2015;125:509–19. https://doi.org/10.1016/j.compstruct.2015.02.036.
[89] Harte AM, Fleck NA. On the mechanics of braided composites in tension. Eur J Mech A/Solids 2000;19:259–75. https://doi.org/10.1016/S0997-7538(99)00164-3.
[90] Guzman-Maldonado E, Bel S, Bloom D, Fideu P, Boisse P. Experimental and numerical analyses of the mechanical behavior during draping of non-orthogonal bi-axial non-crimp fabric composite reinforcements. Mater Des 2022;218. https://doi.org/10.1016/j.matdes.2022.110682.
[91] Xiao S, Gao H, Soulat D, Wang P. A revised model of kinematic analysis on in-plane shearing behaviour of biaxial fabrics in bias extension test. Compos Part A Appl Sci Manuf 2022;163. https://doi.org/10.1016/j.compositesa.2022.107251.
[92] Boisse P, Colmars J, Hamila N, Naouar N, Steer Q. Bending and wrinkling of composite fiber preforms and prepregs. A review and new developments in the draping simulations. Compos Part B Eng 2018;141:234–49. https://doi.org/10.1016/j.compositesb.2017.12.061.
[93] Liang B, Hamila N, Peillon M, Boisse P. Analysis of thermoplastic prepreg bending stiffness during manufacturing and of its influence on wrinkling simulations. Compos Part A Appl Sci Manuf 2014;67:111–22. https://doi.org/10.1016/j.compositesa.2014.08.020.
[94] Boisse P, Colmars J, Hamila N, Naouar N, Steer Q. Bending and wrinkling of composite fiber preforms and prepregs. A review and new developments in the draping simulations. Compos Part B Eng 2018;141:234–49. https://doi.org/10.1016/j.compositesb.2017.12.061.
[95] Boisse P, Colmars J, Hamila N, Naouar N, Steer Q. Bending and wrinkling of composite fiber preforms and prepregs. A review and new developments in the

draping simulations. Compos Part B Eng 2018;141:234–49. https://doi.org/10.1016/j.compositesb.2017.12.061.
[96] Boisse P, Huang J, Guzman-Maldonado E. Analysis and modeling of wrinkling in composite forming. J Compos Sci 2021;5:1–16. https://doi.org/10.3390/jcs5030081.
[97] F. T. Peirce B.Sc., F.Inst.P. FTI. The “Handle” of Cloth As a Measurable Quantity. J Text Inst Trans 1930;21:1930.
[98] Peirce FT. 5—The geometry of cloth structure. vol. 28. 1937. https://doi.org/10.1080/19447023708658809.
[99] Bilisik K. Bending behavior of multilayered and multidirectional stitched aramid woven fabric structures. Text Res J 2011;81:1748–61. https://doi.org/10.1177/0040517511411974.
[100] Yu F, Chen S, Viisainen J V., Sutcliffe MPF, Harper LT, Warrior NA. A macroscale finite element approach for simulating the bending behaviour of biaxial fabrics. Compos Sci Technol 2020;191. https://doi.org/10.1016/j.compscitech.2020.108078.
[101] Lammens N, Kersemans M, Luyckx G, Van Paepegem W, Degrieck J. Improved accuracy in the determination of flexural rigidity of textile fabrics by the Peirce cantilever test (ASTM D1388). Text Res J 2014;84:1307–14. https://doi.org/10.1177/0040517514523182.
[102] de Bilbao E, Soulat D, Hivet G, Gasser A. Experimental Study of Bending Behaviour of Reinforcements. Exp Mech 2010;50:333–51. https://doi.org/10.1007/s11340-009-9234-9.
[103] Liang B, Chaudet P, Boisse P. Curvature determination in the bending test of continuous fibre reinforcements. Strain 2017;53:1–12. https://doi.org/10.1111/str.12213.
[104] Sherwood JA, Fetfatsidis KA, Gorczyca JL, Berger L. Fabric thermostamping in polymer matrix composites. vol. m. Woodhead Publishing Limited; 2012. https://doi.org/10.1533/9780857096258.2.139.
[105] Alshahrani H, Hojjati M. A new test method for the characterization of the bending behavior of textile prepregs. Compos Part A Appl Sci Manuf 2017;97:128–40. https://doi.org/10.1016/j.compositesa.2017.02.027.
[106] Lomov S V., Verpoest I, Barburski M, Laperre J. Carbon composites based on multiaxial multiply stitched preforms. Part 2. KES-F characterisation of the deformability of the preforms at low loads. Compos Part A Appl Sci Manuf 2003;34:359–70. https://doi.org/10.1016/S1359-835X(03)00025-3.
[107] Sachs U, Akkerman R. Viscoelastic bending model for continuous fiber-reinforced thermoplastic composites in melt. Compos Part A Appl Sci Manuf 2017;100:333–41. https://doi.org/10.1016/j.compositesa.2017.05.032.
[108] Hamila N, Boisse P. Tension locking in finite-element analyses of textile composite reinforcement deformation textiles de composites. Comptes Rendus - Mec 2013;341:508–19. https://doi.org/10.1016/j.crme.2013.03.001.

[109] Guan W, Dai Y, Li W, Qu Y, He P. An improved semi-discrete approach for simulation of 2 . 5D woven fabric preforming. Compos Struct 2022;282:115093. https://doi.org/10.1016/j.compstruct.2021.115093.
[110] Hearle JWS. Mechanical properties of textile reinforcements for composites. Elsevier Ltd.; 2015. https://doi.org/10.1016/B978-1-78242-307-2.00011-7.
[111] Xie J, Guo Z, Shao M, Zhu W, Jiao W, Yang Z, et al. Mechanics of textiles used as composite preforms: A review. Compos Struct 2023;304:116401. https://doi.org/10.1016/j.compstruct.2022.116401.
[112] Nguyen QT, Vidal-sallé E, Boisse P, Park CH, Saouab A, Bréard J, et al. Composites : Part B Mesoscopic scale analyses of textile composite reinforcement compaction. Compos Part B 2013;44:231–41. https://doi.org/10.1016/j.compositesb.2012.05.028.
[113] Tabatabaei SA, Lomov S V, Verpoest I. Assessment of embedded element technique in meso-FE modelling of fibre reinforced composites. Compos Struct 2014;107:436–46. https://doi.org/10.1016/j.compstruct.2013.08.020.
[114] Syerko E, Schmidt T, May D, Binetruy C, Advani SG, Lomov S, et al. Benchmark exercise on image-based permeability determination of engineering textiles : Microscale predictions 2023;167. https://doi.org/10.1016/j.compositesa.2022.107397.
[115] Wang Y, Sun X. Digital-element simulation of textile processes 2001;61:311–9.
[116] Zhou G, Sun X, Wang Y. Multi-chain digital element analysis in textile mechanics 2004;64:239–44. https://doi.org/10.1016/S0266-3538(03)00258-6.
[117] Said B El, Green S, Hallett SR. Composites : Part A Kinematic modelling of 3D woven fabric deformation for structural scale features. Compos Part A 2014;57:95–107. https://doi.org/10.1016/j.compositesa.2013.11.006.
[118] Wang Y, Miao Y, Swenson D, Cheeseman BA, Yen CF, LaMattina B. Digital element approach for simulating impact and penetration of textiles. Int J Impact Eng 2010;37:552–60. https://doi.org/10.1016/j.ijimpeng.2009.10.009.
[119] Liu KYSÆXH. A new skeletal model for fabric drapes 2006:225–43. https://doi.org/10.1007/s10999-006-9004-0.
[120] Thompson AJ, El Said B, Belnoue JPH, Hallett SR. Modelling process induced deformations in 0/90 non-crimp fabrics at the meso-scale. Compos Sci Technol 2018;168:104–10. https://doi.org/10.1016/j.compscitech.2018.08.029.
[121] Durville D. Simulation of the mechanical behaviour of woven fabrics at the scale of fibers. Int J Mater Form 2010;3:1241–51. https://doi.org/10.1007/s12289-009-0674-7.
[122] Liu C, Xie J, Sun Y, Chen L. Micro-scale modeling of textile composites based on the virtual fiber embedded models. Compos Struct 2019;230:111552. https://doi.org/10.1016/j.compstruct.2019.111552.

[123] Wu L, Zhao F, Xie J, Wu X, Jiang Q, Lin JH. The deformation behaviors and mechanism of weft knitted fabric based on micro-scale virtual fiber model. Int J Mech Sci 2020;187:105929. https://doi.org/10.1016/j.ijmecsci.2020.105929.
[124] Daelemans L, Tomme B, Caglar B, Michaud V, Van Stappen J, Cnudde V, et al. Kinematic and mechanical response of dry woven fabrics in through-thickness compression: Virtual fiber modeling with mesh overlay technique and experimental validation. Compos Sci Technol 2021;207. https://doi.org/10.1016/j.compscitech.2021.108706.
[125] Daelemans L, Faes J, Allaoui S, Hivet G, Dierick M, Van Hoorebeke L, et al. Finite element simulation of the woven geometry and mechanical behaviour of a 3D woven dry fabric under tensile and shear loading using the digital element method. Compos Sci Technol 2016;137:177–87. https://doi.org/10.1016/j.compscitech.2016.11.003.
[126] Green SD, Long AC, El Said BSF, Hallett SR. Numerical modelling of 3D woven preform deformations. Compos Struct 2014;108:747–56. https://doi.org/10.1016/j.compstruct.2013.10.015.
[127] Hamila N, Boisse P. Simulations of textile composite reinforcement draping using a new semi-discrete three node finite element. Compos Part B Eng 2008;39:999–1010. https://doi.org/10.1016/J.COMPOSITESB.2007.11.008.
[128] Remacle J, Lambrechts J, Seny B. A semi-discrete shell finite element for textile composite reinforcement forming simulation. International 2012:1102–19. https://doi.org/10.1002/nme.
[129] Hamila N, Boisse P. Locking in simulation of composite reinforcement deformations. Analysis and treatment. Compos Part A Appl Sci Manuf 2013;53:109–17. https://doi.org/10.1016/j.compositesa.2013.06.001.
[130] De Luycker E, Morestin F, Boisse P, Marsal D. Simulation of 3D interlock composite preforming. Compos Struct 2009;88:615–23. https://doi.org/10.1016/j.compstruct.2008.06.005.
[131] Wang P, Hamila N, Boisse P. Thermoforming simulation of multilayer composites with continuous fibres and thermoplastic matrix. Compos Part B Eng 2013;52:127–36. https://doi.org/10.1016/J.COMPOSITESB.2013.03.045.
[132] Aimène Y, Vidal-Sallé E, Hagège B, Sidoroff F, Boisse P. A hyperelastic approach for composite reinforcement large deformation analysis. J Compos Mater 2010;44:5–26. https://doi.org/10.1177/0021998309345348.
[133] Charmetant A, Orliac JG, Vidal-Sallé E, Boisse P. Hyperelastic model for large deformation analyses of 3D interlock composite preforms. Compos Sci Technol 2012;72:1352–60. https://doi.org/10.1016/j.compscitech.2012.05.006.
[134] Peng XQ, Cao J. A continuum mechanics-based non-orthogonal constitutive model for woven composite fabrics. Compos Part A Appl Sci Manuf 2005;36:859–74. https://doi.org/10.1016/j.compositesa.2004.08.008.
[135] Yu WR, Pourboghrat F, Chung K, Zampaloni M, Kang TJ. Non-orthogonal constitutive equation for woven fabric reinforced thermoplastic composites.

Compos Part A Appl Sci Manuf 2002;33:1095–105. https://doi.org/10.1016/S1359-835X(02)00053-2.
[136] Badel P, Gauthier S, Vidal-Sallé E, Boisse P. Rate constitutive equations for computational analyses of textile composite reinforcement mechanical behaviour during forming. Compos Part A Appl Sci Manuf 2009;40:997–1007. https://doi.org/10.1016/j.compositesa.2008.04.015.
[137] Chen B, Colmars J, Naouar N, Boisse P. A hypoelastic stress resultant shell approach for simulations of textile composite reinforcement forming. Compos Part A Appl Sci Manuf 2021;149:106558. https://doi.org/10.1016/j.compositesa.2021.106558.
[138] Chen S, Endruweit A, Harper LT, Warrior NA. Inter-ply stitching optimisation of highly drapeable multi-ply preforms. Compos Part A Appl Sci Manuf 2015;71:144–56. https://doi.org/10.1016/j.compositesa.2015.01.016.
[139] Charmetant A, Vidal-Sallé E, Boisse P. Hyperelastic modelling for mesoscopic analyses of composite reinforcements. Compos Sci Technol 2011;71:1623–31. https://doi.org/10.1016/j.compscitech.2011.07.004.
[140] Schäfer F, Werner HO, Henning F, Kärger L. A hyperelastic material model considering biaxial coupling of tension–compression and shear for the forming simulation of woven fabrics. Compos Part A Appl Sci Manuf 2023;165:107323. https://doi.org/10.1016/j.compositesa.2022.107323.
[141] Pazmino J, Mathieu S, Carvelli V, Boisse P, Lomov S V. Numerical modelling of forming of a non-crimp 3D orthogonal weave E-glass composite reinforcement. Compos Part A Appl Sci Manuf 2015;72:207–18. https://doi.org/10.1016/j.compositesa.2015.02.013.
[142] Schäfer F, Werner HO, Henning F, Kärger L. A hyperelastic material model considering biaxial coupling of tension–compression and shear for the forming simulation of woven fabrics. Compos Part A Appl Sci Manuf 2023;165:107323. https://doi.org/10.1016/j.compositesa.2022.107323.
[143] Arnold SE, Sutcliffe MPF, Oram WLA. Experimental measurement of wrinkle formation during draping of non-crimp fabric. Compos Part A Appl Sci Manuf 2016;82:159–69. https://doi.org/10.1016/j.compositesa.2015.12.011.
[144] Domskiene J, Strazdiene E, Bekampiene P. Development and optimisation of image analysis technique for fabric buckling evaluation. Int J Cloth Sci Technol 2011;23:329–40. https://doi.org/10.1108/09556221111166266.
[145] Zhu B, Yu TX, Teng J, Tao XM. Theoretical modeling of large shear deformation and wrinkling of plain woven composite. J Compos Mater 2009;43:125–38. https://doi.org/10.1177/0021998308098237.
[146] Hao SA, Peng W, Xl A. In-plane shear characteristics during the forming of tufted carbon woven fabrics. Compos Part A Appl Sci Manuf 2020;141.
[147] Kyosev Y, Aurich M. Investigations about the braiding angle and the cover factor of the braided fabrics using Image Processing and Symbolic Math

Toolbox of Matlab. Elsevier Ltd; 2016. https://doi.org/10.1016/b978-0-08-100407-4.00023-5.
[148] Wang J, Wang P, Hamila N, Boisse P. Mesoscopic analyses of the draping of 3D woven composite reinforcements based on macroscopic simulations. Compos Struct 2020;250:112602. https://doi.org/10.1016/j.compstruct.2020.112602.
[149] Naouar N, Vidal-Salle E, Schneider J, Maire E, Boisse P. 3D composite reinforcement meso F.E. analyses based on X-ray computed tomography. Compos Struct 2015;132:1094–104. https://doi.org/10.1016/j.compstruct.2015.07.005.
[150] Naouar N, Vidal-Sallé E, Schneider J, Maire E, Boisse P. Meso-scale FE analyses of textile composite reinforcement deformation based on X-ray computed tomography. Compos Struct 2014;116:165–76. https://doi.org/10.1016/j.compstruct.2014.04.026.
[151] Suman R, Kumar L, Khan IH. Exploring the potential of 3D Scanning in Industry 4.0: An Overview. Int J Cogn Comput Eng 2022:0–22. https://doi.org/10.1016/j.ijcce.2022.08.003.
[152] Ouagne P, Soulat D, Moothoo J, Capelle E, Gueret S. Complex shape forming of a flax woven fabric; Analysis of the tow buckling and misalignment defect. Compos Part A Appl Sci Manuf 2013;51:1–10. https://doi.org/10.1016/j.compositesa.2013.03.017.
[153] Shen H, Wang P, Legrand X, Liu L. Characterisation and optimisation of wrinkling during the forming of tufted three-dimensional composite preforms. Compos Part A Appl Sci Manuf 2019;127:105651. https://doi.org/10.1016/j.compositesa.2019.105651.
[154] Wu C. SiftGPU: A GPU Implementation of Scale Invariant Feature Transform SIFT 2013.
[155] Bianco S, Ciocca G, Marelli D. Evaluating the performance of structure from motion pipelines. J Imaging 2018;4:1–18. https://doi.org/10.3390/jimaging4080098.
[156] CloudCompare v2.6.1-User manual.pdfng.pdf. n.d. https://doi.org/https://www.danielgm.net/cc/doc/qCC/.
[157] Shenglei, Xiao, Peng, Wang, Damien, Soulat, et al. Analysis of the in-plane shear behaviour of non-orthogonally textile reinforcements: Application to braided fabrics. Compos Part B Eng 2018.
[158] Wakeman MD, Rudd CD, Cain TA, Brooks R, Long AC. Compression moulding of glass and polypropylene composites for optimised macro- and micro-mechanical properties. 4: Technology demonstrator - a door cassette structure. Compos Sci Technol 2000;60:1901–18. https://doi.org/10.1016/S0266-3538(00)00066-X.

[159] A TB, A BF, B JD, B PG. Experimental investigation of stamp forming of unconsolidated commingled E-glass/polypropylene fabrics. Compos Sci Technol 2006;66:555–70.
[160] Long AC. Composites Forming Technologies. Crc Press 2007.
[161] Wang Y, Chea MK, Belnoue JPH, Kratz J, Ivanov DS, Hallett SR. Experimental characterisation of the in-plane shear behaviour of UD thermoset prepregs under processing conditions. Compos Part A Appl Sci Manuf 2020;133. https://doi.org/10.1016/J.COMPOSITESA.2020.105865.
[162] Lebrun G, Bureau MN, Denault J. Evaluation of bias-extension and picture-frame test methods for the measurement of intraply shear properties of PP/glass commingled fabrics. Compos Struct 2003.
[163] Harrison P, Clifford MJ, Long AC. Shear characterisation of viscous woven textile composites: a comparison between picture frame and bias extension experiments. Compos Sci Technol 2004.
[164] Chellamani K, Sudharsan J, Sathish J. Medical textiles using Braiding Technology 2015.
[165] Rana S, Fangueiro R. Braided Structures and Composites: Production, Properties, Mechanics, and Technical Applications. Braided Structures and Composites: Production, Properties, Mechanics, and Technical Applications; 2015.
[166] Lee W, Padvoiskis J, Cao J, de Luycker E, Boisse P, Morestin F, et al. Bias-extension of woven composite fabrics. Int J Mater Form 2008;1:895–8. https://doi.org/10.1007/s12289-008-0240-8.
[167] Xiao S, Wang P, Soulat D, Gao H. Thermo-Mechanical Characterisations of Flax Fibre and Thermoplastic Resin Composites during Manufacturing. Polym 2018, Vol 10, Page 1139 2018;10:1139. https://doi.org/10.3390/POLYM10101139.
[168] Omrani F, Wang P, Soulat D, Ferreira M. Mechanical properties of flax-fibre-reinforced preforms and composites: Influence of the type of yarns on multi-scale characterisations. Compos Part A Appl Sci Manuf 2017;93:72–81. https://doi.org/10.1016/J.COMPOSITESA.2016.11.013.
[169] Du GW, Popper P. Analysis of a circular braiding process for complex shapes. J Text Inst 1994;85:316–37. https://doi.org/10.1080/00405009408631277.
[170] Rawal A, Kumar R, Saraswat H. Tensile mechanics of braided sutures. Text Res J 2012;82:1703–10. https://doi.org/10.1177/0040517512445340.
[171] Guzman-Maldonado E, Hamila N, Boisse P, Bikard J. Thermomechanical analysis, modelling and simulation of the forming of pre-impregnated thermoplastics composites. Compos Part A Appl Sci Manuf 2015;78:211–22. https://doi.org/10.1016/j.compositesa.2015.08.017.
[172] Buet-Gautier K, Boisse P. Experimental analysis and modeling of biaxial mechanical behavior of woven composite reinforcements. Exp Mech 2001;41:260–9. https://doi.org/10.1007/BF02323143.

[173] Lussier D, Chen J. Composite Materials of Woven Fabrics for. J Thermoplast Compos Mater 2002;15:497–509. https://doi.org/10.1106/089270502023205.
[174] Peng X, Cao J. A dual homogenization and finite element approach for material characterization of textile composites. Compos Part BEngineering 2002;33:45–56. https://doi.org/10.1016/S1359-8368(01)00052-X.
[175] Zhu B, Yu TX, Tao XM. An experimental study of in-plane large shear deformation of woven fabric composite. Compos Sci Technol 2007;67:252–61. https://doi.org/10.1016/j.compscitech.2006.08.011.
[176] Zhu B, Yu TX, Tao XM. Large shear deformation of E-glass/ polypropylene woven fabric composites at elevated temperatures. J Reinf Plast Compos 2009;28:2615–30. https://doi.org/10.1177/0731684408093095.
[177] Yin H, Peng X, Du T, Guo Z. Draping of plain woven carbon fabrics over a double-curvature mold. Compos Sci Technol 2014;92:64–9. https://doi.org/10.1016/j.compscitech.2013.12.013.
[178] Hosseini A, Kashani MH, Sassani F, Milani AS, Ko FK. Identifying the distinct shear wrinkling behavior of woven composite preforms under bias extension and picture frame tests. Compos Struct 2018;185:764–73. https://doi.org/10.1016/j.compstruct.2017.11.033.

Appendix A

Coefficients identified on the tensile behavior of the fabric

The tensile strain energy of fabric can be considered to be related to the elongation of the yarn, and the tensile coefficients describe the relationship between the tensile strain energy and the tensile invariants. The identification of these coefficients are mainly determined by the universal tensile test of a single yarn. Since yarns may be damaged during the braiding process, it is necessary to test yarns extracted from the fabric before braiding.

The tests used in this thesis was completed in the Gemtex laboratory, and the test setup are shown in Fig. A1 (a). A single Flax/PA12 yarn was selected to do the test at room temperature. The yarn was inserted and clamped by a top movable clamp, a load sensor on the top clamp measured the load in real time. The machine was set at 150 mm to ensure an accurate fixed length of the specimen. A preliminary test was conducted to verify that the slip of the test specimen was 0%. The load curve of the test is shown in Fig. A1 (b).

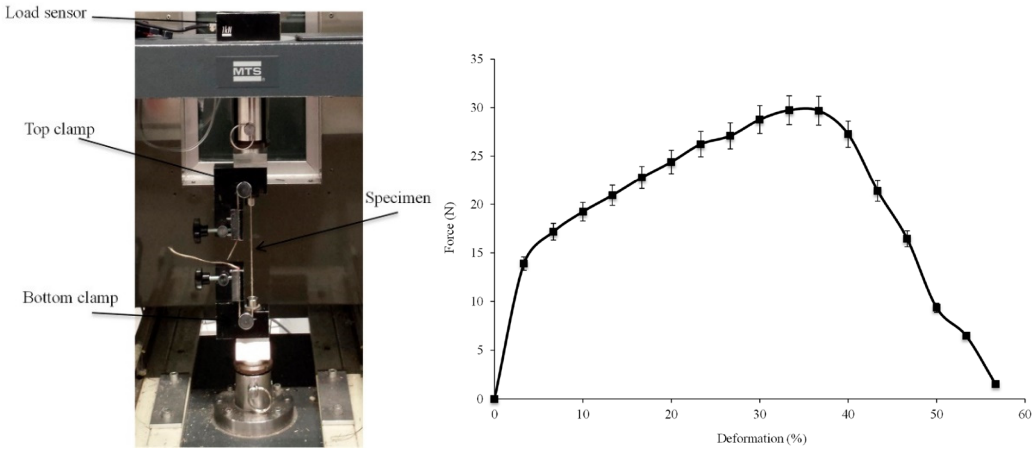

(a) (b)

Fig. A1 Tensile test of single yarn [167].

The tensile coefficient of the fabric describes the relationship between the tensile

invariants and the tensile strain energy. Using the load-deformation curve of yarn to obtain tensile coefficients requires establishing their relationship to tensile strain energy, which depends on the second Piola-Kirchhoff tensile stress tensor. The schematic diagram of a single yarn before and after deformation is shown in Fig. A2. Define $\lambda = \frac{L}{L_0}$.

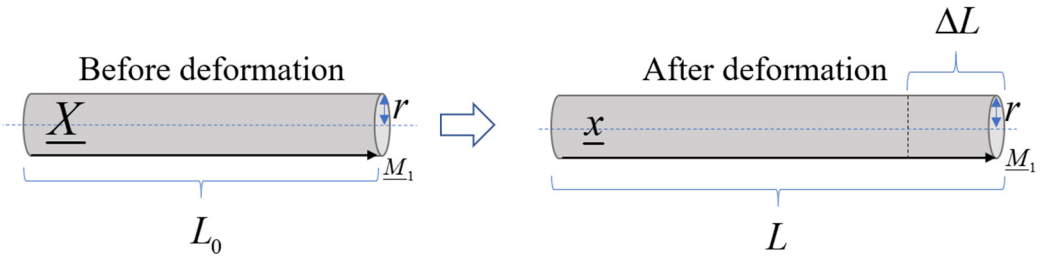

Fig. A2 Schematic diagram of a single yarn before and after deformation.

Using the elongation of the yarn, its deformation gradient is expressed as:

$$\underline{\underline{F}} = \begin{pmatrix} \frac{\partial x}{\partial X} & \frac{\partial x}{\partial Y} & \frac{\partial x}{\partial Z} \\ \frac{\partial y}{\partial X} & \frac{\partial y}{\partial Y} & \frac{\partial y}{\partial Z} \\ \frac{\partial z}{\partial X} & \frac{\partial z}{\partial Y} & \frac{\partial z}{\partial Z} \end{pmatrix} = \begin{pmatrix} \lambda & 0 & 0 \\ 0 & 1 & 0 \\ 0 & 0 & 1 \end{pmatrix} \tag{A1}$$

An expression for the right Cauchy Green strain tensor:

$$\underline{\underline{C}} = \underline{\underline{F}}^T \underline{\underline{F}} = \begin{pmatrix} \lambda^2 & 0 & 0 \\ 0 & 1 & 0 \\ 0 & 0 & 1 \end{pmatrix} \tag{A2}$$

According to Equation 3.24, the second Kirchhoff tensile stress tensor is expressed as:

$$\underline{\underline{S}}_{\text{elong1}} = 2\frac{\partial w_{\text{elong1}}}{\partial \underline{\underline{C}}} = 2\left(\frac{\partial w_{elong1}}{\partial I_{elong1}} \cdot \frac{\partial I_{elong1}}{\partial \underline{\underline{C}}}\right) = \frac{1}{\lambda^2} \cdot \sum_{i=1}^{n} 2i \cdot c_i \left(I_{elong1}\right)^{2i-1} \cdot \underline{\underline{M}}_{11} \tag{A3}$$

Considering that the only mode of deformation of the yarn is tension, the external power due to machine forces can be related to the internal power due to tensile forces of yarn:

$$P_{ext} = P_{int} \tag{A4}$$

$$F\dot{u}(t) = \frac{1}{2}\int_{\Omega_0} \underline{\underline{S}}_{elong1} : \dot{\underline{\underline{C}}}(t) dV_0 \tag{A5}$$

The relationship between tensile load, deformation and tensile coefficient is:

$$F = \frac{1}{\lambda} \cdot \pi \cdot r^2 \cdot \sum_{i=1}^{n} 2i \cdot c_i \left(I_{elong1} \right)^{2i-1} \tag{A6}$$

From Fig. A1 (b), it is found that the tensile of a single yarn is divided into three stages, corresponding to the breakage of flax and PA12. For the fitting, only the first linear portion of the yarn was selected. According to Eq. A6, using MATLAB to fit Fig. A1 (b), the tensile coefficient can be obtained, shown in Fig. A3.

$$n = 1; c_1 = 181$$

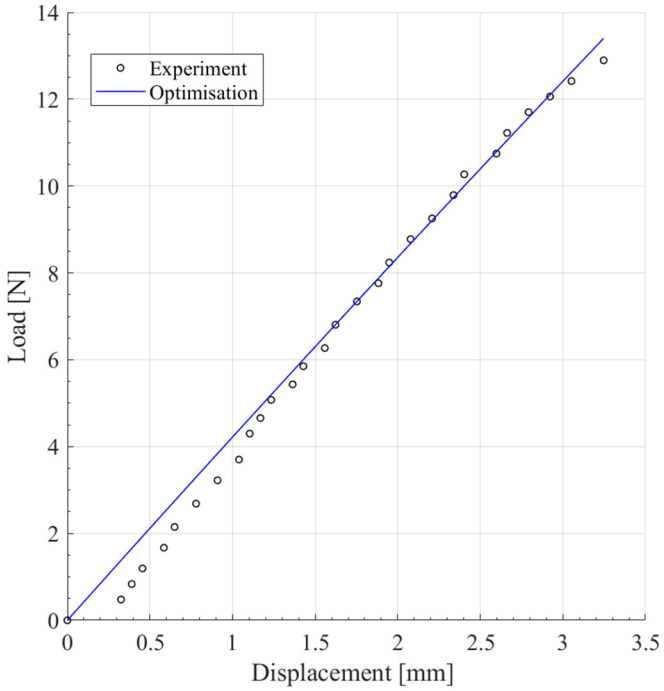

Fig. A3 Identification of tensile parameters for flax/PA12 single yarn.